
MECHANICAL PROPERTIES OF CELLS AND MATRIX
INVESTIGATED BY QUANTITATIVE ATOMIC FORCE
MICROSCOPY

Stefanie Kiderlen



München 2019

MECHANICAL PROPERTIES OF CELLS AND MATRIX
INVESTIGATED BY QUANTITATIVE ATOMIC FORCE
MICROSCOPY

Stefanie Kiderlen

Dissertation
an der Fakultät für Physik
der Ludwig-Maximilians-Universität
München

vorgelegt von
Stefanie Kiderlen
aus Konstanz

München, den 18.12.2019

Erstgutachter: Prof. Dr. Joachim O. Rädler

Zweitgutachter: Prof. Dr. Hauke Clausen-Schaumann

Tag der mündlichen Prüfung: 17.02.2020

ZUSAMMENFASSUNG

Zellen und deren umgebende extrazelluläre Matrix (ECM) sind einer Vielzahl unterschiedlicher mechanischer Belastungen im Körper ausgesetzt. Daher ist der strukturelle Aufbau eines jeden Gewebes an die entsprechenden Anforderungen angepasst. Dabei spielen sowohl intrazellulär als auch extrazellulär Netzwerke aus Strukturproteinen eine maßgebliche Rolle: Intrazellulär bestimmt u.a. die Architektur des Aktin-Zytoskeletts die mechanischen Eigenschaften von Zellen, extrazellulär ist die mechanische Stabilität der extrazellulären Basalmembran (BM) im Wesentlichen durch ein Netzwerk aus Laminin determiniert. In dieser Arbeit wurde mittels Rasterkraftmikroskopie untersucht, auf welche Weise die Struktur dieser Netzwerke den Elastizitätsmodul der ECM, einzelner lebender Zellen und zellbeladener 3D-Hydrogele beeinflusst. Das Rasterkraftmikroskop (AFM) ermöglicht dabei die Untersuchung von Mikroelastizitäten mit einer hohen räumlichen Auflösung unter nahezu physiologischen Bedingungen.

Im ersten Teil der Arbeit wurde gezeigt, dass die mechanischen Eigenschaften der BM durch das Protein Netrin-4 (Net-4) moduliert wird. Hierzu wurde Matrigel, ein Laminin-haltiges, ECM-basiertes Hydrogel, welches als artifizielle BM diente, mit zunehmenden Mengen des Proteins Net-4 versetzt. AFM-Indentationsmessungen zeigten eine quantitative Abnahme des Elastizitätsmoduls mit zunehmender Net-4 Konzentration. Dies bestätigt die postulierte Funktion von Net-4 als Regulator für die mechanischen Eigenschaften der BM und stützt die Hypothese, dass die Modulation der BM-Mechanik auf einer kompetitiven Bindung von Net-4 an die ternären Knotenpunkte beruht, an denen durch Verbindung von jeweils drei Laminin-Molekülen die Netzwerkbildung erfolgt.

Im zweiten Teil der Arbeit wurde der Zusammenhang zwischen der Struktur des Aktin-Zytoskeletts und der lokalen Elastizität in lebenden Zellen mittels räumlich hochauflösender, quantitativer Rasterkraftmikroskopie, welche das schnelle und simultane Messen der Zelltopographie und des Elastizitätsmoduls einzelner Zellen ermöglicht, untersucht. Insgesamt konnten dadurch Elastizitätsprofile einzelner Zellen erstellt werden, wodurch sich eindeutig unterschiedliche Elastizitätsmoduln den unterschiedlichen Vernetzungsformen des Aktin-Zytoskeletts zuordnen ließen: Aktin-Netzwerke aus stark verzweigten Aktinfasern zeigten einen höheren Elastizitätsmodul, als Bereiche mit linearen und parallelen Fasern. Bei einer parallelen Anordnung der Fasern sinkt außerdem der Elastizitätsmodul mit zunehmendem Abstand zwischen den Fasern.

Die Struktur des Aktin-Zytoskeletts wird dabei durch eine Vielzahl von Gerüstproteinen, wie z.B. α -Aktinin-1 (A1) und -4 (A4), bestimmt. Ein Knockout beider α -Aktinine resultierte in einem stark verzweigten basalen Aktin-Zytoskelett, welches sich kranzförmig um den Zellkern anordnete, sowie einem Verlust kernüberspannender dorsaler Aktinfasern, den sogenannten Aktinkappen. Bezogen auf die Topographie und den Elastizitätsmodul führte dies zu einer Art „Spiegelei“-Struktur: mittig waren diese Zellen hoch und weich, in der Peripherie jedoch flach und fest. Für A1 und A4 konnten außerdem unterschiedliche Funktionen in Bezug auf die Aktinarchitektur und damit die mechanischen Eigenschaften der Zellen identifiziert werden. A1 fördert das Ausbilden geradliniger basaler und dorsaler Aktinfasern. Durch das Vorhandensein von nur wenigen Aktinkappen ähneln die Zellen zwar dem Phänotyp von Wildtypzellen, insgesamt zeigen sie jedoch einen verringerten Elastizitätsmodul über den gesamten Bereich der Zelle. Im Gegensatz dazu fördert A4 die Quervernetzung der Aktinfasern. Dies resultierte ebenfalls peripher in einem netzartigen, flachen und festen sowie mittig in einem hohen und weichen Erscheinungsbild der Zellen.

Die Struktur des Aktin-Zytoskeletts ändert sich außerdem durch natürliche Prozesse, wie das Altern von Zellen. Durch den Vergleich des Elastizitätsprofils und des Aktin-Zytoskeletts primärer, humaner Sehnenvorläuferzellen (TSPC) von jungen und älteren Patienten (Y-TSPC und A-TSPC) konnte gezeigt werden, dass diese strukturellen Veränderungen den Elastizitätsmodul der Zelle modellieren, und der Elastizitätsmodul somit als Biomarker für Zellalterung dienen kann. Im Vergleich zu Y-TSPCs zeigten die A-TSPCs einen höheren Elastizitätsmodul und dichter gepackte parallele Aktinfasern. Die Inhibition von ROCK 1 und 2 in A-TSPCs, führte wieder zu einem lose gepackten Aktin-Zytoskelett und damit zu einer Annäherung an die Struktur von Y-TSPCs. Auch diese „strukturelle Verjüngung“ manifestierte sich in einem verringerten Elastizitätsmodul, ähnlich dem von Y-TSPC Zellen.

Schließlich wurde gezeigt, inwiefern Y- und A-TSPC Zellen die mechanischen Eigenschaften ihrer umgebenden Matrix beeinflussen können, indem diese in einem dreidimensionalen Polypeptid-basierten Hydrogel kultiviert und das Gel anschließend auf Veränderungen im Elastizitätsmodul hin untersucht wurde. Dabei konnte gezeigt werden, dass beide Zelltypen den Elastizitätsmodul der umgebenden Matrix deutlich erhöhen. Dieser Effekt war bei A-TSPCs deutlicher ausgeprägt als bei Y-TSPCs, was als weiteres Merkmal für Zellalterung gedeutet werden kann. Das Elastizitätsmodul könnte auch hier als Biomarker für Zellalterung dienen um zukünftig Gewebe mit jungen von Gewebe mit gealterten Zellen zu unterscheiden.

SUMMARY

Cells and their extracellular matrix (ECM) are exposed to a broad range of different mechanical loads in the body. For this reason, the structural composition of each tissue is adapted to its specific requirements. In this context, networks of structural proteins play a crucial role: for example, the architecture of the actin cytoskeleton determines the mechanical properties of cells and the mechanical stability of the extracellular basement membrane (BM) is determined mainly by a laminin network. In this thesis, atomic force microscopy (AFM), which allows the investigation of the microelasticity with a high spatial resolution under nearly physiological conditions, was used to investigate how the structure of these networks affects the Young's modulus of the ECM, of single living cells and cell-laden 3D hydrogels.

In the first part of this thesis, it was shown that the mechanical properties of the BM can be regulated by the protein Netrin-4 (Net-4). For this purpose, matrigel, a laminin-containing, ECM-based hydrogel, which served as an artificial BM, was supplemented with increasing amounts of the protein Net-4. AFM measurements revealed a quantitative decrease of the Young's modulus with increasing Net-4 concentrations. This confirms the postulated function of Net-4 as a regulator for the mechanical properties of the BM and supports the hypothesis that the modulation of the BM-mechanics is based on competitive binding of Net-4 to the ternary nodes usually connecting three laminin molecules for network formation.

In the second part of the thesis, the relationship between the structure of the actin cytoskeleton and the local elasticity in living cells was investigated by high-resolution, quantitative AFM, which enables to render the cell topography and the Young's modulus simultaneously. Thereby, elasticity profiles of individual cells were generated, which identified different Young's moduli for different actin fiber arrangements. Highly branched actin fibers revealed a higher Young's modulus than regions with linear and parallel actin fibers. However, the Young's modulus also decreases with an increasing fiber-to-fiber distance for parallel fibers. The structure of the actin cytoskeleton is governed by a large number of scaffolding proteins such as α -actinin-1 (A1) and -4 (A4). A knockout of both α -actinins caused a strongly branched basal actin cytoskeleton located around the cell nucleus, as well as a loss of dorsal actin fibers spanning over the nucleus, so-called actin caps. This results in a kind of "fried egg" morphology of the topography and the Young's modulus: these cells were high and soft in the center, but flat and stiff in the periphery.

Furthermore, different functions of A1 and A4 in regulating the actin architecture and thus the mechanical properties of the cells were identified. A1 promotes the formation of linear basal and dorsal actin fibers and therefore, the cells resemble the phenotype of wildtype cells. However, due to the presence of only a few actin caps, these cells showed a reduced Young's modulus. In contrast, A4 promotes the cross-linking of the actin fibers. This caused highly branched peripheral actin fibers, resulting in flat and stiff as well as a high and soft parts of the cells.

The structure of the actin cytoskeleton also changes by natural processes such as cell aging. Comparing the elasticity profile and the actin cytoskeleton of primary human tendon stem progenitor cells (TSPC) of young and aged patients (Y-TSPC and A-TSPC), revealed that structural changes of the actin structure are also reflected by the Young's modulus. Thus, the Young's modulus is a suitable biomarker for cell aging. Compared to Y-TSPCs, A-TSPCs revealed a higher Young's modulus in combination with an increased density of parallel actin fibers. The inhibition of ROCK 1 and 2 in A-TSPCs induced a loosely packed actin cytoskeleton and thus an adaptation of the actin structure back to that of Y-TSPCs. This "structural rejuvenation" was also manifested in a reduced Young's modulus, similar to that of Y-TSPC cells.

Finally, it was shown how Y- and A-TSPC cells influence the mechanical properties of their surrounding matrix. Therefore, Y- and A-TSPCs were cultivated in a 3D polypeptide-based hydrogel and the Young's modulus of the gel was examined. Both cell types increased the Young's modulus of their surrounding matrix. This effect was more evident in A-TSPCs than in Y-TSPCs, which can be considered to be a further characteristic of cell aging. Therefore, in the future, the Young's modulus of 3D constructs could also serve as a biomarker for cell aging and allow to discriminate between young and aged tissue.

CONTENTS

1 INTRODUCTION AND MOTIVATION	1
2 THEORETICAL BACKGROUND.....	4
2.1 INTERPLAY BETWEEN CELL BEHAVIOR AND MATRIX ELASTICITY.....	4
2.2 THE BASEMENT MEMBRANE: COMPOSITION AND MECHANICAL PROPERTIES	6
2.3 THE ACTIN CYTOSKELETON: DETERMINANT OF MECHANICAL PROPERTIES	9
2.3.1 Actin fibers and adhesions sites	9
2.3.2 Structure and function of α -actinins.....	11
2.4 CELL MIGRATION REQUIRES REGULATED SYNCHRONIZED ACTIN REMODELING	13
2.5 CELL AGING OF TENDON STEM/PROGENITOR CELLS	14
2.5.1 TSPCs in 3D hydrogels.....	15
3 ATOMIC FORCE MICROSCOPY: INDENTATION OF ECM AND CELLS	16
3.1 FORCE MAPS AND QUANTITATIVE IMAGING	17
3.2 DETERMINATION OF THE YOUNG'S MODULUS USING A MODIFIED HERTZ-MODEL.....	19
3.3 AFM PARAMETERS FOR INDENTATION EXPERIMENTS	20
3.3.1 Vertical tip velocity for biological samples	21
3.3.2 Relative deformation: influence of the underlying substrate	24
4 RESULTS	27
4.1 THE YOUNG'S MODULUS OF MATRIGEL IS DECREASED BY NETRIN-4	27
4.1.1 Net-4 inhibits the formation of a laminin network.....	28
4.1.2 Net-4 disrupts an existing laminin network	30
4.1.3 Discussion and Conclusion	32
4.2 THE ROLES OF ALPHA-ACTININ-1 AND -4 IN REGULATING THE ACTIN ARCHITECTURE AND YOUNG'S MODULUS	33
4.2.1 Influence of the scaffolding proteins A1 and A4 on cell mechanics.....	34
4.2.1.1 Overall Young's modulus and cell height	38
4.2.1.2 Young's modulus of branched versus parallel actin fiber arrangement	39
4.2.2 Correlation of the cell height and the Young's modulus.....	41
4.2.3 Basal and dorsal actin organization.....	44
4.2.3.1 The roles of A1 and A4 in dorsal and basal actin architecture	44
4.2.4 Actin architecture and adhesion sites guides cell migration	47
4.2.4.1 Cell-cell and cell-matrix contacts and the orientation of actin fibers.....	47
4.2.5 Unorganized actin cytoskeleton hampers collective cell migration	51
4.2.6 Impaired translocation of the mechanosensitive transcription factor MRTF	54

4.2.7	Discussion and Conclusion	56
4.3	INFLUENCE OF CELL AGING ON ACTIN ARCHITECTURE AND CELL MECHANICS	59
4.3.1	Young’s modulus: a biomarker for cell aging.....	60
4.3.2	Cell aging promotes a dense actin architecture	63
4.3.3	ROCK inhibition: a suitable rejuvenating strategy	64
4.3.4	Discussion and Conclusion	65
4.4	YOUNG’S MODULUS OF Y- TSPC AND A-TSPC LADEN HYDROGELS	67
4.4.1	Increased Young’s modulus of cell-laden hydrogels with a bimodal distribution	68
4.4.2	Discussion and Conclusion	69
5	OUTLOOK.....	71
A.	METHODS AND EXPERIMENTAL DETAILS.....	73
B.	LIST OF PUBLICATIONS AND MANUSCRIPTS.....	83
C.	ABBREVIATIONS.....	85
D.	REFERENCES.....	87

1 INTRODUCTION AND MOTIVATION

Tissue consists of both, extracellular matrix (ECM) and cells and is exposed to a variety of mechanical stimuli *in vivo*. For example, shear forces in endothelial vessels [1], compressive forces in cartilage and bone [2, 3], contractile forces in muscle [4] or tensile forces in epithelia [5–7]. Therefore, each tissue exhibits specific biomechanical properties to fulfill its physiological function. Very soft tissues like the brain exhibit < 1 kPa, whereas very stiff tissues like bones reach up to > 1 GPa, as shown in Figure 1 [8–11]. The mechanobiology of tissue is shaped by the interplay of the ECM and cell mechanics. The cells represent the active component, as they can probe their environment and adapt to it by remodeling their cytoskeleton and thus tuning their own elasticity [12, 13]. However, they also remodel their surrounding matrix by the expression of ECM molecules, degeneration of the ECM or migration and spreading and thus force generation within the ECM [14–16].

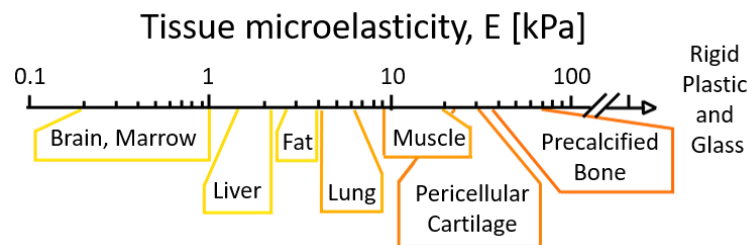


Figure 1: Schematic overview of microelasticity of different tissues in the body, ranging from very soft tissues e.g. < 1 kPa for brain marrow up to very rigid tissue e.g. > 10 kPa for muscle or bone (adapted from [17]).

The perception of cells of the mechanical properties of their surroundings influences cellular processes, e.g. in embryogenesis [18]. Mesenchymal stem cells (MSC) do not differentiate into osteocytes, even if provided with appropriate growth factors when growing on soft substrates [19]. An elasticity gradient guides the spatial arrangement and organization of chondrocytes in the developing growth plate in bones [20]. Therefore, it is not surprising, that when the interplay between matrix and cell elasticity is not balanced, pathological

progression is supported. For example, the invasiveness of cancer is associated with tumor stiffness [8].

Even though the effect of the mechanical properties of the EMC on cell behavior has been and still is investigated intensively, it is also crucial to investigate which cellular components contribute to the mechanical properties of individual cells, the ECM and the composition of both. Over the past, various techniques have been established to evaluate the mechanical properties of biological samples [21]. Micropipette aspiration is a sensitive method to investigate the cell membrane and cytoplasm but is not suitable for cell organelles. Optical tweezers possess a high force sensitivity but only small indentations are possible and the spatial resolution is limited to the size of the bead [22]. Ultrasound and magnetic resonance techniques are non-invasive methods but have only limited spatial resolution [23, 24]. Brillouin microscopy is also a non-invasive technique for biological samples, with an acceptable spatial resolution [25]. Finally, although it is an invasive method, atomic force microscopy (AFM) is one of the best-suited and most versatile techniques to determine the mechanical properties of biological samples under near physiological conditions with high spatial resolution. State of the art AFMs combine Young's modulus measurements and topographic imaging with high measurement speed and high resolution. Nevertheless, measuring the mechanical properties of biological samples is still challenging, since they are highly heterogeneous, often show viscoelastic behavior and are constantly modified by the active cells, making such measurements time-dependent. For example, cells can adjust their elasticity by remodeling their actin cytoskeleton [12, 13]. Furthermore, the mechanical properties of the ECM are never in a steady-state, because cells can express ECM degrading or building proteins or because they can generate local stress by processes like migration. For example, fibroblasts can degrade fibrin gels proteolytically, but at the same time they form rigid fibrin fibers through cellular traction forces and thus they locally enhance the mechanical properties of the gel [16].

The aim of this thesis is to provide a better understanding of the mechanical properties of individual living cells, the ECM and the composition of both, cells embedded in a 3D matrix. In particular, understanding how ECM biomechanics can be modulated by soluble network disrupting and inhibiting factors, as well as gaining insights into the effects of the interplay between actin scaffolding proteins and the actin organization on cell mechanics is the focus of this thesis. In addition, age-associated changes of the actin cytoskeleton and the

corresponding changes in cell mechanics, as well as the effect of matrix remodeling by cells are in the scope of this thesis.

First, the Young's modulus of matrigel supplemented with different concentrations of Netrin-4 (Net-4) was investigated using AFM. Matrigel is a natural ECM-based hydrogel, closely resembling the basal membrane (BM). Net-4 is a soluble BM protein which disrupts existing BM networks and can inhibit the formation of new BM networks. The corresponding decrease of the Young's modulus of the BM caused by Net-4 has been investigated in a dose-dependent manner.

Next, the mechanical properties of cells with different architectures of the actin cytoskeleton, which were induced by the stable knockout of the scaffolding proteins α -actinin-1 (A1) and -4 (A4) or by cell aging, were investigated. The actin cytoskeleton is shaped with the help of multiple scaffolding proteins, such as A1 and A4. In addition, natural processes, such as cell aging influence the integrity and structure of the actin cytoskeleton. For example, tendon stem progenitor cells (TSPC) change their actin cytoskeleton during cell aging [26, 27]. For this purpose, high-resolution data sets, which can clearly resolve cytoskeletal structures within individual cells, were recorded using a new data acquisition mode referred to as quantitative AFM or quantitative imaging (QI) mode. The literature reports Young's modulus values for different cells, ranging from ~ 0.2 kPa for neutrophils up to ~ 100 kPa for cardiomyocytes [28]. However, almost all of these measurements were recorded, at only one or just a few positions of the cell. However, cells are highly heterogeneous, exhibiting distinct cytoskeletal structures and multiple organelles with varying mechanical properties at different locations within the cell. Quantitative AFM provides sufficient spatial resolution, generating Young's modulus profiles to detect these local variations of the structural and mechanical parameters of an entire living cell.

A last set of experiments demonstrates that cells can affect their 3D environment and modify the Young's modulus of their ECM. Here, TSPCs were cultured in a polypeptide based 3D hydrogel (RADA) and changes in the elastic modulus of the gel were investigated.

2 THEORETICAL BACKGROUND

2.1 INTERPLAY BETWEEN CELL BEHAVIOR AND MATRIX ELASTICITY

Cells must continuously sense and quickly adapt to substrate rigidity in a constant feedback loop in order to maintain its physical integrity [29, 30]. However, the underlying processes of how cells perceive their environment is still not completely understood. Most likely, the cells exert small tensile forces and sense the local deformation [31]. By this, substrate elasticity can direct the spatial arrangement and organization of cells within a tissue, affect cell differentiation, morphogenesis and homeostasis as well as the phenotype of the cells, as shown in Figure 2 [11]. Prein et al. have shown a close correlation between ECM stiffness and cellular organization of the developing growth plate in bones. They were able to show a gradient of matrix elasticity that forces the morphogenesis and proliferation of chondrocytes along the longitudinal axis of the limb [20]. In 2006, Engler et al. have shown that the elasticity of the microenvironment plays a central role for the prediction of MSC specification. By cultivating MSCs on collagen I coated polyacrylamide (PA) gels with different elastic moduli they demonstrated, that soft matrices (0.1–1 kPa) mimicking the brain are neurogenic, stiffer matrices (8–17 kPa) mimicking the muscle are myogenic, and rigid matrices (25–40 kPa) mimicking the bone prove to be osteogenic [19], regarding the cell morphology and RNA profiles. In a similar experiment, Park et al. could also show that soft substrates have a greater adipogenic and chondrogenic potential, while stiffer substrates have a stronger myogenic potential for MSCs [32]. This emphasizes the role of substrate elasticity when regulating the differentiation of MSCs towards specific lineages.

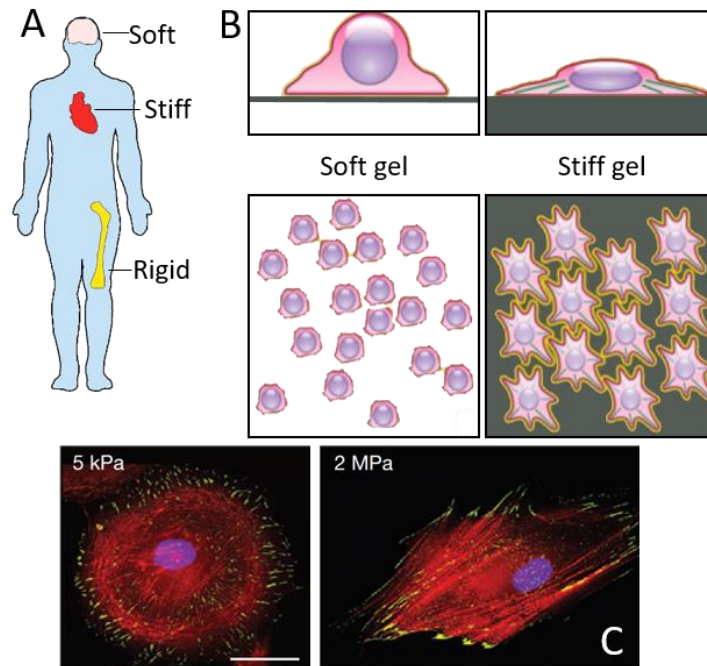


Figure 2: Morphology and actin architecture of cells on soft and stiff substrates. A) Overview over tissues with different rigidities, which can be found in the body. B) Schematic illustration demonstrating how cells adhere and spread on soft (left) and rigid (right) surfaces, displayed in side view (top) and top view (middle) to demonstrate the resulting difference in cell height and the spreading area, respectively. C) Fluorescence images of actin-fibers (red), focal adhesions (green) and cell nucleus (blue) of fibroblasts plated on fibronectin-coated stiff (5 kPa, left) and soft (2 MPa, right) substrates. Scale bar 30 μm . (A and B adapted from [17] and C adapted from [33]).

Furthermore, the phenotype of the cells is strongly influenced by substrate elasticity. If cells grow on soft substrates, they tend to show a roundish cell shape with few pronounced actin fibers. If they grow on a rigid substrate, on the other hand, they are strongly flattened with a dense actin network [17, 34]. As an example, the growth of fibroblasts on substrate of different elasticity is shown in Figure 2 C. On rigid surfaces like glass ($> 1 \text{ GPa}$) or gels with 2 MPa, fibroblasts exhibit a highly polarized cell shape with stable cell edges, pronounced actin fibers localized along the major cell axis and matured focal adhesions elongated along the stress fibers. Whereas on soft substrates with 5 kPa or less, cells display a more circular cell shape with clear cell edges or aligned actin bundles. Also, the cells form an increased number of small adhesion sites distributed over the entire cell [33, 34].

2.2 THE BASEMENT MEMBRANE: COMPOSITION AND MECHANICAL PROPERTIES

ECM is the cell-free network of macromolecules that provides mechanical support and biochemical stimuli for the enclosed cells. ECM consists of about 300 different proteins such as collagens, laminins, proteoglycans (PGs) and glycoproteins providing structural support, but also the necessary elasticity, depending on the tissue [14]. Therefore, the ECM of every tissue exhibits its individual composition and organ-specific mechanical properties. Tissues exposed to high tensile and compressive forces like cartilage or tendons are rich in collagens forming mechanical networks and supportive structures that exhibit a higher elastic modulus, whereas tissues like the lung, are rich in elastic fibers providing certain flexibility [35]. In general, ECM can be classified into two major types, based on their composition and location: (i) the interstitial connective tissue matrix and (ii) the basement membrane (BM). Whereas the interstitial connective tissue matrix surrounds cells, the basement membrane separates the epithelium from the surrounding stroma in every tissue [35].

The basement membrane (BM) is a specialized type of the ECM which is, mostly found at the basal side of the endo- and epithelium, muscle fibers or peripheral axon fibers [36, 37]. The BM forms a ~100 nm thick support structure with a pore size of 10-112 nm [38–40], which acts as a barrier dividing tissues into compartments and comprises a source of matrix-linked growth factors. The BM is connected to cells mainly by integrin receptors which bind laminin and collagen IV [14, 37, 41]. The most abundant proteins in the BM are laminins, collagen IV and the crosslinker nidogen [37, 42]. Collagen IV (Col IV) is a non-fibrillar collagen consisting of six alpha-chains with a length of ~ 400 nm per chain. In contrast to other members of the collagen superfamily, Col IV is uniquely found in the BM [43, 44]. Laminins are heterotrimeric proteins consisting of three disulfide-linked polypeptides, the α , β and γ chains (Figure 3 A). Laminin isoforms are defined by their number, location and size of these independent α , β and γ chains. The chains are divided into long arms and short arms. The long arms (~80 nm) exhibit a helical coiled-coil structure with five C-terminal domains at the α -chain, which comprise the most cell-adhesive sites of laminin. The laminin short arms (~35-50 nm) are not connected to each other within one laminin molecule but are involved in forming laminin networks at the N-terminus creating ternary nodes

(Figure 3B) [45, 46]. Nidogens are glycoproteins of which two isoforms, nidogen-1 and -2 have been identified. Nidogens are crosslinker proteins, that connect the Col IV with the laminin network (Figure 3 B) [47, 48].

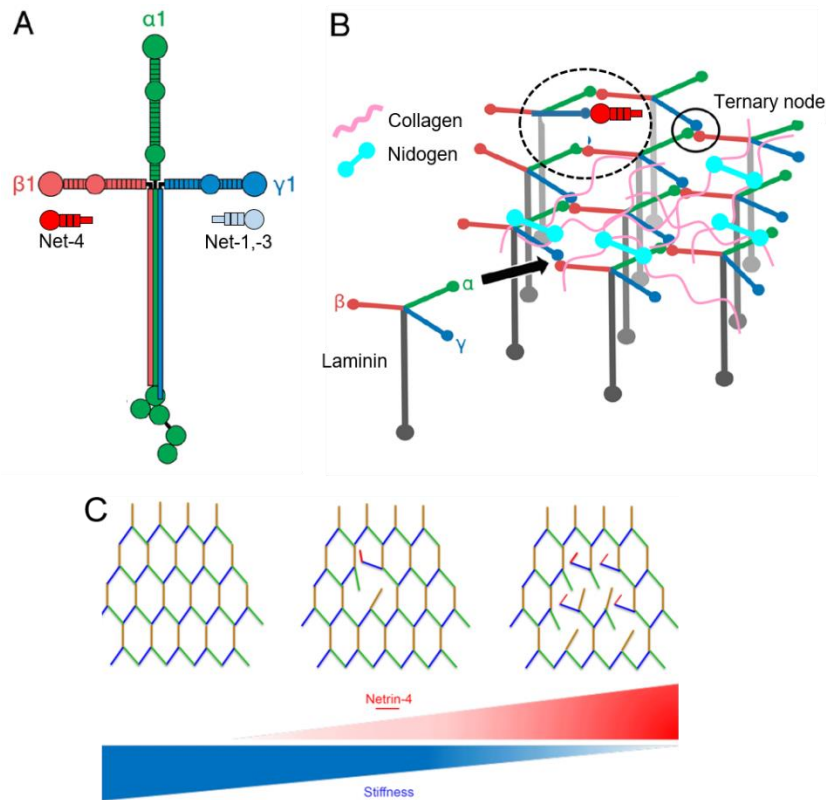


Figure 3: Structure and assembly of laminin and modulation of the BM by Net-4. (A) Laminin, Net 4 (red) with homology to $\beta 1$ chain and Net-1-3 (light blue) with homology to $\gamma 1$ chain. (B) Self-assembly of laminin-111 by creating ternary nodes of the α (green), β (red) and γ (blue) chain (black circle) on Collagen 4 (pink) and disruption of the network by Net-4 by binding the $\gamma 1$ chain (black dotted circle). (C) Modulation of the BM mechanics by Net-4. Net-4 disrupts the laminin-network in a dose-dependent manner, resulting in an increasing pore size and thus a decreased stiffness. (A and B adapted from [46], C taken from [49]).

The BM composition and rigidity can be actively modified, by secretory proteins such as matrix metalloproteinases (MMPs) or by netrins [50, 51]. The netrin family consists of six members. All netrins exhibit a homology to the laminin short arms. Netrin-1, -3 and -5 show a homology to the laminin $\gamma 1$ chain, whereas netrin-4 (Net-4) exhibits a higher homology to the $\beta 1$ chain. Because of their homology to the laminin chains, all members of the netrin family were considered to have similar functions. However, the outstanding function of Net-4 was recently shown by Reuten et al. [49, 51]. While Net-1 does not bind native laminin,

Net-4 can inhibit laminin polymerization by binding to the $\gamma 1$ chain. Through competitive binding, it can also disrupt an already existing laminin network. Net-4 is therefore a key regulator of basal membrane integrity [51, 52]. By binding to laminin, Net-4 opens the laminin node complex and blocks the $\gamma 1$ chain, thereby inhibiting the rebinding of the laminin molecules [49] and thereby changes the mechanical properties of the BM, what will be discussed in 4.1.

Alterations of the BM architecture and molecular composition and thus the mechanical properties are fundamental for many physiological processes, such as the transmigration of immune cells during the inflammatory response, which have to pass the BM locally [53]. However, the mechanical relevance of the ECM is manifested by a broad range of diseases. For example, the depletion of genes encoding the abundant ECM proteins fibronectin or collagen results in tissue defects which are often embryonic lethal [14, 54, 55]. Abnormal elastic properties can also lead to a number of other pathological events, like fibrosis or osteoarthritis. During pulmonary fibrosis, excessive ECM synthesis leads to an increased elastic modulus and shortness of breath [56, 57]. Moreover, there is an increased risk of developing cancer in a variety of tissues with an increased elastic modulus of the ECM [58–60].

2.3 THE ACTIN CYTOSKELETON: DETERMINANT OF MECHANICAL PROPERTIES

2.3.1 ACTIN FIBERS AND ADHESIONS SITES

The actin cytoskeleton consists of actin filaments, organized into diverse structural arrays by numerous accessory proteins (Figure 4). Because actin fibers have to fulfill a variety of different functions, there are several fiber types, which are not all present in the cell at the same time. At the leading edge of a migrating cell, a flat network forms the lamellipodium, which is one major „engine“ of cell migration, because within the lamellipodium polymerizing actin fibers push against the cell membrane in direction of motion. A thin-layered mesh with fine actin fibers, called the cell cortex, coats the inner side of the cell membrane and thus provides the cell shape and stability. Parallel-aligned bundles of actin form the basis of filopodia, which appear as finger-like structures on the front side of a migrating cell and which are important for a cell to probe its environment. A three-dimensional network of thick basal or dorsal actin bundles, so-called stress fibers, transmit intracellular forces such as contractile forces generated by motor proteins of the myosin-family. They connect to the substratum or neighboring cells via focal adhesions (FAs) and adherent junctions (AJs), respectively [61–64].

Via FAs and AJs, cells are in permanent contact with the ECM and with neighboring cells, from where they obtain mechanical signals. FA formation and maturation are force-dependent mechanisms, making adhesion sites to crucial force sensors of a cell. There are different stages of FA-development: early nascent adhesion sites exhibit a high protein turnover whereas mature adhesion sites show a lower turnover rate, but higher stability and a larger size. On rigid substrates, for example, cells exhibit large and stable FAs that sustain high forces, whereas cells on soft substrates only develop small but dynamic FAs of low mechanical strength [31, 34, 65, 66]. This is in line with the observation that reduced traction forces in cells lead to the disassembly of FAs [67]. Thus, assembly and disassembly of FAs are highly sensitive to extracellular mechanical signals and intracellular forces that affect cell shape, cell stiffness, migration behavior, and multiple other cellular processes guided by the actin cytoskeleton and adhesion sites [68].

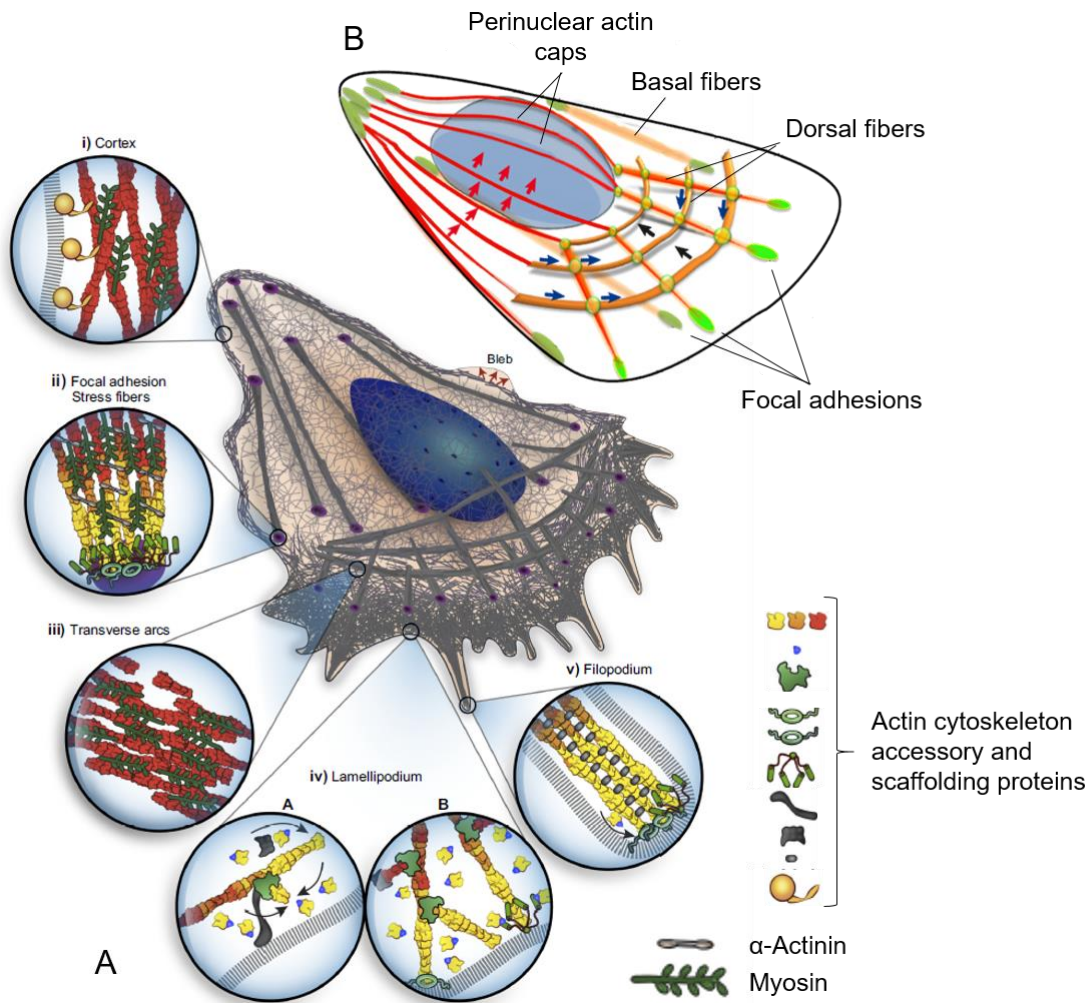


Figure 4: Actin cytoskeleton and stress fiber types. A) Schematic representation of the actin cytoskeleton and the different actin fiber subtypes: myosin-containing actin fibers in the contractile units (i-iii), highly aligned and parallel fibers in the filopodia (v) and branched actin fibers in the cortex and the lamellipodium (I and iv). The actin scaffolding protein α -actinin is mainly present in contractile stress fibers (ii). Other accessory and scaffolding proteins of the actin cytoskeleton are illustrated on the right. B) Schematic representation of the process of actin cap formation. Peripheral stress fibers are pulled over the nucleus, resulting in actin caps. (A adapted from [61] and B adapted from [69]).

2.3.2 STRUCTURE AND FUNCTION OF α -ACTININS

α -actinins are well-known cytoskeletal scaffolding proteins found in all mammal cells. The α -actinin-family belongs to the spectrin superfamily and consists of 4 members (α -actinin 1-4). While α -actinin-2 and -3 are exclusively expressed in muscle cells, the non-muscle α -actinins-1 and -4 are expressed ubiquitously.

An α -actinin monomer consists of an N-terminal actin-binding head domain (ABD), a central rod domain with four-helical spectrin-like repeats (SR1–SR4) and a C-terminal calmodulin-like (CaM) tail domain with two calcium-binding EF-hand motifs [70–72]. Dimerization of two α -actinin monomers via the rod domain results in antiparallel heterodimers (Figure 5). This is essential for the biological function of α -actinin-dimers since they exhibit functional domains at both ends. By this, α -actinins can bind and crosslink actin filaments but also bind the cytoplasmic domain of β -integrin and tether them to cell adhesion sites [73, 74]. Previous studies have demonstrated that α -actinin-1 and -4 are associated with stress fiber formation, focal adhesion maturation, cell polarization and other cellular processes [30, 75]. They provide a multivalent platform by hosting numerous interaction sites within the rod domain for many other scaffolding proteins e.g. vinculin [71, 76]. Therefore, α -actinins are crucial proteins providing stability at the cell-substrate interface and at the cell-cell contacts and provide the integrity of the actin cytoskeleton and control the cell shape [77, 78].

In both functions, as a crosslinker and as a linkage of actin to the adhesion sites, α -actinins are suspected to act as force and elasticity regulators. On the one hand, α -actinins can be stretched and unfolded in a force-dependent manner and thus are thought to absorb tension at the adhesion sites. As a crosslinker, they provide a certain elasticity for the actin fibers, by the number of α -actinin molecules between the actin fibers [79]. On the other hand, stretching of the α -actinin dimers promotes the binding of stabilization proteins such as vinculin and thus enables maturation of the adhesion sites [30]. Therefore, α -actinins seem to be involved in the mechanosensory cascade and the transmission and translation of mechanical signals.

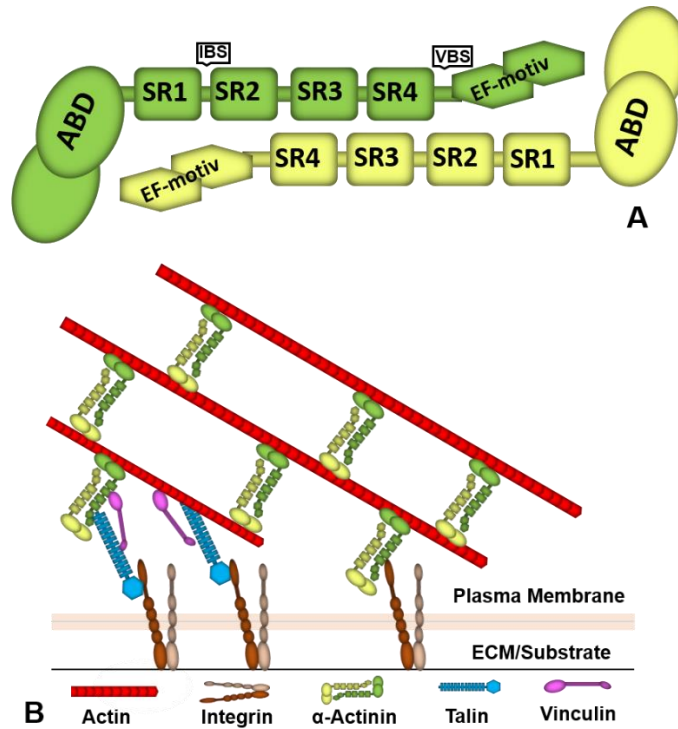


Figure 5: Schematic illustration of an α -actinin homodimer (A), consisting of two α -actinin monomers (green and yellow) with one actin-binding site (ABS) at the head, a rod of spectrin repeats (SR1-SR4), and the EF-hand motifs. B) Scaffolding and tethering function of α -actinin within the cell. In its tethering function, α -actinin can bind directly to integrin by the integrin-binding site (IBS) between SR1 and SR2 or indirectly via other proteins such as talin and vinculin. In its scaffolding function, α -actinins can bind and crosslink actin fibers by the ABD at both ends of the dimer.

Although α -actinin-1 and -4 exhibit 87 % amino-acid homology, their divergent functions were recently discussed [80, 81]. Their distribution within a cell differs at least in highly motile cells. α -actinin-1 seems to be evenly distributed along the actin stress fibers in motile cells, whereas actinin-4 was found to be more concentrated in circular dorsal ruffles and seems to be involved in the initial adhesion [30, 70, 75, 78, 82]. α -actinin-1 but not -4 rescues the phenotype of the cells related to the basal actin cytoskeleton and FA-distribution, and both actinins suppress random cell migration [83, 84]. The individual roles of α -actinin-1 and -4 regarding the biomechanical properties of the cells and the apical actin cytoskeleton will be discussed in 4.2.

2.4 CELL MIGRATION REQUIRES REGULATED SYNCHRONIZED ACTIN REMODELING

The translocation of cells is highly dynamic and a fundamental physiological process which is a prerequisite for tissue homeostasis. Therefore, the interaction of cells with the environment is crucial for controlled cell migration and tissue organization. Besides remodeling the intracellular actin architecture, migration is another essential mechanism for cells to adapt to their mechanical or molecular environment. The ability of cells to move forward is a key process during morphogenesis, wound healing or immune response. Cells have to migrate to the site of inflammation during an immune reaction or promote wound closure [85, 86]. Migration plays also a major role in pathogenic tissue like in a tumor, where cells metastasize through the narrow epithelial layer [87, 88].

Cell migration can be classified into single and collective cell migration. While mature cell-cell contacts play an important role for the communication in collective migration, because neighboring cells affect the behavior of each other, the adhesion sites in single-cell migration are limited to cell-substrate connections [31, 86]. The organized assembly and disassembly of actin fibers and adhesion sites as well as the remodeling of the entire actin cytoskeleton by scaffolding proteins, such as α -actinins, are determinants for persistent cell migration [83, 84]. Therefore, intracellular forces are generated by contractile actomyosin fibers and transmitted to the adhesion sites, allowing the cell to probe and react to elasticity variations of the ECM during cell migration, called „durotaxis“. Of course, there are also molecular factors, which can guide cell migration, a process called „chemotaxis“ [31, 89]. Thus, in addition to biochemical pathways, cell migration is a major force-driven process.

2.5 CELL AGING OF TENDON STEM/PROGENITOR CELLS

Aging influences the functionality, maintenance of homeostasis and the regenerative ability of cells and tissue [27, 90]. Age-related impairments are associated with a decrease in the stem cell pool and thus the availability of potent cells [91]. Mesenchymal stem cells (MSC) are adult stem cells found in the bone marrow and other tissues. MSCs are multipotent progenitor cells and thus are able to differentiate into different cell types. Therefore, MSCs are a promising source for tissue regeneration [92, 93]. Studies on MSCs showed age-related changes including reduced proliferation and altered differentiation potential [94–97]. Kasper et al. reported a decreasing cell pool of MSCs with increasing age [98]. They also showed increased senescence, reduced antioxidant defense, changes in cytoskeletal organization and low migration capacity.

Tendons connect muscles to bones and thereby enable joint movement. Mature tendon is characterized by a low cell density and a high content of extracellular matrix (ECM) [99]. However, with increasing age, tendons become prone to injuries. Tendon aging and overload are the main reasons for tissue degeneration and thus promote tendon injury [100–102]. Tendon repair is particularly protracted in older patients and it is difficult to restore the original strength of the tendon. Up to date, there is no medical treatment strategy to support tendon repair and restoration of its normal physiological function after injury, which often causes pain and leads to scar tissue [103]. Thus, for prospective treatment of tendon injury, it is crucial to understand the age-related effects and investigate reprogramming strategies to achieve young cell characteristics and regeneration capacity in aged-cells.

Tendon stem/progenitor cells (TSPCs) were identified by Bi et al. in 2007 [104]. They show classic MSC characteristics (surface antigenic, self-renewal, clonogenicity and three-line differentiation capacity), but unlike MSCs, TSPCs express tendon-related genes such as scleraxis and tenomodulin and are capable of forming tendon-like tissues when implanted in vivo [27, 104]. In 2013, Kohler et al. investigated human TSPC derived from Achilles tendon biopsies of young and healthy individuals (Y-TSPC) and aged patients with functionally degenerated tissues (A-TSPC) [27].

Because reprogramming of aged tendon cells to younger cell characteristics might help to improve treatment strategies in the future, transcriptome analysis was conducted and a transcriptomal shift of a number of genes regulating cell adhesion, migration, the actin cytoskeleton and specifically an upregulation of the kinases ROCK 1 and 2 was discovered in A-TSPCs [27]. The Rho-associated kinases ROCK 1 and 2 are effector proteins of the GTPase Rho, a key player in cytoskeletal organization by regulating stress fiber formation and cell contraction [105]. ROCK inhibition was described to alleviate senescence and thus could be a new approach in treating age-related diseases [106]. For TSPCs it could be shown, that treatment of A-TSPCs with a ROCK-inhibitor reconstitutes cell morphology and other characteristics of young cells, such as actin content, migration velocity, and cell spreading [27]. The mechanical properties of TSPCs during cell aging and after ROCK treatment will be discussed in 4.3.

2.5.1 TSPCs IN 3D HYDROGELS

In a 3D environment, cells behave differently than in 2D culture because the interplay between cells and their surrounding matrix plays an important role in cellular behavior and ECM remodeling [107]. On the one hand, cells can modify the ECM, e.g. by expressing the network-disrupting protein Net-4 in the BM or ECM supporting proteins such as collagens [52, 108, 109]. ECM can guide cell behavior and characteristics mainly by its microenvironment [107, 110, 111]. It has been shown, that ECM composition has a rejuvenating effect on cells [112, 113] and that providing a well-defined 3D microenvironment, composed of a hydrated biopolymer network similar to that found in the ECM can rejuvenate TSPCs [114]. The hydrogel, analyzed in this thesis, contains the self-assembling peptide RADA. RADA peptides consist of the amino acids arginine, alanine and aspartic acid [115], creating a fibrous hydrogel with a pore size between 5–200 nm and a water content of ~99 %. This constitutes a microenvironment, similar to the natural ECM architecture [38–40]. Therefore, RADA 3D hydrogels have been used for multiple cell systems already [116, 117]. The mechanical properties of TSPC-laden hydrogels will be discussed in 4.4.

3 ATOMIC FORCE MICROSCOPY: INDENTATION OF ECM AND CELLS

The development of the atomic force microscope (AFM) by Binnig and colleagues enables topographic imaging down to atomic resolution as well as the application and measurement of forces from the nanonewton down to the piconewton range and thus the determination of mechanical properties of biological systems [118, 119]. Unlike other methods, the AFM allows measuring sample topography and biomechanical properties at the same time under nearly physiological conditions. The principle of the AFM is based on a flexible cantilever spring with a tip, scanning or indenting a sample. Changes in sample height or indentation depth lead to a bending of the cantilever and thus to a deflection of the laser, which is reflected from the backside of the cantilever onto a position-sensitive segmented photodiode (Figure 6 A). Indentation data are displayed as force versus distance curves (FD-curves) as shown in Figure 6 B, where the cantilever tip indents into the sample until a predefined threshold force is reached.

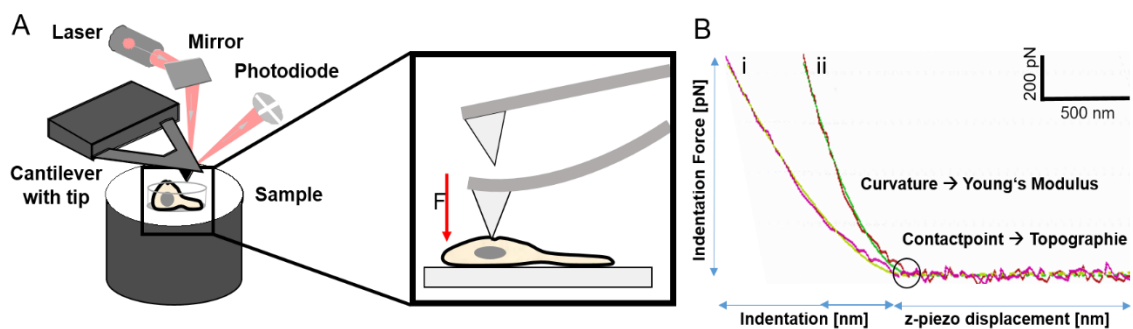


Figure 6: Working principle of the atomic force microscope (AFM), with a cell as a sample (A) and exemplary force-distance (FD) curves (B). The FD-curves were recorded on a soft area (i) and a rigid area (ii) of a cell. The contact point (black circle) and the curved part of the FD-curve (green) can be used to determine the sample height and the Young's modulus, respectively. (A adapted from [120]).

3.1 FORCE MAPS AND QUANTITATIVE IMAGING

The FD-curves collected from several indentation measurements following a given two-dimensional pattern on a sample are called a force map, also known as force volume, originally published by Radmacher and colleagues in 1996 [121]. Typically, during force mapping the z-piezo moves with a constant velocity while an FD-curve is recorded and rests at a constant z-position during the x-y-movement to the next pixel. Using soft AFM cantilevers, as they are used for biological samples, hydrodynamic drag of the cantilever in the aqueous medium and the high accelerations at the turning points of this triangular excitation of the z-piezo in combination with low resonance frequencies of the cantilever limit the pixel-to-pixel measuring time, making high resolution force maps slow and time-consuming. For example, a force map containing 256 x 256 measurement points recorded with a constant z-piezo velocity of 10 $\mu\text{m/s}$ and a z-traveling distance of up to 15 μm takes about 55 h. However, living biological systems like cells are highly dynamic samples. By rearranging their cytoskeleton, they do not only change their shape and topography but also their position on the sample and their mechanical properties. Because of the high measurement times, classical force maps can be applied to entire living cells only at low resolution (typically up to 32 x 32 measurement points), or only small sections of the cell can be mapped at a resolution resolving, for example cytoskeletal structures, as shown in Figure 7 A.

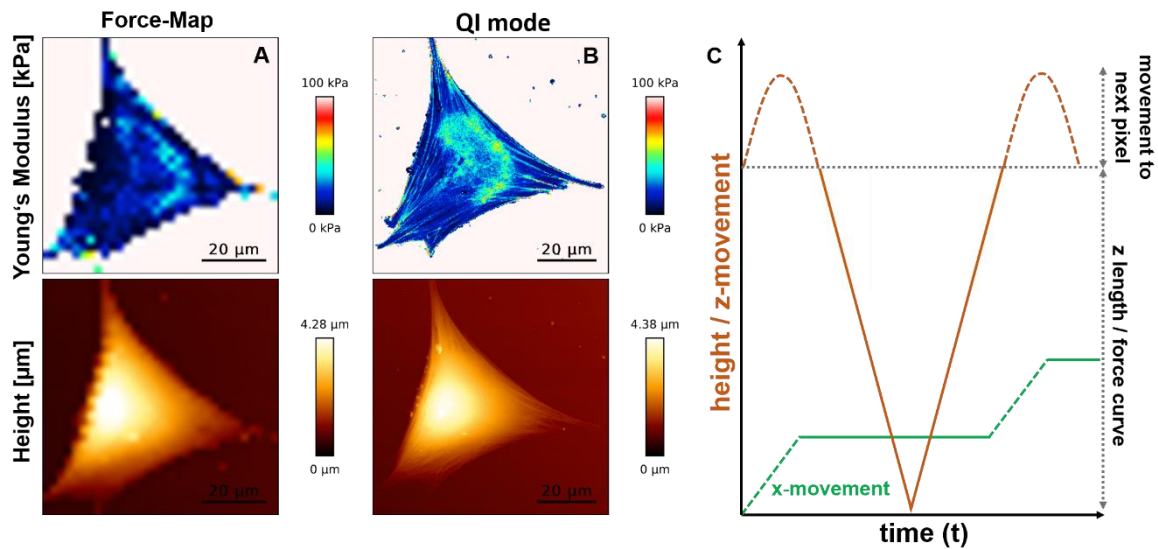


Figure 7: Young's modulus and cell height extracted from a classical force-map (A) and the quantitative imaging (QI) mode (B). A) Classical force-map: 32×32 FD-curves, vertical tip velocity $15 \mu\text{m/s}$ and B) QI mode: 256×256 FD-curves, vertical tip velocity $300 \mu\text{m/s}$. The Young's modulus (top row) was calculated using a modified Hertz model and height images (bottom row) were determined from the contact point. C) Schematic overview of the z- and x-piezo movement during the QI mode. The orange line displays the z-movement (height) and the green line displays the x-movement (pixel position). A whole FD-curve is recorded during no x (or y) movement (C adapted from [122]).

To overcome this limitation and allow for faster and thus high-resolution FD-curve recording on living cells, new algorithms for the cantilever movement have been developed, replacing the triangle (constant velocity) z-movement of the cantilever by a sinusoidal or parabolic movement which avoids high accelerations of the free cantilever. In addition, the lateral movement of the free cantilever is carried out while the cantilever still travels in z-direction (Figure 7C) [122, 123]. The quantitative imaging (QI) mode used in this thesis allows for simultaneous measurement of the topography (called height) and the Young's modulus. The QI mode provides a complete FD cycle consisting of an indentation and a retraction curve at each x-y-position. Topography and elastic modulus are usually determined using the indentation part of the FD-cycle. Because no lateral forces are exerted to the soft cell membrane, the QI mode enables topographic imaging of living cells with a high spatial resolution. In addition, due to the high speed, cells can be mapped extremely fast, so that cellular remodeling or migration is no longer a problem and entire cells can be investigated with a spatial resolution detecting cytoskeletal structures, such as actin bundles.

3.2 DETERMINATION OF THE YOUNG'S MODULUS USING A MODIFIED HERTZ-MODEL

The restoring force as a function of the indentation depth of an elastic sample can be calculated based on a theoretical model proposed by Heinrich Hertz. The original Hertz model describes the force as a function of deformation of two homogeneous, isotropic and elastic spheres pushed against each other [124]. Sneddon modified this model for different indenter geometries penetrating an infinite elastic half-space [125]. Based on the Hertz model, Sneddon derived relations between the force and the indentation depth for a flat cylinder, a paraboloid and a cone used as indenter geometry. In this thesis, cantilevers with a four-sided pyramidal or nearly a conical tip geometry were used. For a conical indenter geometry, the relationship between force and indentation depth can be expressed as:

$$F(d) = \frac{2}{\pi} \cdot \frac{E \cdot \tan(\alpha)}{(1-\nu^2)} \cdot d^2 \quad (1)$$

Here, F is the force, E is the Young's modulus, α is the half-opening angle of the cantilever tip, d is the indentation depth, and ν is the Poisson ratio (assumed to be 0.5 for biological samples) [126, 127]. Bilodeau later modified the Hertz model for a four-sided pyramidal indenter [128]. For this indenter geometry, the relationship between force and indentation depth can be expressed as:

$$F(d) = \frac{1.4906 \cdot E \cdot \tan(\alpha)}{2 \cdot (1-\nu^2)} \cdot d^2 \quad (2)$$

Before applying the Hertz model, FD-curves have to be converted to force indentation (FI) curves by subtracting the cantilever deflection from the movement of the z-piezo, which is recorded by the AFM. To extract the Young's modulus, only the indentation part of the curves is considered.

3.3 AFM PARAMETERS FOR INDENTATION EXPERIMENTS

Determining the Young's modulus of biological samples is challenging, due to the sample properties and active or passive processes of living systems. As mentioned before, cells can react to external forces through active processes like the remodeling of the actin cytoskeleton and thus can tune their own elasticity [12, 13, 129]. The modified Hertz models consider the sample as an isotropic, homogenous and linear elastic infinitely thick half-space with no deformation of the indenter itself [130]. However, due to their composition of numerous structural and molecular components, cells and ECM are usually very heterogeneous samples. They not only exhibit linear elastic but also viscoelastic behavior [129, 131]. Moreover, biological samples often have a sample thickness of only a few micrometers. High loading forces on very thin samples, such as cell edges and protrusions could increase the apparent Young's modulus due to contributions from the underlying substrate. But also a high indentation depth at high regions of the cell might lead to a displacement of intracellular structures such as the nucleus, resulting in apparently softer values [132]. Therefore, the Young's modulus of biological samples is complex and depends on multiple factors such as the applied force, the loading-rate, the timescale of the experiment and so on [12]. Thus, it is important to find a balance between loading velocity and loading force for measuring living cells and other biological samples.

3.3.1 VERTICAL TIP VELOCITY FOR BIOLOGICAL SAMPLES

Due to the viscous part in viscoelastic materials, there is a time-dependent material flow which leads to a dependence of the apparent Young's modulus on the indentation velocity. However, cells also have the ability to restore their original shape, even after viscous deformation [133]. In this thesis, the effect of different vertical tip velocities was systematically investigated. For these investigations, matrigel and living cells were used as samples and tip velocities were varied from 5 – 75 $\mu\text{m/s}$ and 20 – 500 $\mu\text{m/s}$ for matrigel and cells, respectively, with a maximal loading force of 1 nN in both cases.

First, matrigel was examined at 5 different velocities: 5, 15, 25, 50 and 75 $\mu\text{m/s}$ (Figure 8). Force maps were recorded with the respective vertical tip velocity at different regions on one matrigel sample, with a lateral distance of 500 nm between two measurement points. A nominal spring constant of 0.03 N/m was used.

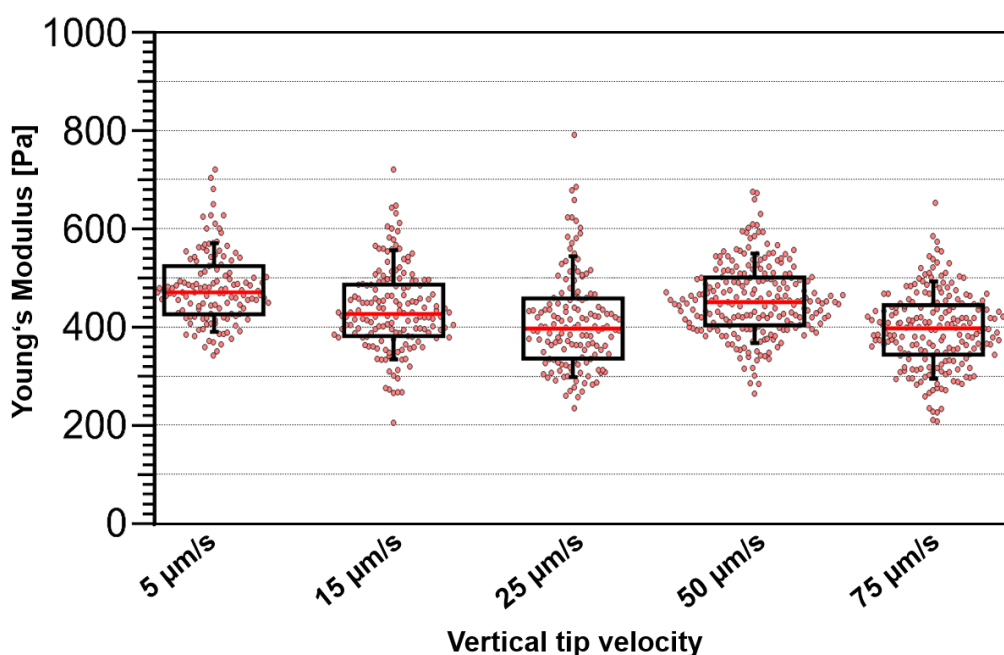


Figure 8: Young's modulus of matrigel at different vertical tip velocities: 5 $\mu\text{m/s}$, 15 $\mu\text{m/s}$, 25 $\mu\text{m/s}$, 50 $\mu\text{m/s}$ and 75 $\mu\text{m/s}$. A scan area of 10 x 10 μm with 20 x 20 FD-curves and a maximal loading force of 1 nN was mapped. Whisker boxplots display the 10 to 90 percent limits (black lines with end caps), the 25 to 75 percent quantile (black unfilled boxes) and the median (red line) of the Young's modulus. The frequency distributions of the Young's modulus (colored scatter dot plots) show the accumulation of measured values. For data analysis, the JPK software (version 6.0.69) was used. The Young's modulus was derived from the first 500 nm of the indentation part of the curves using a modified Hertz model.

Matrigel did not show a significant dependence of the Young's modulus on the indentation velocity. The values measured at the different cantilever velocities vary between 400 and 480 Pa and thus lie within the normal bandwidth (about $450 \text{ Pa} \pm 200 - 300 \text{ Pa}$) reported in the literature for AFM indentation measurements on matrigel [134]. In this thesis, the different cantilever velocities were tested in different regions of one gel. The lowest velocity of $5 \text{ } \mu\text{m/s}$ was chosen for the further investigation of matrigel because measurements on matrigel are not time-critical like the measurement of living cells and this velocity allows direct comparison with current literature values [51, 134].

For living human umbilical vein endothelial cells (HUVEC), Weber et al. could recently show a dependency between the apparent Young's modulus and the cantilever velocity in the range of $0.5 - 20 \text{ } \mu\text{m/s}$ [135]. However, they performed AFM-measurements in the region of the nucleus only. Therefore, there was no need for higher velocities than $20 \text{ } \mu\text{m/s}$. In this thesis, high-resolution elastic modulus and topography maps of living cells were recorded. To avoid excessive measurement times, vertical tip velocities ranging from $20 \text{ } \mu\text{m/s} - 500 \text{ } \mu\text{m/s}$ were investigated on living murine NIH3T3 fibroblasts (Figure 9). For the cells, a slight dependence of the Young's modulus and the indentation depth on the vertical tip velocity was observed. The median of the Young's modulus increased with increasing vertical tip velocity from $\sim 30 \text{ kPa}$ for $20 \text{ } \mu\text{m/s}$ to $\sim 40 \text{ kPa}$ for $300 \text{ } \mu\text{m/s}$. Thus, at high vertical tip velocities of $100 \text{ } \mu\text{m/s}$ and $300 \text{ } \mu\text{m/s}$, a slightly higher Young's modulus combined with a slightly smaller indentation depth was observed. This increased apparent Young's modulus of the cells at increasing tip velocities reflects the viscous part of the cells elasticity. The quality of the force-distance curves at tip velocities of $500 \text{ } \mu\text{m/s}$ was not sufficient to reliably extract force-indentation curves and thus the Young's modulus. These values are only shown for the purpose of completeness. Even though an increased apparent Young's modulus of about 30 % was measured for $300 \text{ } \mu\text{m/s}$ compared to $20 \text{ } \mu\text{m/s}$, a vertical tip velocity of $300 \text{ } \mu\text{m/s}$ requires the shortest measurement time, while still providing reliable force-indentation curves. Therefore, this velocity was chosen for all following experiments performed on living cells.

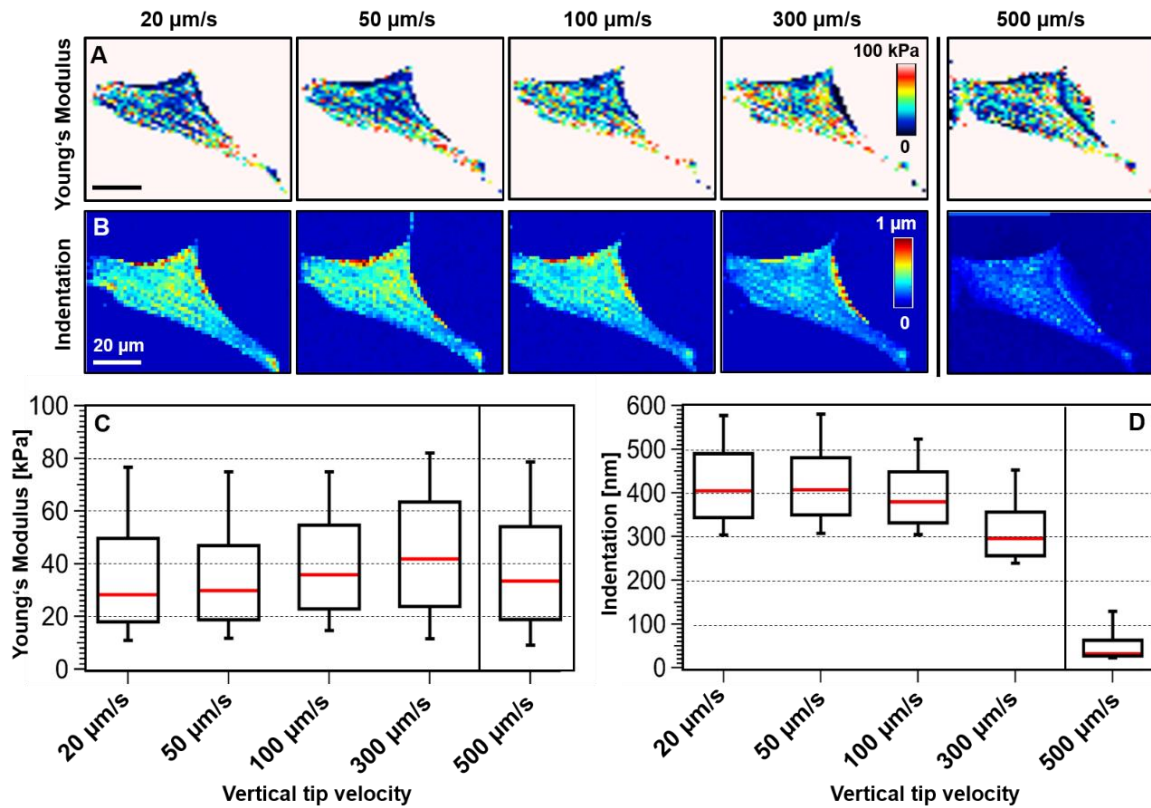


Figure 9: Young's modulus and indentation depth of a NIH3T3 wildtype cell at different vertical tip velocities: 20 $\mu\text{m/s}$, 50 $\mu\text{m/s}$, 100 $\mu\text{m/s}$, 300 $\mu\text{m/s}$ and 500 $\mu\text{m/s}$. A scan area of 80 x 80 μm with 60 x 47 force curves and a maximal loading force of 1 nN was mapped. A) Color-coded map of the Young's modulus at the different vertical tip velocities, color map: 0-100 kPa. B) Color-coded map of the indentation depth at the different vertical tip velocities, color-coded map: 0-1 μm . C) Young's modulus and D) indentation depth represented in a whisker boxplot that displays the 10 to 90 percent limits (black lines with end caps), the 25 to 75 percent quantile (black unfilled boxes) and the median (red line). The Young's modulus and indentation depth for 500 $\mu\text{m/s}$ are only shown for completeness because at these velocities, the FD-curves could not be processed properly. For data analysis, the JPK software (version 6.0.69) was used, and the Young's modulus was derived from the indentation part of the curves using a modified Hertz model.

3.3.2 RELATIVE DEFORMATION: INFLUENCE OF THE UNDERLYING SUBSTRATE

When using the Hertz-model for the determination of the Young's modulus of thin samples such as single cells, the possible influence of the underlying substrate has to be considered. For homogeneous systems, such as gelatin hydrogels, the influence of the underlying substrate on the apparent Young's modulus of the gel was determined as a function of indentation depth by Domke and Radmacher [136]. For their gelatin hydrogels, they found that the modified Hertz model for a conical indenter can be used to reliably extract the Young's modulus of thick gels ($> 1\mu\text{m}$) even at indentations of more than 18 %. For thin gels, on the other hand, the apparent Young's modulus is influenced by the underlying substrate even at small loading forces [136]. For thin gelatin films (120-180 nm), an effect of the underlying substrate was observed at an indentation depth of 25 % of the sample thickness. However, for these samples, 25 % of the sample thickness was the minimum indentation depth that could be tested.

For inhomogeneous samples, such as living cells, with varying height and elasticity, the situation is much more complex. However, according to the literature, for indentation depths up to 10% -18 % of the sample thickness, the influence of the substrate should be negligible [132, 136]. To test, whether the Young's modulus of the cells is influenced by the underlying substrate in the data presented in this thesis, force maps were recorded on living NIH3T3 wildtype and actinin 1& 4 knockout (A1/A4 KO) murine fibroblasts using the QI mode with a constant tip velocity of $300\ \mu\text{m/s}$, a maximum loading force of 1 nN at a lateral resolution of one force curve every 391 nm (Figure 10).

The relative deformation was calculated by subtracting the absolute indentation at 5% and 95% of the maximum loading force for each pixel and dividing the height difference of ($H_{5\%} - H_{95\%}$) by the cell height at 5% of the maximum indentation force $H_{5\%}$. The values of 5% and 95% were chosen because in the first case, at 50 pN (5% of the maximum loading force) the cell height could be obtained without the contact point noise frequently occurring at 0 nN. In the second case, because at the maximum indentation force (100%) often small overshoots in the force-distance curves occurred, due to the high vertical tip velocity of 300 $\mu\text{m/s}$. This also led to fluctuating height values, whereas the height values obtained at 950 pN (95% of the maximum indentation force) were more stable.

$$\text{Relative Deformation} = \frac{H_{5\%} - H_{95\%}}{H_{5\%}} \cdot 100 \quad (3)$$

In Figure 10, the corresponding height images at 50 pN and 950 pN are depicted together with the corresponding relative deformation images. The surface of the cells was visualized nicely at 50 pN, representing nearly the true cell height. In contrast, the height image at 950 pN revealed rigid cell components like fibers of the cytoskeleton. The results show that the maximal relative deformation lies around 14 %, accumulated mainly at the higher parts of the cells ($>1 \mu\text{m}$). According to Domke and Radmacher, this indentation is small enough to ensure that there is almost no influence of the underlying substrate on the calculation of the Young's modulus using a modified Hertz model at a loading force of 1 nN and a vertical tip velocity of 300 $\mu\text{m/s}$.

ATOMIC FORCE MICROSCOPY: INDENTATION OF ECM AND CELLS

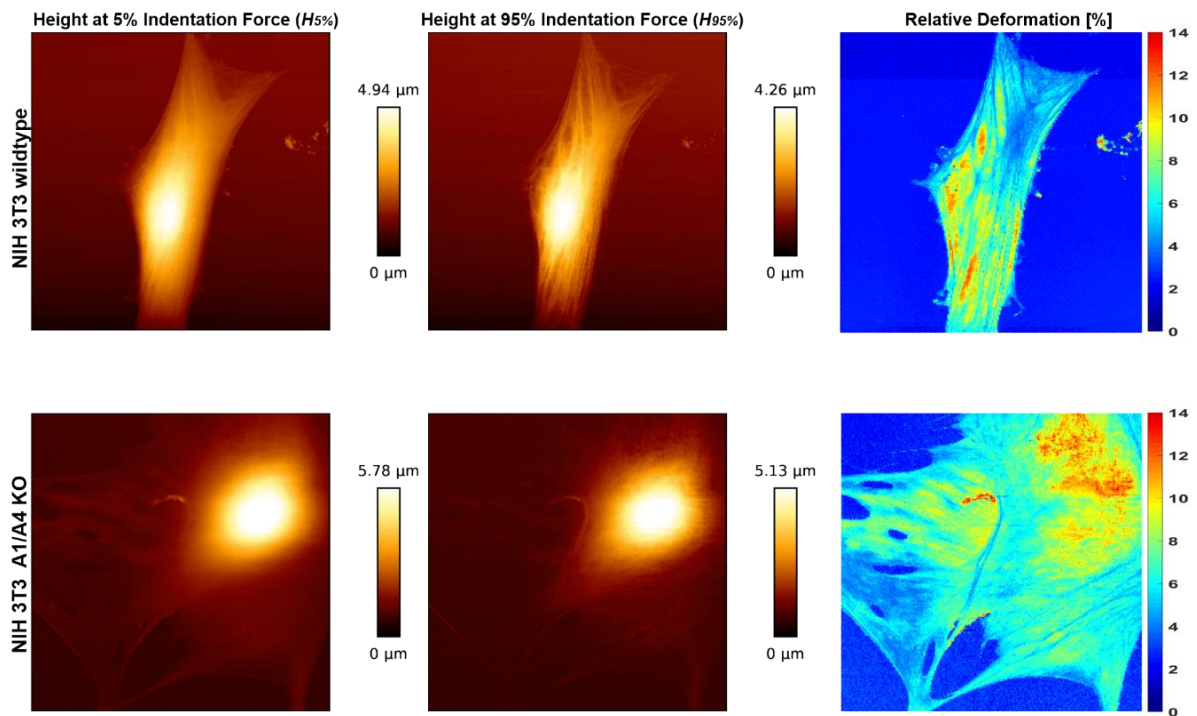


Figure 10: Cell topography at 5% ($H_{5\%}$) and 95% ($H_{95\%}$) (left and middle, respectively) of the maximal indentation force and relative deformation in %, (right) of a living NIH3T3 wildtype (top) and A1/A4 KO fibroblasts (bottom). A scan area of 100 x 100 μm with 256 x 256 FD-curves, a maximal loading force of 1 nN and a vertical tip velocity of 300 $\mu\text{m}/\text{s}$ was mapped. For data analysis, the JPK software (Version 6.0.69) was used. Scale bar 20 μm .

4 RESULTS

4.1 THE YOUNG'S MODULUS OF MATRIGEL IS DECREASED BY NETRIN-4

To investigate the function of Net-4 as a regulator of the Young's modulus of the BM, matrigel was used as the model system for the BM. Matrigel is an artificial matrix resembling the BM, which consists of a soluble extract of BM proteins (approximately 60% laminin, 30% collagen IV) obtained from the Engelbreth-Holm-Swarm (EHS) mouse tumor [137]. Matrigel is liquid at temperatures below 10 °C and polymerizes rapidly to a BM resembling hydrogel at temperatures above 22 °C [138]. The Young's modulus of matrigel is described in the literature with $\sim 450 \pm 230$ Pa [134]. In the following section, both potential functions of Net-4 as a regulator of the BM mechanics have been investigated: i) the inhibition of the polymerization of new BM networks and ii) the degradation of existing BM networks, by the determination of the Young's modulus of Matrigel in the presence of Net-4 using the AFM. The results of the following chapter are based on manuscript 2 listed in list of publications and manuscripts.

4.1.1 NET-4 INHIBITS THE FORMATION OF A LAMININ NETWORK

First, a mixing experiment was carried out to investigate, whether Net-4 can inhibit the formation of a new laminin network in a concentration-dependent manner. For the mixing experiments, 100 μ l of cold liquid matrigel were mixed with Net-4 prior to polymerization. As a control, a sample of matrigel was mixed with the same amount of PBS instead of Net-4. To ensure proper polymerization, the matrigel samples were incubated at 37 °C for 30 min and then covered with PBS at room temperature (RT) for AFM measurements. The mixing experiment contained the following molar ratios of Net-4 to laminin: 0.6 %, 1.2 %, 3 %, 6 %, 10 %, 25 %, 30 % and 50 % (Figure 11 B). For example at 100 %, all laminin proteins can possibly interact with one Net-4 protein. At least two independent gels for each Net-4 concentration were analyzed at three different positions generating three force maps per gel, respectively. Already at 0.6 % Net-4, a strong decrease of the Young's modulus from $\sim 476 \pm 66$ Pa to $\sim 387 \pm 59$ Pa was observed. The highest measurable concentration in this experiment was 50 % Net-4 with a Young's modulus of 170 ± 32 Pa. At higher Net 4 concentrations, adhesion between the matrigel and the AFM tip made indentation experiments impossible.

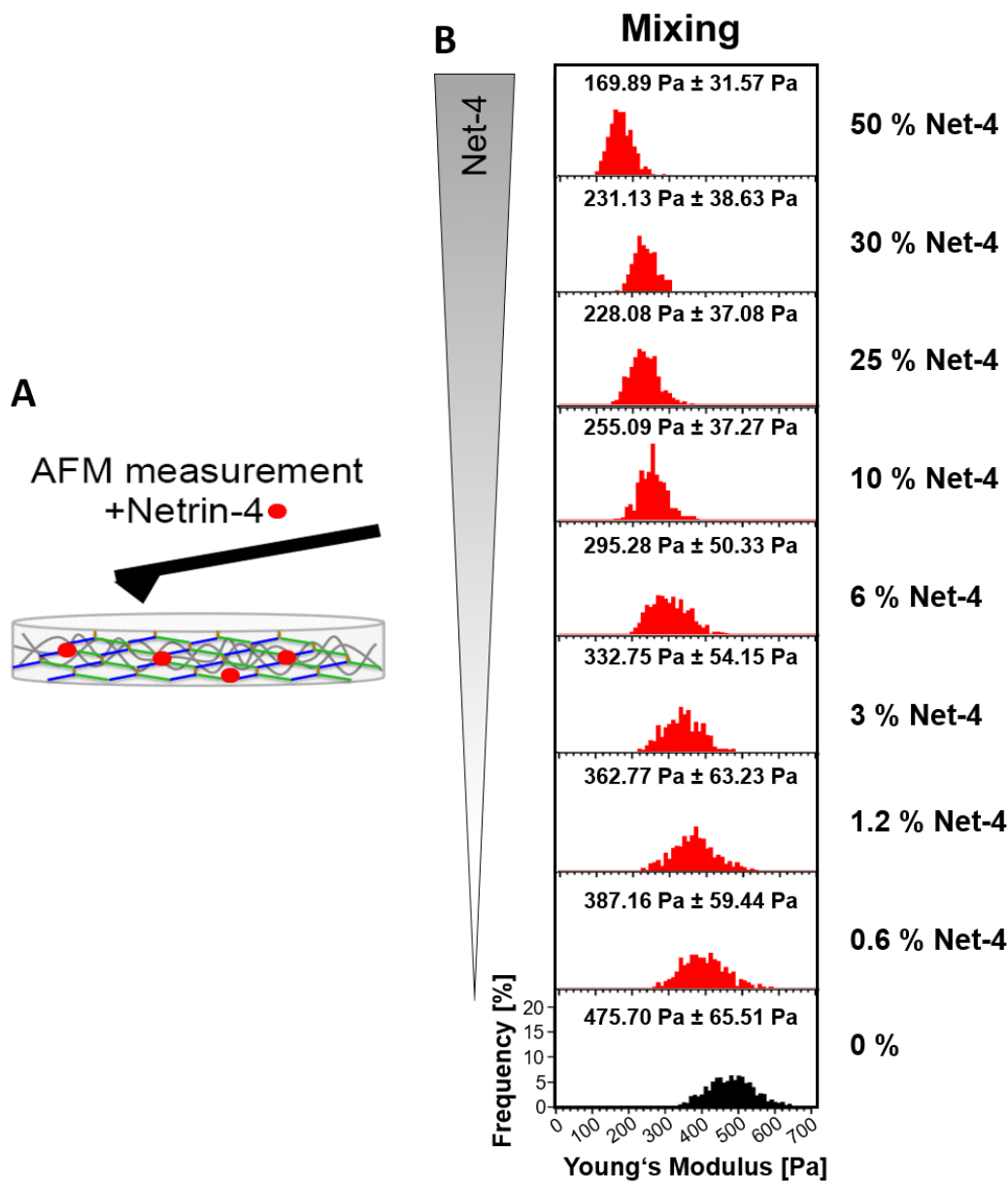


Figure 11: Histograms (of frequency in %) of Young's modulus values of the mixing experiment. A) Schematic overview of the experimental setup (taken from [49]). B) Histograms of pure matrigel (black bars) and with an increasing amount of Net-4 (red bars). A scan area of $100 \times 100 \mu\text{m}$ with 10×10 FD-curves was mapped with a maximal loading force of 2 nN and a constant vertical tip velocity of $5 \mu\text{m/s}$. At least two independent gels with three spatially separated maps were analyzed for pure matrigel and for each Net-4 concentration. For data analysis, the JPK software (version 6.0.69) was used, and the Young's modulus was derived from the first 500 nm of the indentation part of the curves using a modified Hertz model. (B submitted in [49]).

4.1.2 NET-4 DISRUPTS AN EXISTING LAMININ NETWORK

Next, the matrix-disrupting effect of Net-4 was investigated, using already polymerized matrigel. 2 ml cold matrigel were pipetted into a pre-cooled glass Petri dish. After 30 min at 37 °C, the gel was covered with 9 ml PBS and AFM indentation measurements were performed. First, the Young's modulus of the pure matrigel was examined. At least 3 force maps were recorded at different locations and an average Young's modulus of $\sim 419 \pm 38$ Pa was detected. For these experiments, a different batch of matrigel was used, which showed a slightly lower Young's modulus than the matrigel used for the mixing experiments ($\sim 476 \pm 66$ Pa) of pure matrigel. Because matrigel is an extract of the EHS tumor tissue, batch-to-batch variations in protein concentrations and the Young's modulus can occur. In these experiments, increasing amounts of Net-4 were added to the cured gel in a titration series, to detect a concentration-dependent decrease of the Young's modulus due to disruption of the matrigel. The titration series contained the following molecular ratios of Net-4 to laminin: 0.1 %, 0.5 %, 1 %, 2.5 %, 5 %, 10 %, 25 %, 50 % and 100% (Figure 12B). For each titration step, at least 3 force maps were recorded at different locations. By increasing the Net-4 amount, the Young's modulus of the matrigel decreased. Already after the addition of only 0.1 % Net-4 a clear decrease of the Young's modulus from ~ 419 Pa for pure matrigel to $\sim 376 \pm 34$ Pa could be observed. Over the entire titration series, a decrease of the Young's modulus from ~ 419 Pa for pure matrigel to ~ 57 Pa for 100 % Net-4, could be observed.

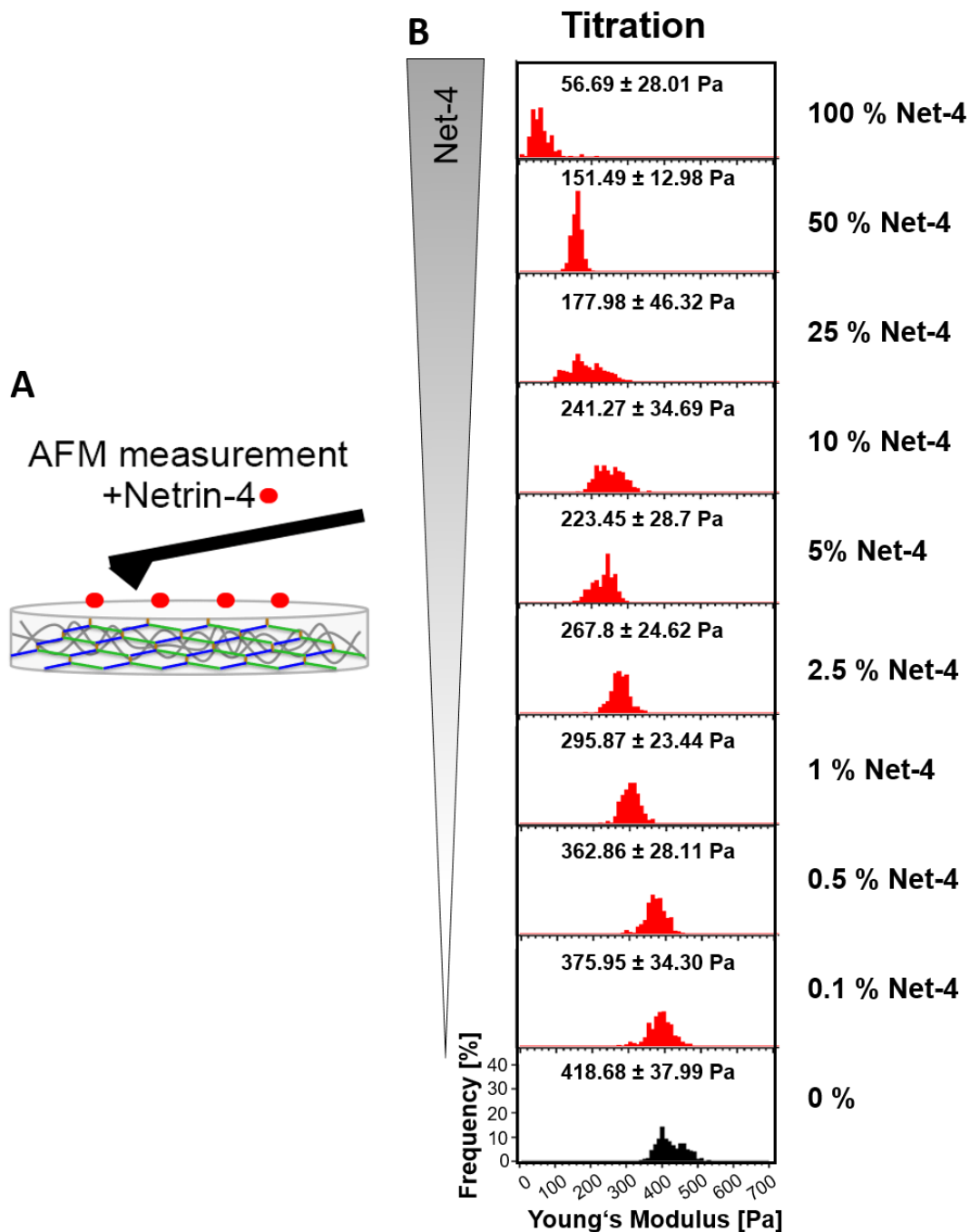


Figure 12: Histograms (of frequency in %) of Young's modulus values of the titration experiment. A) Schematic overview of the experimental setup (taken from [49]). B) Histograms of pure matrigel (black bars) and with an increasing amount of Net-4 (red bars). A scan area of $10 \times 10 \mu\text{m}$ with 10×10 FD-curves was mapped with a maximal loading force of 3 nN and a constant vertical tip velocity of $5 \mu\text{m/s}$. At least 3 maps were taken for each Net-4 concentration. For data analysis, the JPK software (Version 6.0.69) was used and the Young's modulus was derived from the first 500 nm of the indentation part of the curves using a modified Hertz model. (B submitted in [49]).

4.1.3 DISCUSSION AND CONCLUSION

It has already been shown, that the binding of Net-4 to the γ -chain arm of laminin regulates BM assembly and maintenance [51, 52]. In this thesis, AFM experiments identified Net-4 as a protein, also regulating BM mechanical properties in a dose-dependent manner. By mixing liquid matrigel with Net-4 prior to polymerization of the network, it could be shown that Net-4 is capable of preventing the formation of a new laminin network. The titration experiment in which Net-4 was gradually added to the pre-polymerized matrigel network revealed that the gel becomes softer with increasing Net-4 amounts. These findings support the assumption that the mechanical modulation of the BM arises from the competitive binding of Net-4 to the ternary node complex within the laminin network [49, 51]. In the case of the mixing experiment very small volumes of about 100 μ l of matrigel were used and the Net-4 was added directly into the gel. Here, the Net-4 was ubiquitously distributed and therefore could disrupt the gel at all positions equally. For the titration experiment, Net-4 was added to the buffer solution above the pre-polymerized matrigel. Therefore, the Net-4 - laminin interaction was limited to the gel surface, while an excess of Net-4 was still present in the buffer. This could be the reason why a 1:1 molecular ratio of Net-4 and laminin (referred as 100 % Net-4) could only be measured in the titration experiment. Nevertheless, in both experiments, a comparable decrease of the Young's modulus down to ~300 Pa in the mixing experiment and ~270 Pa in the titration experiment could be observed for 50 % Net-4. Moreover, even very small amounts of Net-4 (0.1 - 0.6%) in the titration and mixing experiment, respectively, already reduced the Young's modulus by more than 10 %.

Young's modulus variations in the BM play a crucial role in angiogenesis and are associated with metastasis formation. It has been shown that Net-4 overexpression inhibits angiogenesis and can reduce tumor progression [139–141]. Therefore, in the future Net-4 could be a potential candidate for cancer treatment [51].

4.2 THE ROLES OF ALPHA-ACTININ-1 AND -4 IN REGULATING THE ACTIN ARCHITECTURE AND YOUNG'S MODULUS

The actin architecture is governed by actin polymerization and by a variety of scaffolding and accessory proteins, like the non-muscle α -actinins-1 (A1) and -4 (A4). The influence of A1 and A4 on the structure and mechanics of the actin cytoskeleton has not yet been clarified entirely. In this thesis, the actin A1 and A4 double knock-out (A1/A4 KO) murine NIH3T3 fibroblasts and single knockins of A1 and A4 (A1/A4 KO +A1 and A1/A4 KO + A4, respectively) were investigated. The cell lines were generated by simultaneous multi-gene knockout using CRISPR/Cas9-mediated genome editing and kindly provided by A. Timper and C. Hauck (University of Konstanz) [83, 84] and were used as model system to investigate the effect of A1 and A4 on the architecture and organization of the actin cytoskeleton and on cell mechanics.

4.2.1 INFLUENCE OF THE SCAFFOLDING PROTEINS A1 AND A4 ON CELL MECHANICS

The mechanical properties of cells with alterations of the actin architecture induced by the depletion of the scaffolding proteins A1 and A4 were investigated in this section. AFM measurements were carried out using the QI mode, which simultaneously renders topography images (Figure 13 A and C) and Young's modulus maps (Figure 13 B and D) of single living cells. Cells were seeded on fibronectin-coated Petri dishes at low confluence so that they were situated as single cells for AFM measurements. Topography and Young's modulus data were extracted from FI-curves, as described in 3.2.

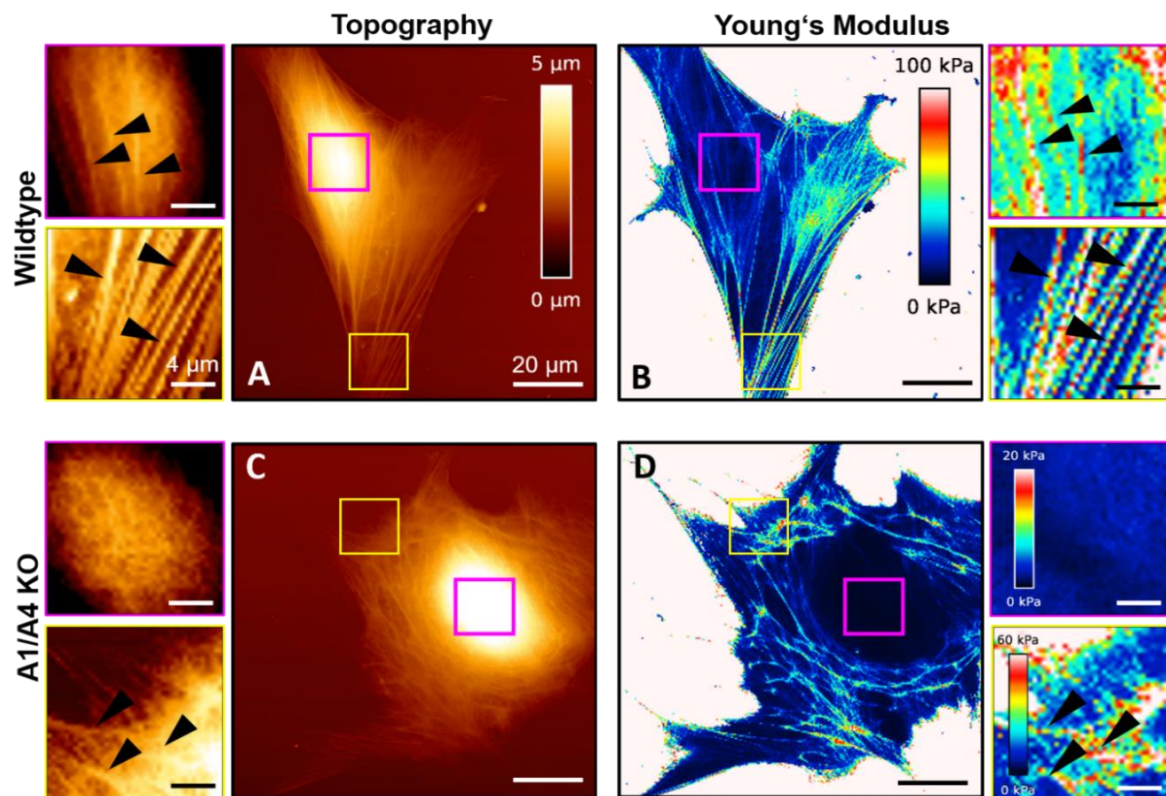


Figure 13: AFM topography images (A and C), and Young's modulus maps (B and D) of wildtype (WT) and A1/A4 KO cells. Yellow close-ups show the cell periphery and pink close-ups show the nuclear area. Black arrowheads highlight the cytoskeletal structures. A scan area of $100 \times 100 \mu\text{m}$ with 256×256 FD-curves, a maximal loading force of 1 nN and a vertical tip velocity of $300 \mu\text{m/s}$ was mapped. For data analysis, the JPK software (version 6.0.69) was used. Color bar for topography images: $0\text{-}5 \mu\text{m}$ and for the Young's modulus maps: $0\text{-}100 \text{ kPa}$ (overview), 20 kPa (pink close-ups) and 60 kPa (yellow close-ups).

Here, for the Young's modulus maps a threshold of 100 kPa was chosen to clearly separate the cell from the underlying substrate. The pink boxes in Figure 13 and Figure 14 show close-ups of the topography and the Young's modulus of the nuclear region. The yellow close-ups depict the periphery of the cells. For the close-ups of the Young's modulus maps, a threshold of 20 kPa for the highest part (Figure 13 B and Figure 14 B, pink close up) and 60 kPa for a lower part (yellow close up) were chosen, in order to highlight structures with different elastic properties in more detail. For wildtype (WT) cells, the topography images show a polarized cell shape with ordered prominent fibers (Figure 13 A). Overall, the density of the actin fibers decreases in the apical region of the WT cells, but prominent actin fibers can still be found over the entire cell. The yellow close up shows thick stress fibers at the cell edges and the pink close up shows more filigree fibers at the cell center, so-called perinuclear actin caps, spanning over the nucleus. These observations are also evident in the Young's modulus maps, where stiffer filamentous structures similar to the ones observed in the topography images are observed, as shown in Figure 13 B. In the topography images, A1/A4 KO cells show a round cell shape with a large cell body and many filopodia in all directions (Figure 13 C). In the apical area of the cell, mesh-like structures can be observed. Disordered and strongly cross-linked fibrous structures accumulate in a coronary ring around the cell center, at the lower regions of the cell. In the topography images, only the fibers observed in the lower regions of the cell correlate with stiff structures in the Young's modulus maps, as shown in Figure 13 D. However, the mesh-like structures in the apical region, which can be observed in the topography image, do not appear in the Young's modulus map.

To determine the specific effects of A1 and A4 on the structural organization of the actin cytoskeleton and the Young's modulus of the cells separately, partial knockin cells, expressing either A1 or A4, were investigated, as shown in Figure 14.

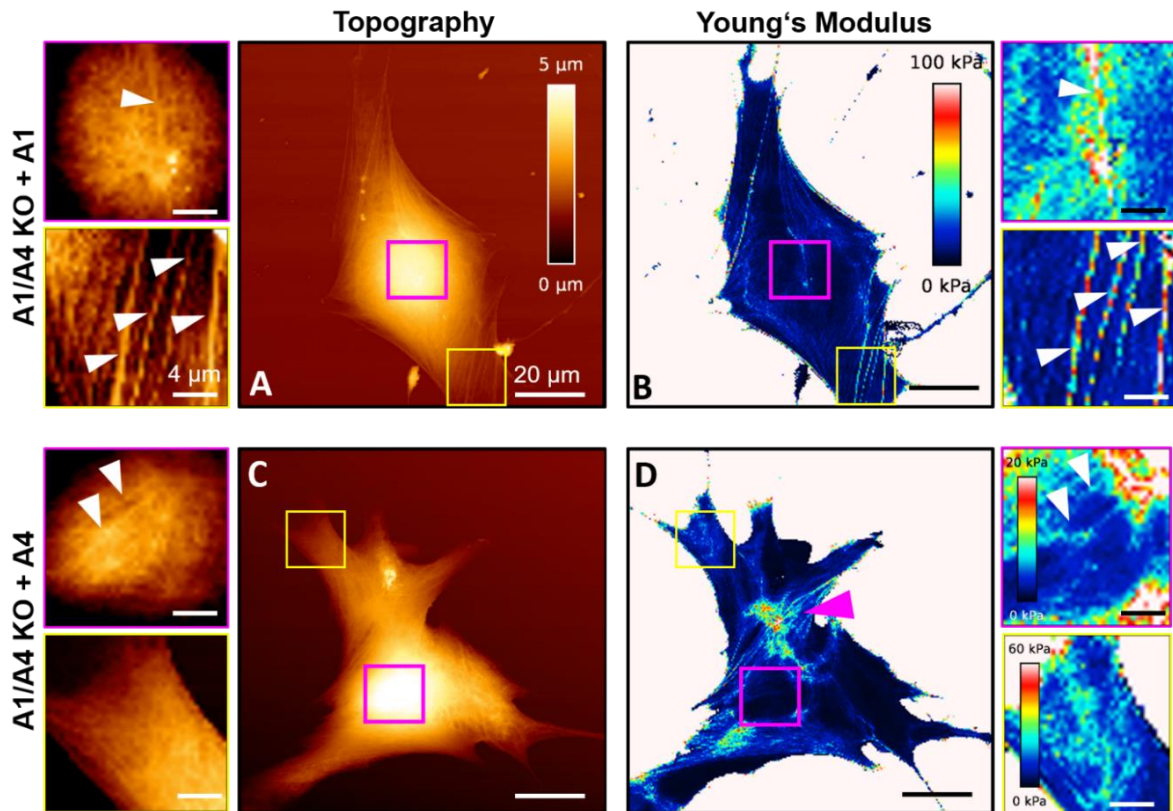


Figure 14: AFM topography images (A and C), and Young's modulus maps (B and D) of a partial A1 and A4 knockin: A1/A4 KO+A1 and A1/A4 KO+A4 cells, respectively. Yellow close-ups show the cell periphery and pink close-ups show the nuclear area. White arrowheads highlight the cytoskeletal structures, pink arrowhead highlights a cluster of cytoskeletal structures. A scan area of $100 \times 100 \mu\text{m}$ with 256×256 force curves, a maximal loading force of 1 nN and a vertical tip velocity of $300 \mu\text{m/s}$ was mapped. For data analysis, the JPK software (Version 6.0.69) was used. Color bar for topography images: 0-5 μm and for the Young's modulus maps: 0-100 kPa (overview), 20 kPa (pink close-ups) and 60 kPa (yellow close-ups).

The A1/A4 KO + A1 displays dominant fibrous structures mainly at the cell periphery and only very few and filigree fibers in the apical region of the cell, as shown in Figure 14 A (yellow and pink close-ups). These fibers, observed in the topography images, can be identified as stiffer structures in the Young's modulus maps (Figure 14 B). The overview and the close-ups of the Young's modulus map indicate a very soft cell body with only a few stiff but parallel aligned fibers. The A1/A4 KO + A4, on the other hand displays a cell shape resembling the A1/A4 KO cells, as shown in Figure 14 C and D. Here, at the apical region of the cell, only a few fibrous structures can be observed (Figure 14 C, pink close up). At the protrusion, no dominant fibrous structures can be observed (Figure 14 C, yellow close up). Both observations are consistent with the Young's modulus map, where a few stiff linear and partly branched structures can be observed in the close up of the apical region (Figure 14 D, pink close up), while at the cell protrusions a smooth distribution of the Young's modulus was detected (Figure 14 D, yellow close up). A noticeable feature of these cells are stiff structures appearing like tightly accumulated and branched filaments close to the nuclear region (Figure 14 D, pink arrowhead).

4.2.1.1 OVERALL YOUNG'S MODULUS AND CELL HEIGHT

In Figure 15 A and B, the overall Young's modulus and the maximum cell height are shown. Young's modulus values were extracted from all FI-curves of eight cells of WT and A1/A4 KO, respectively and five cells of A1/A4 KO + A1 and A1/A4 KO + A4, respectively.

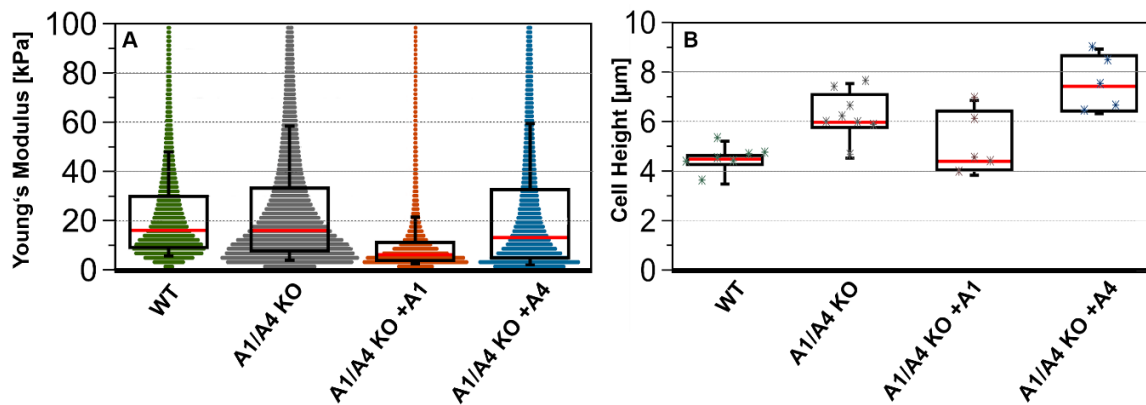


Figure 15: Young's modulus (A) and maximum cell height (B) of WT, A1/A4 KO, A1/A4 KO + A1 and A1/A4 KO + A4. The boxplots display the median (red line), the 25 to 75 percent quantile (black unfilled boxes) and 10 to 90 percent limits (whiskers). A) The colored waterfall plots display the frequency distributions of the measured Young's modulus values. B) The maximum cell heights for the individual cells are indicated by colored crosses. The maximum cell height was determined from the contact points at zero force from the FI-curves. (WT and A1/A4 KO, $n = 8$; A1/A4 KO + A1 and A1/A4 KO + A4 $n = 5$).

Surprisingly, the WT cells exhibit a Young's modulus median similar to the median of the A1/A4 KO cells with 16.2 kPa and 16.3 kPa, respectively (Figure 15 A). However, the maximum width of the waterfall plot, representing the most frequently measured values, appears at ~ 8 kPa and ~ 4 kPa for WT and A1/A4 KO cells, respectively. The A1/A4 KO + A4 cells also show a comparable median of the Young's modulus to the WT cells of 13.6 kPa while the maximum width of the waterfall plot lies at only ~ 2 kPa. The A1/A4 KO + A1 cells display a much lower median (6.2 kPa), than all other cells but also a maximum width of the waterfall plot at ~ 2 kPa. The maximum height of the WT cells has a median value of 4.49 μm (Figure 15 B). In the absence of both α -actinins, the cell height increases by ~ 1.5 μm to 5.98 μm for A1/A4 KO cells. The cell height of the A1/A4 KO + A1 reaches a median of the maximum cell height of 4.4 μm , resembling that of WT cells, while the A1/A4 KO + A4 exhibit the highest maximum cell heights of all cell types with a median of 7.42 μm .

4.2.1.2 YOUNG'S MODULUS OF BRANCHED VERSUS PARALLEL ACTIN FIBER ARRANGEMENT

In order to investigate the effect of branched and crossed versus linear and parallel actin fibers on the Young's modulus under wildtype conditions, meaning that both α actinins are normally expressed, WT cells were grown on micro-contact printed squared FN-spots with a diameter of 86 μm to inhibit cell polarization. AFM measurements were carried out using the QI mode and the Young's modulus maps are depicted in Figure 16.

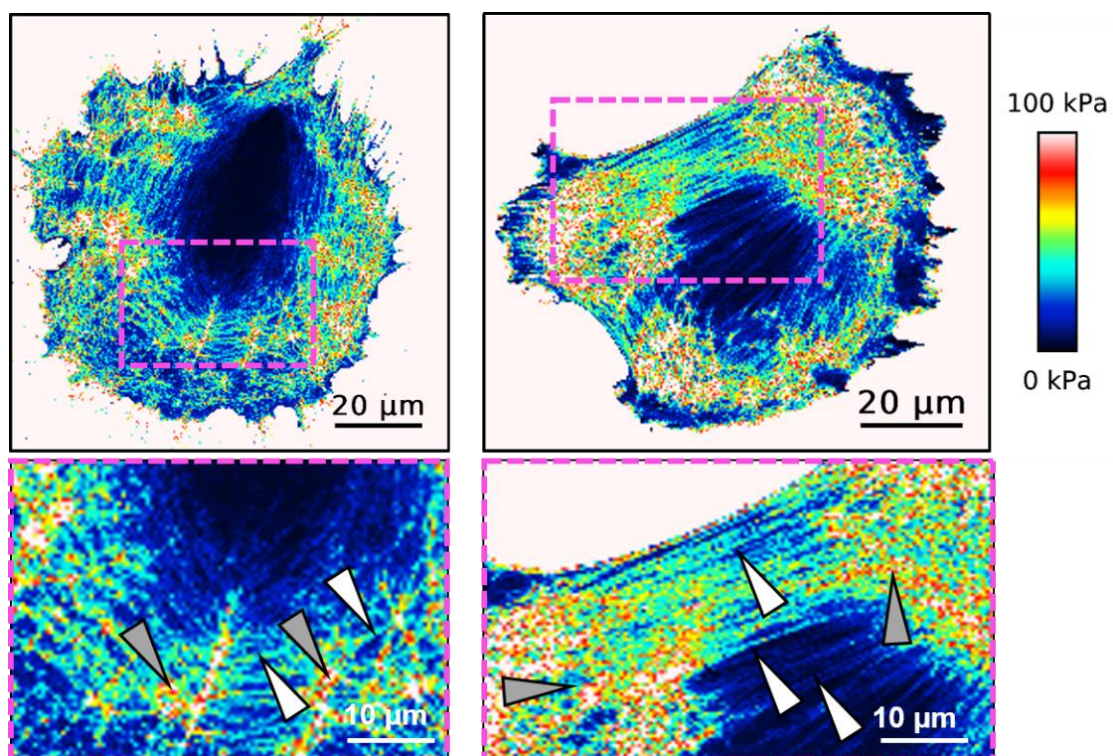


Figure 16: Young's modulus of branched versus linear actin fibers of WT cells. Cells were grown on microcontact printed FN-spots with a diameter of 86 μm to prevent cell polarization. Pink close-ups show the different actin architectures, grey arrowheads highlight branched actin and white arrowheads highlight linear actin fibers. A scan area of 100 x 100 μm with 256 x 256 FD-curves, a maximal loading force of 1 nN and a vertical tip velocity of 300 $\mu\text{m}/\text{s}$ was mapped. For data analysis, the JPK software (version 6.0.69) was used. Color bar for the Young's modulus maps: 0-100 kPa.

In contrast to unconfined WT cells, cell polarization and alignment of the actin fibers in one preferential direction cannot be observed anymore. Compared to the Young's modulus map of unconstrained WT cells, like the one shown in Figure 13 B, shows that the WT cells in Figure 16 exhibit stiffer structures over the entire cell because the actin cytoskeleton is now

separated in highly branched fibers, concentrated around the cell center and a few linear and parallel actin fibers, at the cell center and partly at the cell edges (Figure 16, right). Color-coding of the Young's modulus values (0 – 100 kPa) shows that branched actin exhibits a higher Young's modulus than the linear and parallel fibers. The highest Young's modulus values are observed at structures resembling nodes or strongly cross-linked actin, highlighted by grey arrowheads in the close-ups of Figure 16. Thus, the Young's modulus seems to increase with what seems to be increased actin cross-linking or branching. The linear actin fibers, exhibit a lower Young's modulus than the branched and accumulated actin fibers, as depicted in Figure 16 (white arrowheads) and in more detail in Figure 13 B. However, loosely packed parallel actin fibers at the cell center with a lower Young's modulus compared to densely packed parallel actin fibers at the cell edges suggests that an increased density of the fibers is also linked to an increase of the Young's modulus.

4.2.2 CORRELATION OF THE CELL HEIGHT AND THE YOUNG'S MODULUS

To correlate the Young's modulus to the cell height of individual cells, a cluster analysis was carried out where the Young's modulus values of WT and A1/A4 KO cells were plotted against the corresponding cell heights, as shown in Figure 17 and Figure 18.

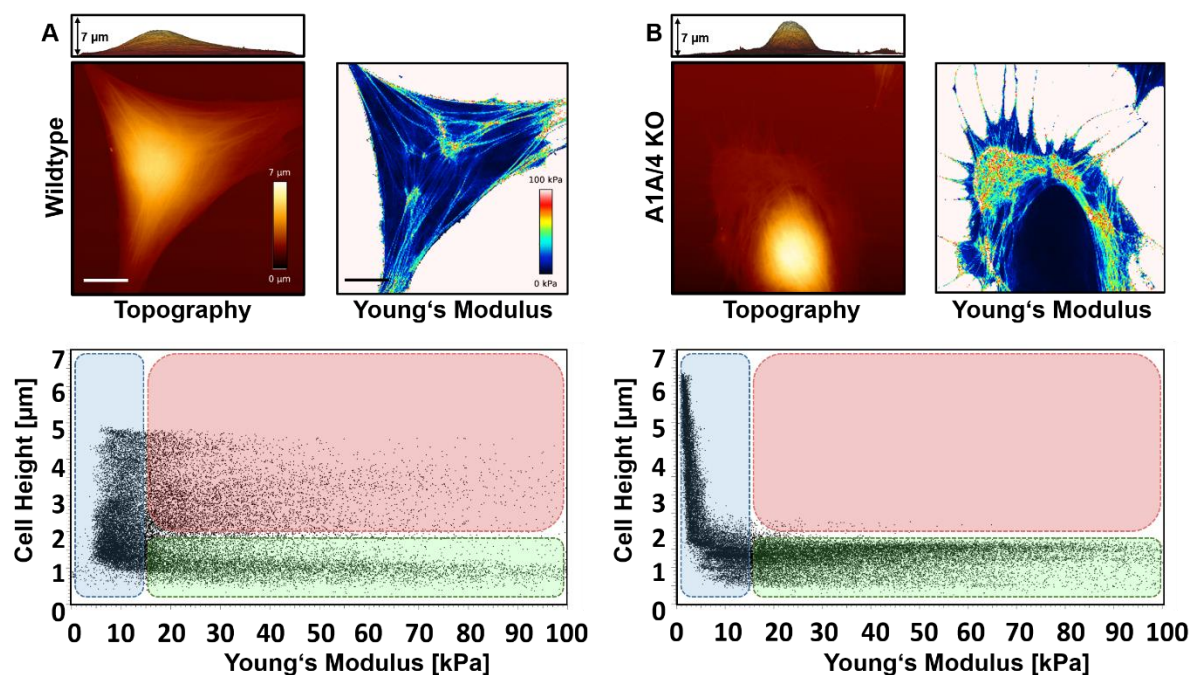


Figure 17: Correlation of the Young's modulus and the cell height of individual WT (A) and A1/A4 KO cells (B). An area of $100 \times 100 \mu\text{m}$ with 256×256 FD-curves, a maximal loading force of 1 nN and a vertical tip velocity of $300 \mu\text{m/s}$ was mapped. For the cluster analysis, the cell height and the Young's modulus of every curve is plotted in the diagram. The blue cluster highlights the intermediate to high and soft parts, the green cluster highlights the Young's modulus values of the flat parts of the cell and the red cluster highlights high Young's modulus values at the intermediate to high cell heights. Side view images were rendered from the topography images. Color bar for topography images: $0\text{-}7 \mu\text{m}$ and for the Young's modulus maps: $0\text{-}100 \text{ kPa}$. For data analysis, the JPK software (version 6.0.69) was used.

Again, the WT cells are compared to the A1/A4 KO cells. For the WT cells, Young's modulus values accumulate between $\sim 5 - 15 \text{ kPa}$ at cell heights from $\sim 1.5 \mu\text{m}$ up to the maximum of $5 \mu\text{m}$ (Figure 17 A, blue cluster). Within this area, the greatest accumulation of values appears between 1 and $2.5 \mu\text{m}$ cell height. From an intermediate height of $\sim 2 \mu\text{m}$ up to the maximum cell height, Young's modulus values of $\sim 18 \text{ kPa}$ up to 100 kPa are

observable, as depicted in Figure 17 A (red cluster). This observation is reflected in the topography and Young's modulus maps, where the WT cells show stiff structures at the highest part of the cell (Figure 13 A and B, Figure 17 A). At the lower regions between ~ 500 nm – $1,5$ μ m, Young's modulus values ranging from ~ 15 kPa up to 100 kPa can be observed (Figure 17 A, green cluster).

The most noticeable feature in the cluster analysis of the A1/A4 KO cells is that there are no longer values observable at high and at the same time stiff regions (Figure 17 B, red cluster). This is reflected in the topography and Young's modulus maps, where these cells show only soft and smooth structures at the higher parts of the cell above ~ 2 μ m (Figure 13 C and D, Figure 17 B). For the A1/A4 KO, there is a huge accumulation of data points from ~ 2 μ m up to the maximal cell height with low Young's modulus values in this area, ranging from ~ 2 - 6 kPa (Figure 17 B, blue cluster). In the lower parts of the cell, up to ~ 2.2 μ m, Young's modulus values reach up to 100 kPa (Figure 17 B, green cluster). Compared to the WT cells, the values within the green cluster seem to be shifted upwards. However, in the range of the red cluster of the WT cells (Figure 17 A), no data points are observed for the A1/A4 KO cells. Thus, the cluster analysis emphasizes the "fried egg" morphology of these cells, as shown in the side view images in Figure 17 B.

The correlation between the cell height and the Young's modulus was investigated for both actinins separately. A1/A4 KO + A1 cells exhibit an accumulation of low Young's modulus values at ~ 1 - 8 kPa (Figure 18 A, blue cluster). Very few Young's modulus values can be found at an intermediate cell height of ~ 3 μ m between ~ 10 – 60 kPa (Figure 18 A, red cluster) and at ~ 1 μ m cell height above ~ 10 kPa (Figure 18 A, green cluster). The A1/A4 KO + A4 cells, exhibit a minor accumulation of data points at low Young's modulus values between ~ 1 - 8 kPa for a cell height up to 7 μ m (Figure 18 B, blue cluster). At a cell height between ~ 3 – 6 μ m, Young's modulus values of ~ 10 kPa up to 100 kPa are apparent (Figure 18 B, red cluster). However, within this area, the height values are shifted downwards with increasing Young's modulus values. They also show an accumulation of values ranging from ~ 10 kPa up to 100 kPa at cell heights of ~ 1 - 2.5 μ m (Figure 18 B, green cluster). Similar to the A1/A4 KO cells the A1/A4 KO + A4 cells show a shift to higher regions (~ 2.5 μ m) within this cluster.

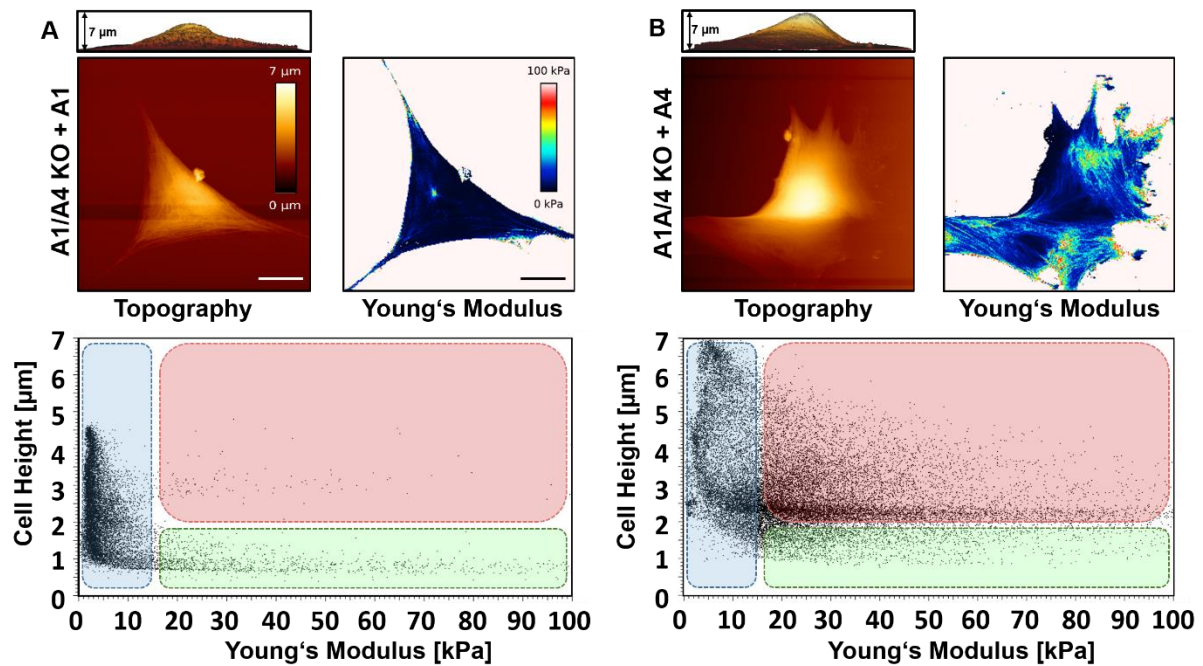


Figure 18: Correlation of the Young's modulus and the cell height of individual A1/A4 KO + A1 (A) and A1/A4 KO + A4 (B) cells. A scan area of $100 \times 100 \mu\text{m}$ with 256×256 FD-curves, a maximal loading force of 1 nN and a vertical tip velocity of $300 \mu\text{m/s}$ was mapped. For the cluster analysis, the cell height and the Young's modulus of every single FD-curve were plotted in the diagram. The blue cluster highlights the intermediate to high and soft parts, the green cluster highlights the Young's modulus values of the flat parts of the cell and the red cluster highlights the Young's modulus values of the intermediate to high cell heights. Side view images were rendered from the topography images and the total height was set to $7 \mu\text{m}$. Color bar for topography images: $0\text{-}7 \mu\text{m}$ and for the Young's modulus maps: $0\text{-}100 \text{ kPa}$. For data analysis, the JPK software (version 6.0.69) was used.

Most noticeably here was that the knockout of both α -actinins resulted in the total absence of the values within the red cluster. A1/A4 KO + A1 and A1/A4 KO + A4 show values within the red cluster again, even though the red cluster of the WT cells was not fully restored. The A1/A4 KO + A4 cells showed a clear accumulation of values within the red cluster whereas the A1/A4 KO + A1 cells exhibited only a few data points. Remarkable here is, that the data generated by this cluster analysis, confirmed the findings of the Young's modulus map (Figure 16 B), whereas the calculated overall Young's modulus, as shown in Figure 15 A, could not resolve these few but high and stiff structures in the A1/A4 KO + A1 cells.

4.2.3 BASAL AND DORSAL ACTIN ORGANIZATION

4.2.3.1 THE ROLES OF A1 AND A4 IN DORSAL AND BASAL ACTIN ARCHITECTURE

With the AFM, only the dorsal cell surface can be examined and therefore, only dorsal stress fibers can be detected. To validate the findings of the AFM measurements and to investigate the basal actin organization, z-stack images of the actin cytoskeleton were recorded using structured illumination fluorescence microscopy. For fluorescence microscopy, cells were seeded on fibronectin-coated Petri dishes, fixed and stained for the cell nucleus (blue) and the actin fibers (red). Z-stacks were recorded and orthogonal side view images were rendered from the image sequences, as shown in Figure 19 and Figure 20.

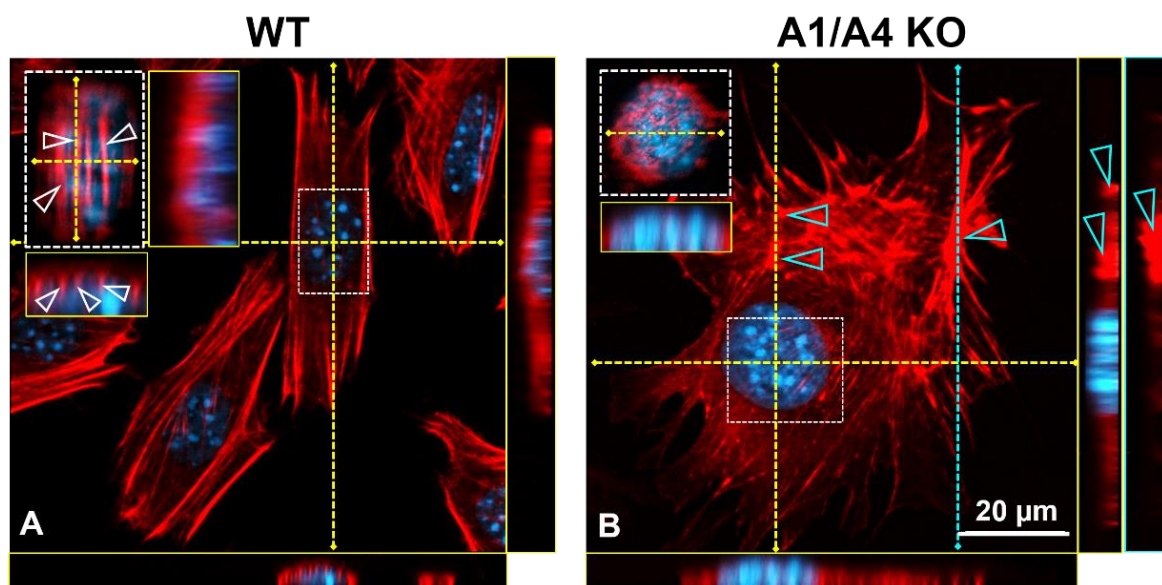


Figure 19: Z-stack fluorescence images of WT (A) and A1/A4 KO cells (B). 200 nm z-stack images were recorded using structured illumination fluorescence microscopy (Apotome 2, Zeiss). Fixed cells were stained with phalloidin-594 (actin, red) and DAPI (cell nucleus, blue). Overview images display the basal regions and the white dotted boxes display a close up of the apical regions. Yellow boxes show the side view images rendered from the z-stack image sequences and dotted lines mark the cross-sections. White arrowheads display the actin caps, blue arrowheads highlight actin clusters in the basal region and the side view images. Scale bar for basal actin and side view images: 20 μm .

WT cells exhibit a polarized cell shape with prominent cell body spanning as well as strictly aligned basal actin fibers with clear cell edges, as shown in Figure 19 A. The absence of both α -actinins, results in a strongly altered basal actin cytoskeleton, with unorganized actin fibers, often accumulated in cluster-like structures, multiple filopodia and thus no clear cell edges, as shown in Figure 19 B. Next, the dorsal actin was analyzed to confirm the AFM results and investigate the perinuclear actin caps. Figure 19 shows close-ups (white dotted close up) of the apical part of the cells and side view images (yellow cross-sections), to investigate actin caps. The WT cells exhibit dominant actin caps oriented in the direction of the longitudinal axis of the cell (Figure 19 A, white arrowheads). The side view images clearly display multiple actin bundles (Figure 19 A, transversal cross-section) and a pronounced dorsal actin cytoskeleton, spanning over the cell nucleus from one cell end to the other (Figure 19 A, longitudinal cross-section). In the apical region of the A1/A4 KO cells, only disrupted non-fibrous actin can be observed, as shown in Figure 19 B (white dotted close up). The side view images confirm the finding, that the A1/A4 KO cells lack actin caps because they do not show fibrous actin spanning over the cell nucleus (Figure 19 B, yellow cross-sections). However, noticeable here are extremely dense actin-clusters, as shown in Figure 19 B (blue arrowheads). Side view images show, that these clusters rise up to the intermediate cell height (Figure 19 B, blue cross-sections). These fluorescence images of the dorsal actin architecture of WT and A1/A4 KO cells confirm the AFM data.

The A1/A4 KO + A1 cells show a polarized cell shape with aligned actin fibers in the basal region (Figure 20 A), resembling the actin organization of the WT cells. The A1/A4 KO + A4 on the other hand exhibit an unorganized basal actin architecture (Figure 20 B), similar to the A1/A4 KO cells. Both A1-gfp and A4-gfp are associated with the basal actin fibers (Figure 20 C and D). However, A4-gfp accumulates more at actin clusters (Figure 20 D, blue arrowheads). The dorsal actin cytoskeleton of the A1/A4 KO + A1 displays loosely packed actin caps (Figure 20 A, white arrowheads). The side view images display actin fibers mainly at the basal and intermediate regions of the cell (Figure 20 A, yellow cross-sections). The A1/A4 KO + A4 cells display a dorsal actin architecture similar to the A1/A4 KO cells because they exhibit only disrupted actin at the apical region of the cell and also lack the actin caps spanning over the nucleus (Figure 20 B, white dotted close up). The side view images show that the actin fibers are shifted to the basal region of the cell and pronounced actin clusters, that rise up almost to the maximum cell height (Figure 20 B, blue arrowheads). The side view images of A1-gfp and A4-gfp reveal clear

differences. A1-gfp seems to be co-localized with the actin caps (Figure 20 C, yellow cross-section) whereas A4-gfp is mainly present at the basal region of the cells (Figure 20 D, yellow cross-section) and the actin clusters (Figure 20 D, blue arrowheads).

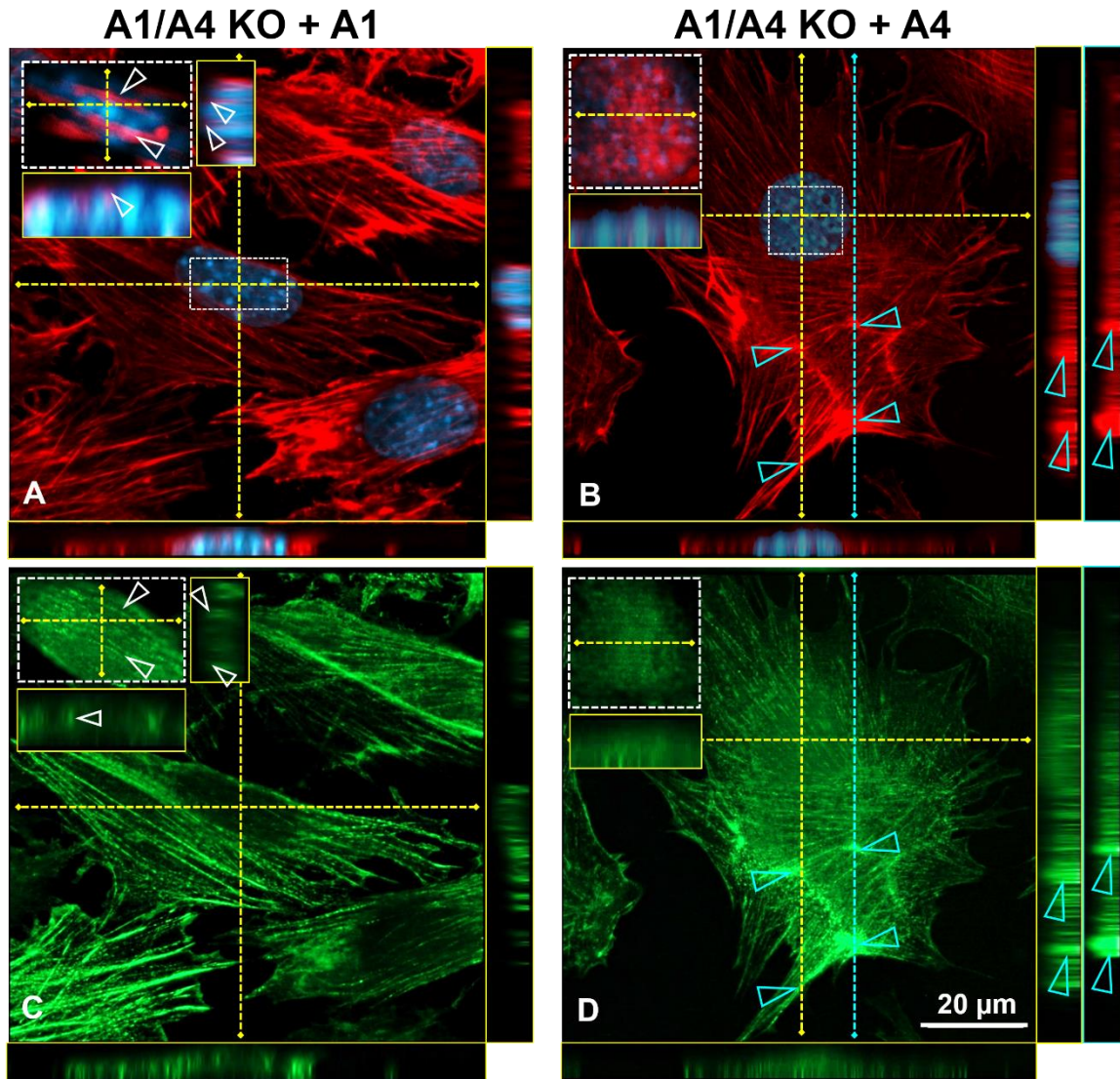


Figure 20: Z-stack fluorescence images of A1/A4 KO + A1 (A,C) and A1/A4 KO + A4 cells (B,D). Overview images display the basal regions and the white dotted boxes display a close up of the apical regions. Yellow boxes show the side view images rendered from the z-stack image sequences and dotted lines mark the cross-sections. White arrowheads display the actin caps, blue arrowheads highlight actin clusters in the basal region and the side view images. A and B) Fixed cells were stained with phalloidin-594 (actin, red) and DAPI (cell nucleus, blue). C) and D) display the gfp-tagged A1 and A4 (green, respectively). 200 nm z-stack images were taken using structured illumination fluorescence microscopy (Apotome 2, Zeiss). Scale bar for basal actin and side view images: 20 μm.

4.2.4 ACTIN ARCHITECTURE AND ADHESION SITES GUIDES CELL MIGRATION

4.2.4.1 CELL-CELL AND CELL-MATRIX CONTACTS AND THE ORIENTATION OF ACTIN FIBERS

External mechanical signals are transmitted into the cell via adhesion sites. Then, signals are further transmitted intracellularly via aligned actin fibers. The interplay of both is a prerequisite for the transmission of mechanical signals and thus for cellular processes such as migration. Because α -actinins play a crucial role in both: cell-cell and cell-matrix-contacts, the question how the absence of both α -actinins A1 and A4 affects the communication and sensing between neighboring cells and the matrix, is addressed in the following section. In this context, adherent junctions (AJ), focal adhesions (FAs) and the orientation of actin fibers were investigated next. For this, WT and A1/A4 KO cells were seeded on FN-coated coverslips for 24 h, fixed and stained for actin (red), the cell nucleus (blue) and cadherins, which is present in the AJs (green) or vinculin, which is present in the FAs (violet), as shown in Figure 21 and Figure 22, respectively. In addition, cell-cell contacts were analyzed by scanning electron microscopy (SEM) (Figure 21 B).

The WT cells exhibit matured cell-cell contacts, with characteristic cadherin localized at the contact sides, as shown in the fluorescence (green) and the SEM images (black arrowheads) (Figure 21 A and C). Contrary, the A1/A4 KO cells reveal neither prominent nor aligned cell-cell junctions, only little cadherin (green) is localized at cell-cell contacts (Figure 21 B). The SEM images confirm these findings, as no distinct cell-cell-contacts are observable (Figure 21 C).

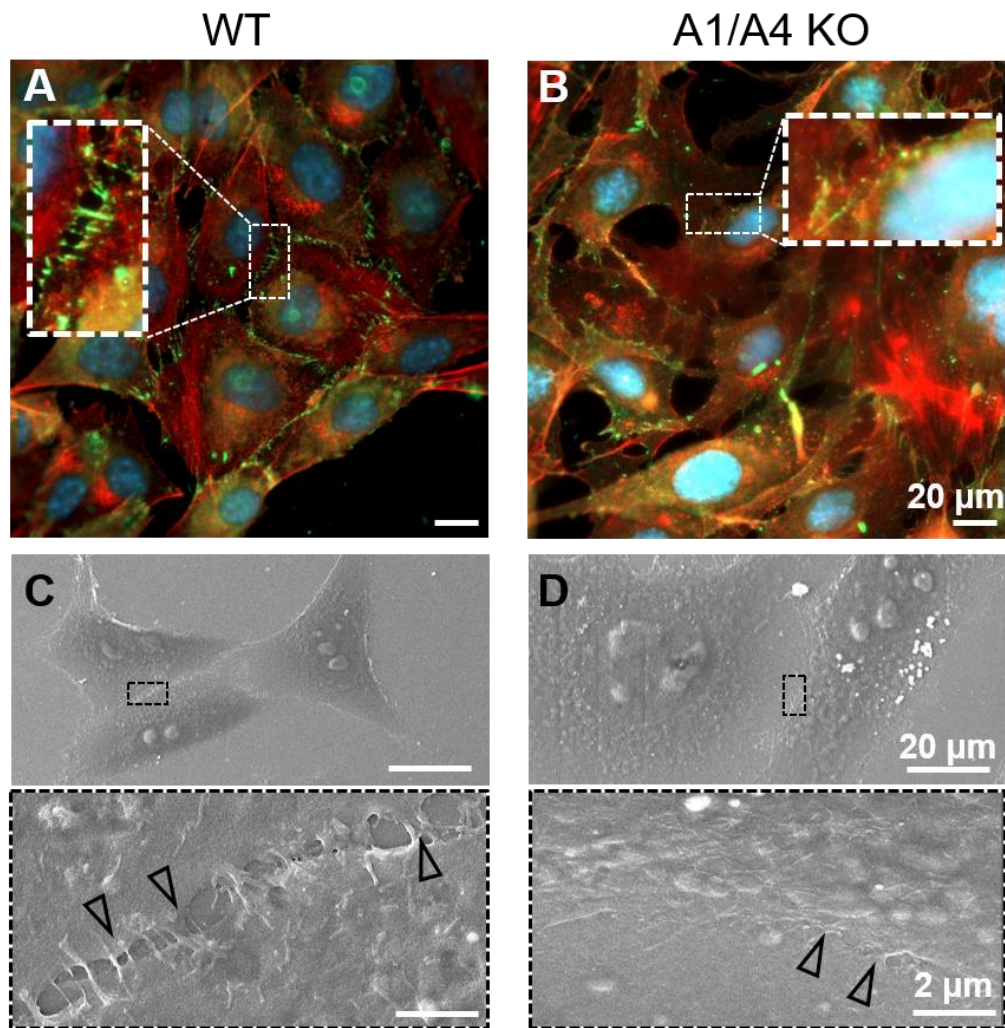


Figure 21: Cell-cell contacts of WT (A) and A1/A4 KO (B) cells. For fluorescence images (top row), cells were fixed and stained for cadherins (green), actin (red) and the cell nucleus (blue). SEM images show an overview of neighboring WT (C) and A1/A4 KO (D) cells. Black close-ups show the cell-cell contacts (highlighted by black arrowheads).

To investigate the effect of actinin-deficiency on how the cells sense their environment, cells were grown on micro-contact printed fibronectin-488 lines (20 μ m width), as shown in Figure 22.

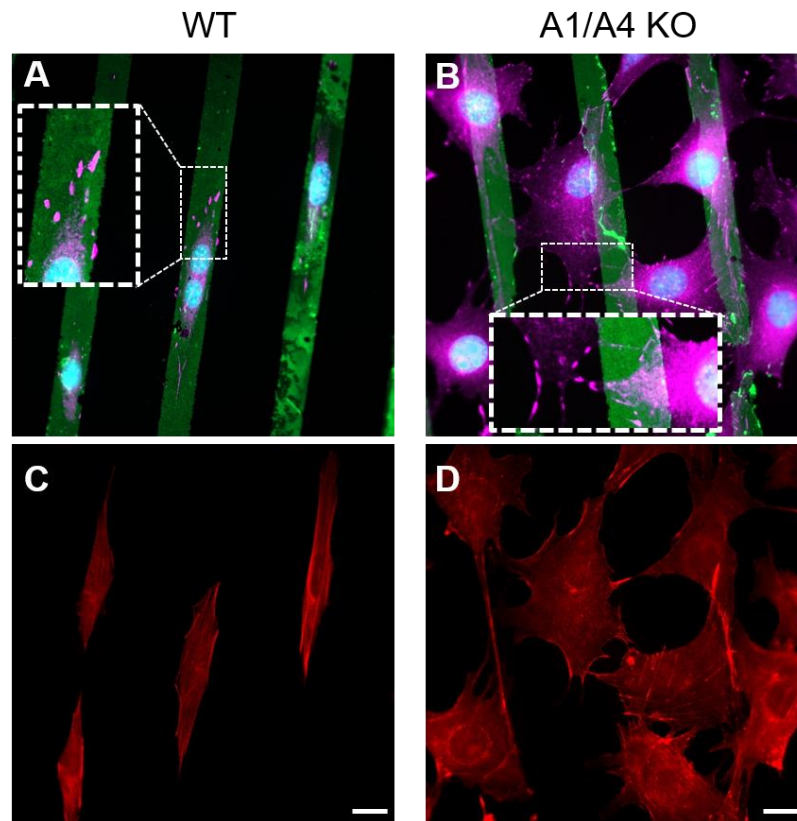


Figure 22: Focal adhesions of WT (A and C) and A1/A4 KO (B and D) cells, grown on micro-contact printed lines of Alexa-488-tagged fibronectin with a width of 20 μ m (green). For fluorescence images, cells were fixed and stained for vinculin (violet), actin (red) and the cell nucleus (blue). Close-ups show representative FAs of the WT (A) and the A1/A4 KO (B) cells. Scale bar: 20 μ m.

The WT cells strictly follow the given FN pattern. In this case, cell growth and spreading was restricted by the available 20 μ m FN lines. They exhibit a polarized actin architecture, aligned along the longitudinal axis of the FN pattern (Figure 22 C) and FAs are uniquely found on the FN patterns, as shown in the close-ups in Figure 22 A. Contrary, the A1/A4 KO cells exhibit a less organized cell growth. Even though parts of the cells grow on the FN-pattern, they do not strictly follow the printed FN pattern, as shown in Figure 22 B and C. They overgrow the FN-lines and exhibit FAs not exclusively on the FN, but also on the substrate between the lines, as shown in the close up of Figure 22 B.

Next, the orientation of the actin fibers and the intracellular tension were investigated. For the orientation of the actin fibers, WT and A1/A4 KO cells were seeded on FN-coated coverslips for 24 h, fixed and stained for actin (red) and DAPI (blue). Figure 23 A and B depicts the fluorescence images of actin and DAPI as a control and the color-coded orientation of the actin fibers, analyzed by using ImageJ (version 1.52d).

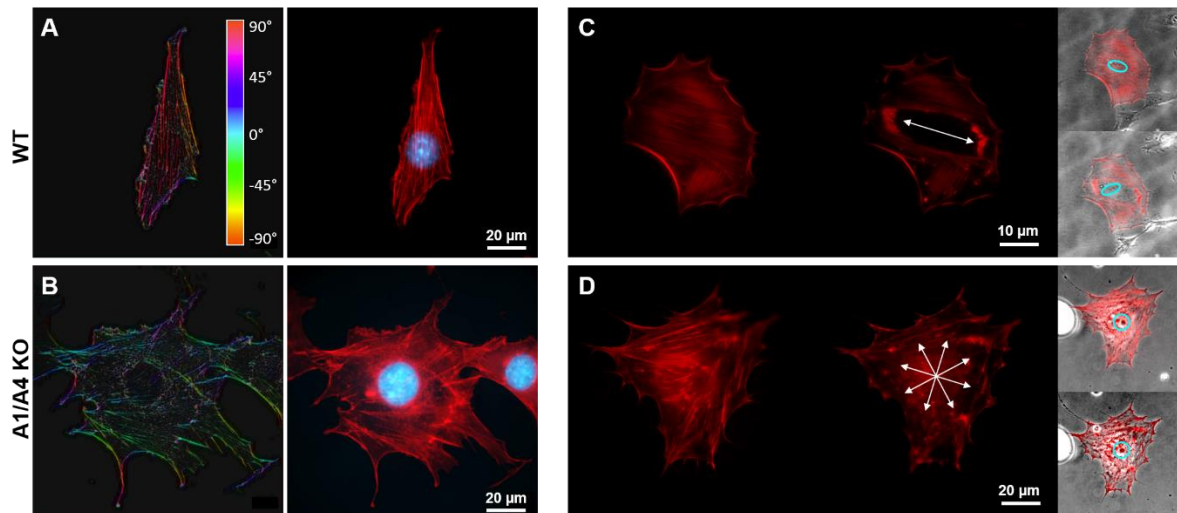


Figure 23: Orientation of actin fibers and direction of actin disruption after Lat. A treatment. A-B) Actin fiber orientation of WT (A) and A1/A4 KO (B) cells was determined using ImageJ. The color scale displays the different angles of the fibers. C-D) Lifeact-rfp expressing WT (C) and A1/A4 KO (D) cells before and after treatment with 1 μ M Lat. A for 15 min. Axis of depolymerization is marked by white arrows. Overlays of phase contrast and fluorescence images (right) display the shape and localization of the cell nucleus (blue circle).

For the WT cell, color-coding of the basal actin fiber orientation confirms the previous findings of an aligned orientation along the longitudinal axis of the cell (Figure 23 A). In contrast, the A1/A4 KO cells display long and bent stress fibers at the cell periphery and very short but linear fibers in the cell center (Figure 23 B). Here, the fibers appear in multiple colors, indicating different fiber orientations.

Figure 23 C and D depict the effect of the unorganized basal actin cytoskeleton in the A1/A4 KO cells. Lifeact-RFP expressing WT and A1/A4 KO cells were seeded on FN-coated coverslips for 24 h and were treated with the actin disrupting toxin latrunculin A (Lat. A). Lat. A binds monomeric actin and thus inhibits further polymerization. By destroying the actin cytoskeleton and recording the "tear-direction" of the actin fibers, the intracellular tension could be visualized indirectly. After treatment of the cells with Lat. A the basal actin

fibers in the WT cells rupture in the direction of the cell polarization axis (Figure 23 C, white arrows). The nuclear confinement is affected by this depolymerization of the actin fibers, as the nucleus clearly changes its orientation and position after Lat. A treatment (Figure 23 C, blue circles). Lat. A treatment in the A1/A4 KO cells leads to depolymerization of the actin network, starting from the cell center in multiple directions simultaneously (Figure 23 D, white arrows). Here, the nucleus position seems to be isolated from the basal actin cytoskeleton, because neither the shape nor the position of the cell nucleus changes after disruption of the actin cytoskeleton (Figure 23 D, blue circles).

4.2.5 UNORGANIZED ACTIN CYTOSKELETON HAMPERS COLLECTIVE CELL MIGRATION

To investigate the influence of the unorganized actin cytoskeleton and the stunted adhesion sites in A1/A4 KO on cell migration, cells were seeded with a high cell density in a drop on a FN-coated glass substrate, so that the cell front was able to colonize the free substrate, as shown in Figure 24.

WT cell migration originates from individual and fast-moving leader cells, followed by a collectively moving cell front. Overall, the WT cells exhibit a typical mesenchymal migration behavior due to an intermittent change from a round to an elongated cell shape, as shown in Figure 24 C (white arrowhead). The monolayer of the A1/A4 KO cells seems to lack intact cell-cell contacts because the A1/A4 KO cells behave like single players, rather than migrating collectively. The A1/A4 KO cells separate individually from the layer and maintain separated over the entire measurement period. During migration, the KO cells form protrusions in arbitrary directions, sometimes even simultaneously in different directions (Figure 24 D). Compared to the WT cells, the A1/A4 KO cells show no resting phases but constant movement, resulting in what seems to be a random walk, as shown in Figure 24 B and D. However, calculating the mean square displacement (MSD), the WT and A1/A4 KO cells exhibit both a slope of the MSD in a log-log plot of ~ 1.5 . Therefore, neither a random nor a persistence walk can be observed for WT and A1/A4 KO cells. The A1/A4 KO cells only exhibit an increased migration velocity, because they almost triple their velocity with $0.63 \mu\text{m}/\text{min}$ compared to the WT cells with $0.23 \mu\text{m}/\text{min}$ (Figure 24 E).

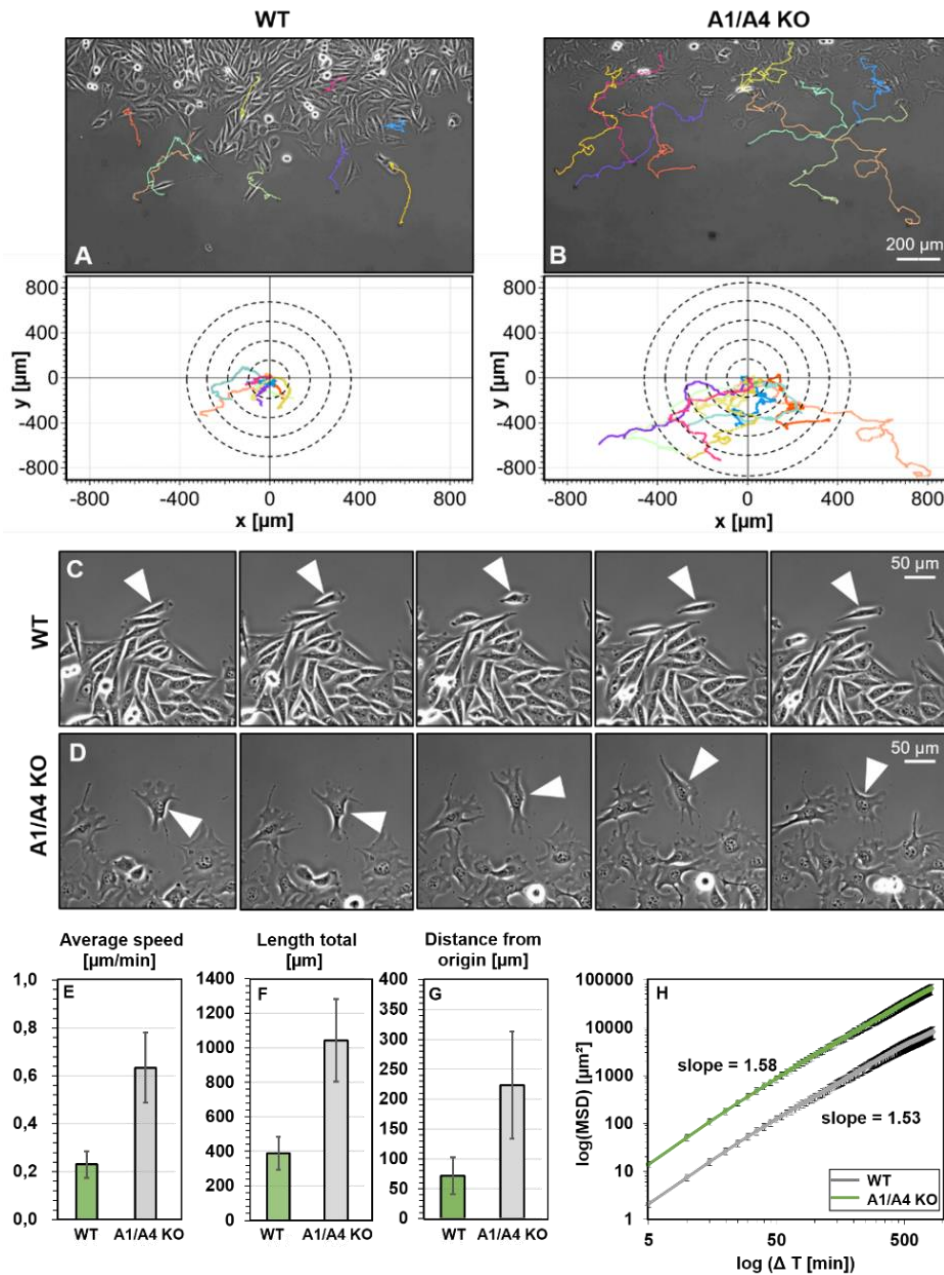


Figure 24: Influence of α -actinin depletion on cell migration of WT cells (A) and A1/A4 KO cells (B). Time-lapse microscopy was carried out with a time interval of 5 min for 27 h. 9 individual cells were tracked and the trajectories are displayed in different colors within the phase-contrast images (A and B, top) and in rose plots with the starting point shifted to the origin (A and B, bottom). C-D) Representative single-cell migration (white arrowhead) of a WT cell (C) and a A1/A4 KO cell (D) (10 min intervals), scale bar: 50 μm . E) Mean of the average cell migration velocity of the 9 tracked cells, calculated from (F) the total length of the trajectories. G) Mean of the distance from the origin of the 9 tracked cells. H) Mean square displacement (MSD) in a log-log-plot. The slope of the MSD for the WT cells is ~ 1.53 and for the A1/A4 KO cells ~ 1.58 .

Contractile actomyosin fibers are crucial for cell migration. Because α -actinins are involved in bundling contractile actin fibers, actomyosin fibers were investigated in the absence of both α -actinins. WT and A1/A4 KO cells were seeded on FN-coated coverslips for 24 h, fixed and stained for actin (blue) and myosin IIa (red) and fluorescence images were recorded, using two-photon excited fluorescence (TPEF) microscopy, as shown in Figure 25.

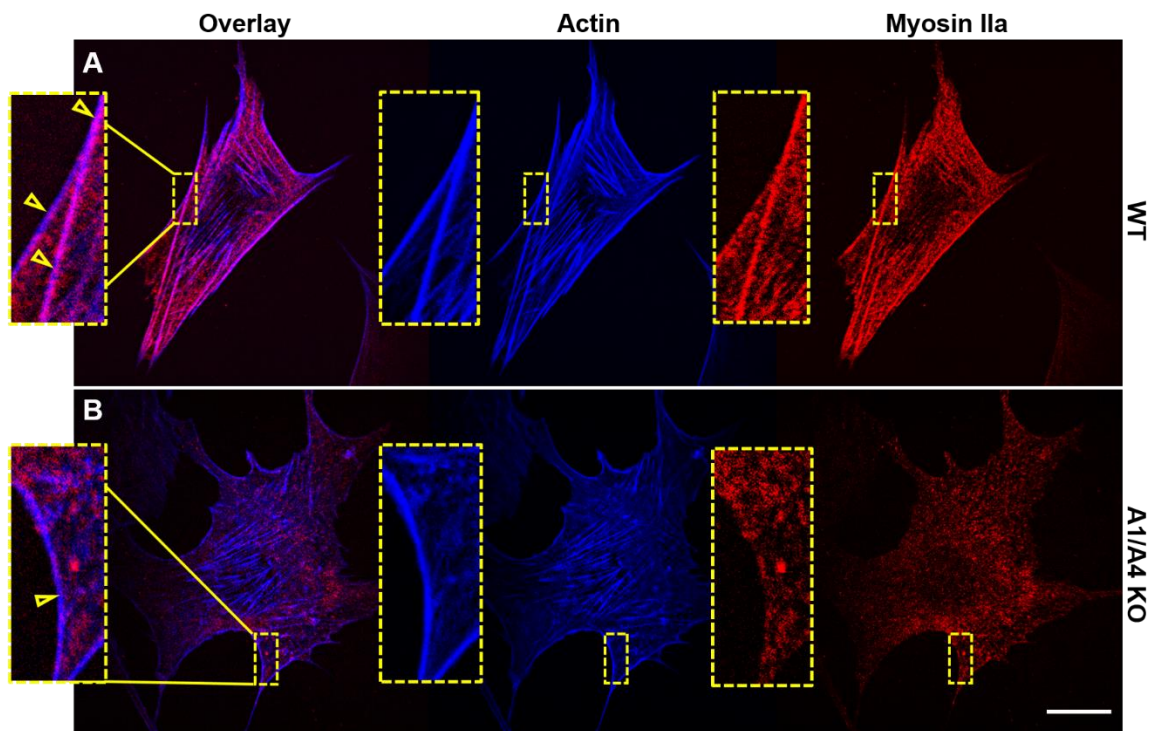


Figure 25: Fluorescence images of contractile actomyosin fibers of WT (A) and A1/A4 KO (B) cells using a custom-built two-photon excited fluorescence microscope. Cells were fixed and stained for actin (blue) and myosin IIa (red). Close-ups show representative contractile fibers. Scale bar 20 μm .

In the WT cells, the myosin IIa (Figure 25 A, red) is clearly localized along the actin fibers (blue), forming contractile fibers. These contractile fibers follow the longitudinal axis of the cell. In contrast, the A1/A4 KO cells, show no distinct co-localization of actin and myosin IIa in the contractile fibers (Figure 25 B). Prominent basal actin fibers are visible at the cell edges, but myosin IIa is localized in clusters, randomly distributed within the cell without clear co-localization with the actin fibers (Figure 25 B).

4.2.6 IMPAIRED TRANSLOCATION OF THE MECHANOSENSITIVE TRANSCRIPTION FACTOR MRTF

To investigate actin remodeling and therefore mechanosensitive processes, the translocation of the mechanosensitive myocardin-related transcription factor (MRTF) into the nucleus was used as a readout. MRTF binds to monomeric actin and is translocated to the cell nucleus upon actin-polymerization. A classical scratch assay was performed for WT and A1/A4 KO cells and the cells were fixed after 15 min, 30 min, 1 h and 4 h and stained for MRTF (green) as shown in Figure 26. As a reference, a confluent monolayer without a scratch was fixed and stained for MRTF, here referred to as 0 min. For the scratch assay, larger sections were recorded, to investigate, how far the cells communicate from the scratch into the cell field. Thus, the magnification of the fluorescence images shown in Figure 26 had to be reduced, compared to the previously shown fluorescence images.

In the intact monolayer (0 min), MRTF is preponderantly present in the cytoplasm for both, WT and A1/A4 KO cells. In the WT cells, all time points after applying the scratch (15 min - 4 h) show the same picture: a clear translocation of MRTF (green) into the cell nucleus, at the margin of the scratch and in the cell layer (Figure 26 A). Completely different results appear for the A1/A4 KO cells, as shown in Figure 26 B. After 15 min and 30 min, a translocation of MRTF into the nucleus can be observed for most of the cells (white arrowhead) but there is still cytoplasmic MRTF detectable (yellow arrowheads). After 60 min, the translocation decreases significantly. From this point on, only a few cells with MRTF in the nucleus are visible.

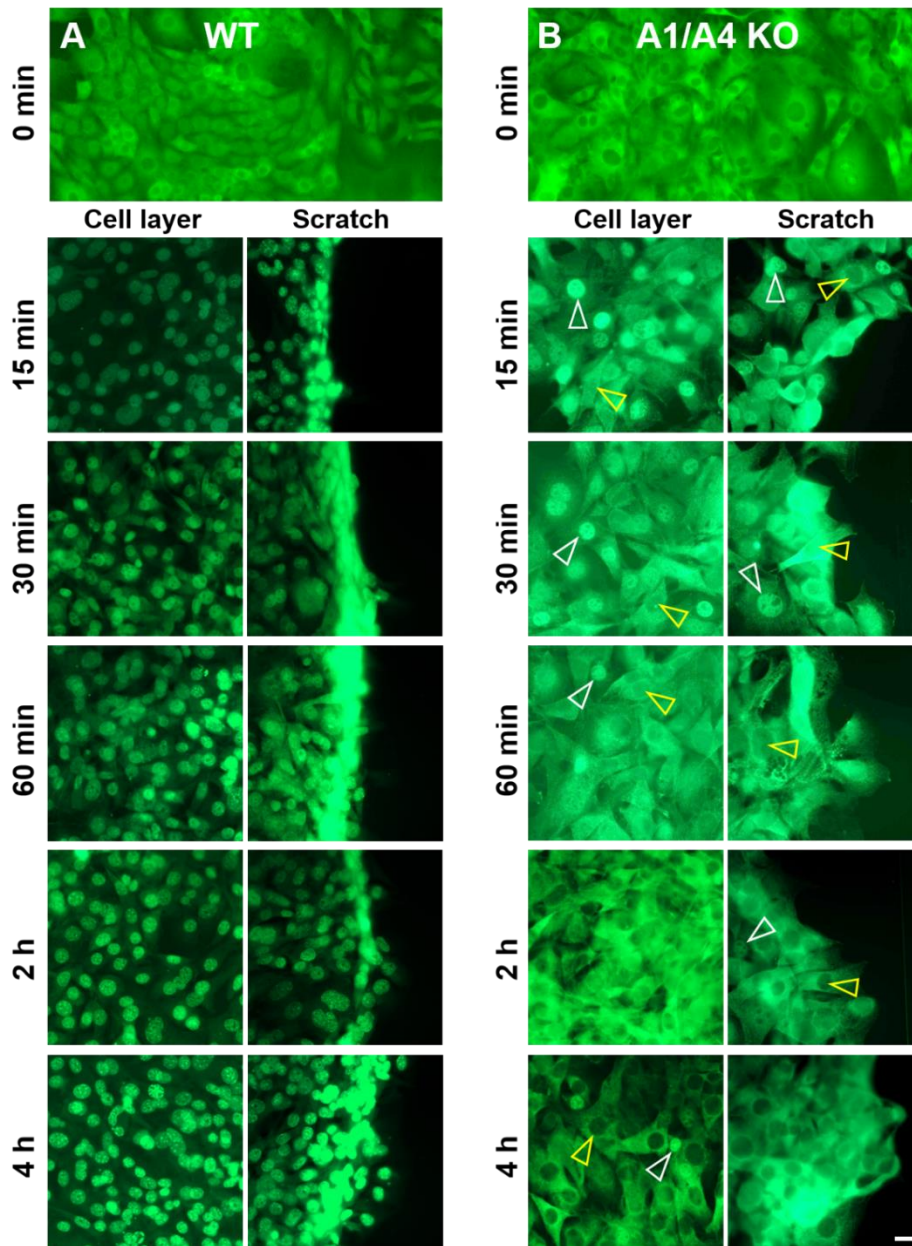


Figure 26: Translocation of the mechanosensitive transcription factor MRTF in WT (A) and A1/A4 KO (B) cells. A classical scratch assay was performed and cells were fixed at 15 min, 30 min, 60 min, 2 h and 4 h post scratch and stained for MRTF (green). Images of the cell layer were recorded about 1000 μm away from the scratch at the intact cell layer. As a control, a 100 % confluent cell layer of WT and A1/A4 KO cells was fixed and stained for MRTF without applying a scratch (0 min). Cytoplasmic MRTF indicates no actin turnover and thus no translocation to the nucleus, highlighted by yellow arrowheads, whereas white arrowheads mark the MRTF translocation to the nucleus. Scale bar: 20 μm .

4.2.7 DISCUSSION AND CONCLUSION

High-resolution AFM measurements enabled to resolve differences in biomechanics and morphology of WT, A1/A4 KO and the knockin cells A1/A4 KO + A1 and A1/A4 KO + A4 and therefore demonstrates the relationship between the structure of the actin cytoskeleton and the local elasticity. Interestingly, WT and A1/A4 KO and the partial A4 knockin cells exhibit a similar overall Young's modulus, whereas A1 expressing cells exhibit a significantly lower overall Young's modulus. However, looking at the spatial distribution of the Young's modulus values, clear differences are observable. While the WT cells show polarized and highly ordered parallel dorsal actin fibers, reflected by stiff structures in the Young's modulus maps, the A1/A4 KO and A1/A4 KO +A4 cells exhibit a strongly altered actin organization with a branched actin network and actin clusters in the cell body as well as the loss of actin caps, leading to very soft areas in the nuclear region, but also stiff areas in the cell body and the filopodia. Interestingly, even though A1 expressing cells could largely rescue the phenotype of the WT cells, the distribution of the Young's modulus shows only sparsely stiff structures.

The investigation of non-polarized WT cells on micro-contact printed circular FN-spot exhibited both: parallel aligned actin fibers and a highly branched actin network, demonstrating that an actin organization, consisting of parallel actin fibers, exhibits a lower Young's modulus in contrast to highly branched actin networks. Moreover, the Young's modulus increases with an increase of parallel actin fiber density. However, the higher Young's modulus might also originate from a higher actin content. The finding of the relationship between the actin fiber arrangement and the Young's modulus could explain the extremely low Young's modulus of A1/A4 KO + A1 cells, which show only very few linear actin fibers and no branched actin fibers in the AFM images. However, even these few dorsal actin fibers seem to be sufficient to rescue the cell height and cell shape. These cells exhibit perinuclear actin caps, which confine and compress the cell nucleus, resulting in a decreased cell height, similar to the WT cells. Hence, A1 and A4 seem to have different roles in organizing the dorsal actin cytoskeleton and tuning the mechanical properties of the cells. A1 seems to be involved in crosslinking the actin fibers and promoting cell polarization because orientated but loosely packed dorsal actin fibers can be observed in the A1 expressing cells. A4 on the other hand seems to promote actin clustering and branching

resulting in a stiff but disordered actin network in A4 expressing cells, which resemble the A1/A4 KO cells.

Actin disrupting drugs, such as Lat. A, which destabilize the actin cytoskeleton, often induce a cell morphology where the higher cell areas become increasingly soft [13, 142–145]. In addition, cellular processes influence the cell height and elasticity, because Harn et al. showed, that migrating cells are higher and softer than resting cells [142]. In 2009, Kasza et al. showed that filamin A (a protein with similar functions as α -actinins) deficient cells become higher and softer [13]. In healthy, untreated and resting cells there is no clear correlation between the cell height and the Young's modulus [143]. However, the information about the spatial distribution of the cell elasticity and, more important, how this correlates with cell height is missing in all these studies, because they did not acquire height and elasticity values at the same time or with sufficient resolution. In this thesis, the simultaneous measurement of the cell topography and the Young's modulus enables a cluster analysis by correlating these two values for each measurement point (see chapter 4.2.2). The WT cells exhibit an aligned dorsal actin cytoskeleton, in particular pronounced actin caps, leading to stiff structures over the entire cell height. The strongly altered actin cytoskeleton of the A1/A4 KO cells with its unaligned and highly branched actin fibers, divides the cell body into high and soft and flat and stiff areas. The cluster analysis confirms the finding that A1 and A4 have non-redundant roles in the actin architecture and thus the distribution of the Young's modulus. While the A1 expressing cells comprise Young's modulus values shifted towards a softer range, they exhibit a few rigid structures in the higher regions of the cell. Cluster analysis of A4 expressing cells reveals a scatter plot similar to the WT cells, but with the stiffer regions shifted towards lower cell height, comparable to the results for the A1/A4 KO cells.

α -actinins have recently been described as tension-buffer that can unfold force-dependently and thus regulate and ensure a force balance, necessary for mechano-driven processes such as migration [79]. Through the force-dependent unfolding, actinins can promote the binding of further scaffold proteins, such as vinculin at the adhesion sites. Furthermore, they can tune the elasticity of the actin fibers by their function as crosslinkers [79]. Due to the total depletion of both α -actinins in the A1/A4 KO cells, they lack an important regulator for cell elasticity and force generation. This could explain the fact, that A1/A4 KO cells show no typical mesenchymal cell migration behavior anymore. Instead, they display continuous

unsynchronized movement of different parts of the cell, as well as simultaneous formation of protrusions in various directions. Therefore, synchronized actin remodeling processes, that are required for regulated cell migration, are missing in these cells. Kasza et al. showed, that filamin A deficient cells generate lower contractile forces than the WT cells [13]. Indeed, the co-localization of actin-fibers and myosin IIa is hardly observable in the A1/A4 KO cells, suggesting a reduced contractility of actomyosin fibers. Because reduced contractile forces stimulate FA disassembly [67], this might explain the permanent movement of the cell body and thus actin remodeling during cell migration of A1/A4 KO cells. Disrupting the actin cytoskeleton using Lat. A shows the consequence of only short linear combined with branched basal actin fibers and therefore the undirected intracellular tension of the basal actin network in the A1/A4 KO cells. This probably makes it difficult for the cells to transmit forces across the entire cell in a coordinated way. This assumption is supported by the fact that the A1/A4 KO cells exhibit no cell polarization. In addition, probing the substratum or neighboring cells via adhesion sites and the transmission of external mechanical signals seem to be disturbed, because the cells exhibit only randomly distributed FAs and stunted cell-cell contacts, which hampers intact cell-cell-communication as shown by impaired translocation of MRTF and cell migration in a cell collective. The observation that A1/A4 KO cells not only exhibit an unorganized actin cytoskeleton but also randomly distributed adhesion sites and unsynchronized random migration behavior suggests that force is generated locally in a non-synchronized way and is not coordinated and transmitted throughout the cell in a synchronized way, as in WT cells.

In summary, it could be shown, that i) the actin cytoskeleton architecture is one determinant for the Young's modulus of the cells. ii) The overall Young's modulus gives no information about the spatial distribution of the Young's modulus within the cells. iii) A1 and A4 have non-redundant functions, regulating the actin architecture and thus the mechanical properties of the cells. iv) The synchronized transmission of intra- and intercellular forces and signals depends on the integrity of the actin cytoskeleton.

4.3 INFLUENCE OF CELL AGING ON ACTIN ARCHITECTURE AND CELL MECHANICS

How natural processes such as cell aging affect the mechanical properties of cells is discussed in the following chapter. In tendon stem progenitor cells (TSPCs), changes of the organization of the actin cytoskeleton during aging, as well as a rejuvenating effect of treatment with the ROCK-inhibitor (Y-27632) have been reported [27]. However, a study on the effect of these age-associated cytoskeletal rearrangements, as well as of Y-27632 treatment on cell mechanics is still missing. Here, the actin structure and the corresponding Young's modulus in young and aged TSPCs (Y- and A-TSPCs, respectively), as well as in Y-27632 treated A-TSPCs are investigated, using high-resolution AFM force maps. The results of the following chapter have been published in publication 1, listed in the list of publications and manuscripts.

4.3.1 YOUNG'S MODULUS: A BIOMARKER FOR CELL AGING

For AFM experiments, TSPCs were grown on collagen I coated Petri dishes at low confluence so that they were situated as single cells. Again, the QI mode was used for AFM measurements in order to simultaneously render topographic images (Figure 27, middle column) and Young's modulus maps (Figure 27, right column) at a sufficiently high spatial resolution, to distinguish individual actin fibers in Y- and A-TSPCs as well as in Y-27632 treated A-TSPCs cells.

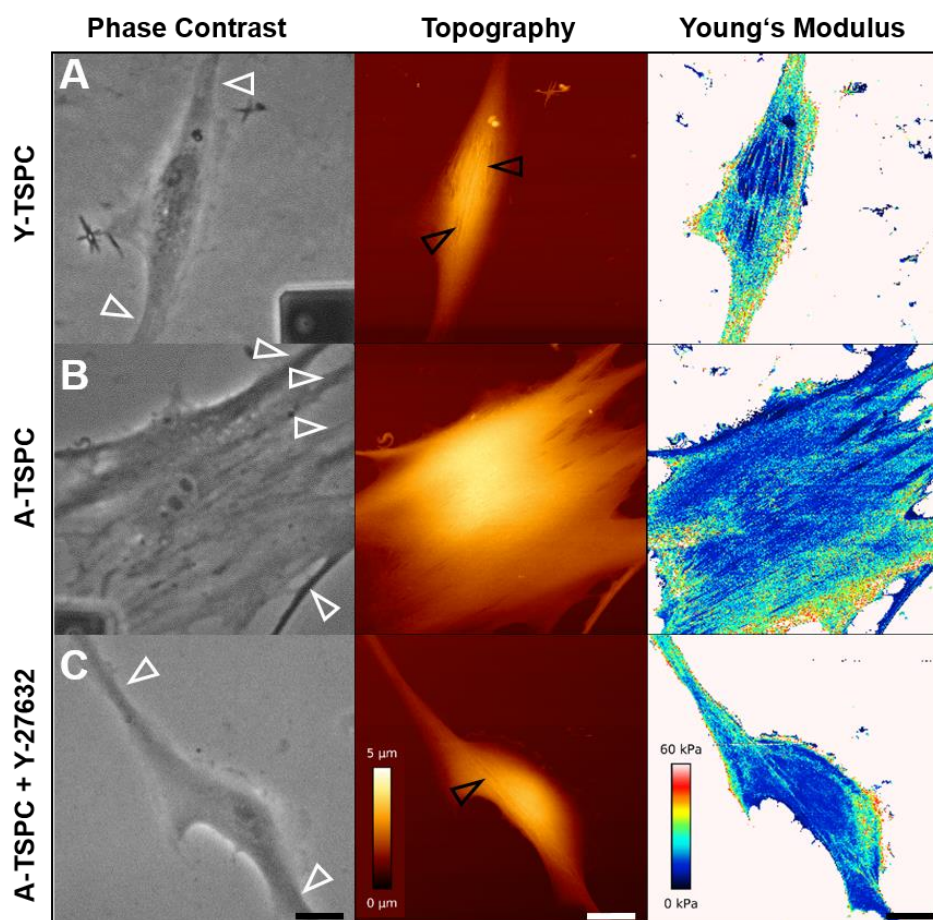


Figure 27: Phase contrast (left) and AFM topography images (middle), and Young's modulus maps (right) of A) a young (Y-TSPC) and B) an aged (A-TSPC) tendon stem/progenitor cell and C) a ROCK-inhibitor (Y-27632) treated A-TSPC. White arrowheads (left column) highlight the cell protrusions, black arrowheads (middle column) highlight topographic structures in the cytoskeleton. An area of $100 \times 100 \mu\text{m}$ with 256×256 force curves, a maximal loading force of 1 nN and a vertical tip velocity of $300 \mu\text{m/s}$ was mapped. For data analysis, the JPK software (version 6.0.69) was used. Color bar for topography images: $0\text{-}5 \mu\text{m}$ and for the Young's modulus maps: $0\text{-}60 \text{ kPa}$. Scale bar: $20 \mu\text{m}$. (Published in [26]).

For both, Y- and A-TSPCs, protrusions appear as the lowest parts of the cell, while the nuclear region was identified as the highest part of the cell in the topography images. Y-TSPCs exhibit fibrous structures (Figure 27 A), extending longitudinally through the cell, while A-TSPCs display a much smoother cell surface (Figure 27 A). The Young's modulus maps (Figure 27, right column) show stiffness variations in the range of 1 - 60 kPa within individual cells. Y-TSPCs exhibit soft regions at the elevated cell center, while high Young's modulus values are obtained at the flat cell edges and protrusions. The fiber-like structures observed in the topography image could clearly be identified as stiff fibers in the Young's modulus map. The elastic modulus maps of A-TSPCs display a higher Young's modulus at the cell periphery than observed for Y-TSPCs. At the same time, A-TSPCs exhibit a softer cell center than Y-TSPCs and the stiff fibrillary structures identified in the center of Y-TSPCs are not visible in A-TSPCs.

The distribution of the Young's modulus values obtained for Y- and A-TSPCs are displayed in a whisker boxplot combined with a waterfall plot in Figure 28 A. For Y-TSPCs (Figure 28 A, green), 50 % of all values are found between 7.8 kPa and 23.2 kPa, with the median at 13.8 kPa. The maximum width of the waterfall plot, which represents the most frequently measured Young's modulus, appears between 5 – 8 kPa. For A-TSPCs, the Young's modulus values are shifted towards higher values (Figure 28 A, yellow). The median of 19.5 kPa is almost 6 kPa higher, compared to Y-TSPCs and 50 % of all values are found between 12.4 kPa and 29.8 kPa. Furthermore, the frequencies indicated by the width of the waterfall-plot decreases almost linearly towards higher Young's modulus values. Thus, the data indicate an increased overall Young's modulus for A-TSPCs.

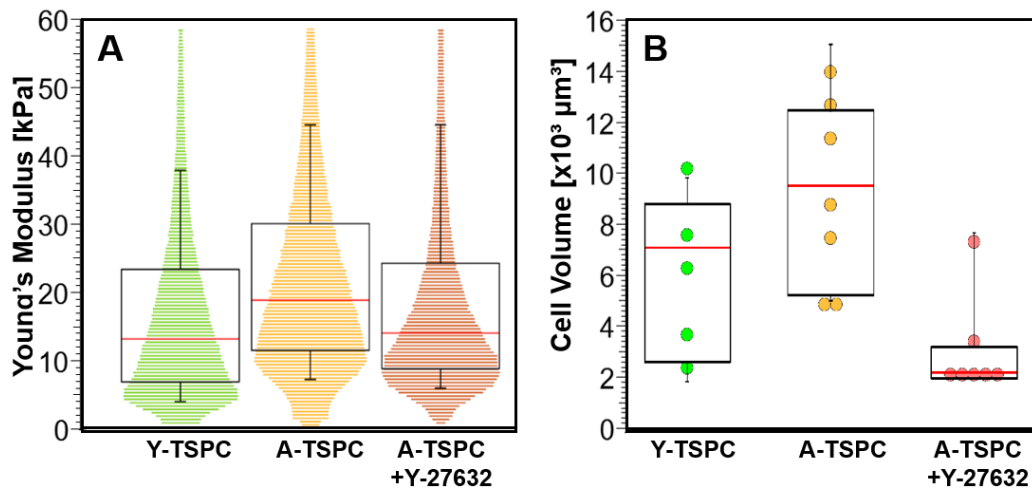


Figure 28: Comparison of A) the overall Young's modulus and B) the cell volume of Y-TSPCs (light green), A-TSPCs (yellow) and A-TSPCs+Y-27632 (red). Whisker boxplots display the 10 to 90 percent limits (black lines with end caps), the 25 to 75 percent quantile (black unfilled boxes) and the median (red line) of the Young's modulus. The distributions of the Young's modulus (colored scatter dot plots) show the accumulation of measured values. For data analysis, the JPK software (version 6.0.69) was used, and the Young's modulus was derived from the indentation part of the curves using a modified Hertz model. Seven individual cells ($n = 7$) of A-TSPCs and A-TSPCs + Y-27632 and five single cells ($n = 5$) of Y-TSPCs were investigated. (Published in [26]).

Another characteristic difference between Y-TSPCs and A-TSPCs is the cell volume, which was calculated from the AFM topography data. The median cell volume was $7307 \mu\text{m}^3$ for Y-TSPCs, whereas for A-TSPCs a median of $9559 \mu\text{m}^3$ was determined (Figure 28 B, green and yellow). However, some of the A-TSPCs exceeded the maximum scan area of the AFM of $100 \mu\text{m} \times 100 \mu\text{m}$, so the cell volume of these cells may be even larger, which would shift the median for A-TSPCs to even higher values.

4.3.2 CELL AGING PROMOTES A DENSE ACTIN ARCHITECTURE

Because AFM measurements clearly revealed differences in the Young's modulus, cell size and fiber-like structure between young and aged cells, age-related changes in the actin cytoskeleton were examined, using two-photon excited fluorescence (TPEF) z-stack microscopy. For these images, the actin cytoskeleton was stained with phalloidin-Atto594 (red) and the nucleus with DAPI (blue)

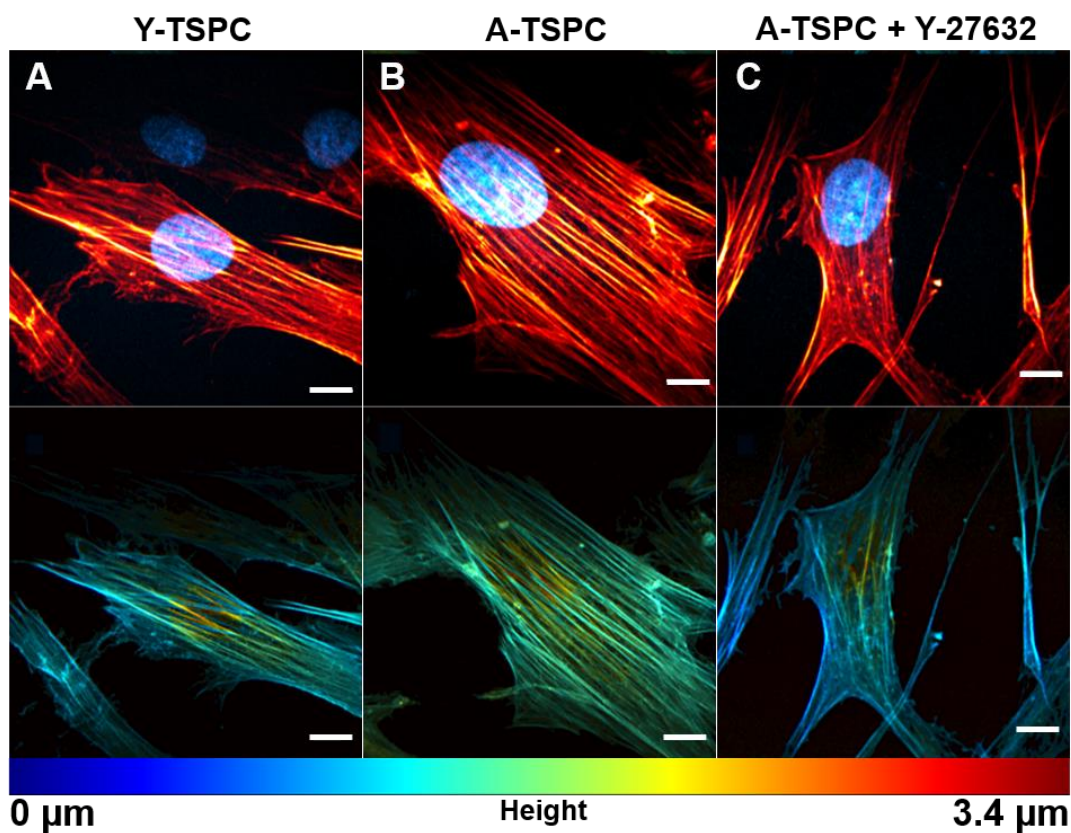


Figure 29: Actin cytoskeleton z-projection of the maximal intensity of each slice (top row) and z-projection with color-coded height (bottom row) using a custom-built, TPEF microscope for A) Y-TSPC, B) A-TSPC and C) A-TSPC+Y-27632. Cells were stained with phalloidin-Atto594 (red) and DAPI (blue). Z-projections with color-coded height of the actin cytoskeleton were generated from 200 nm z-stacks, color scale: 0-3.4 μm . Scale bar 10 μm . (Published in [26]).

Figure 29 shows the overlay of both fluorescence channels (Atto594 and DAPI) whereas the bottom row displays solely the actin cytoskeleton (Atto594). In order to distinguish basal (blue) and dorsal actin fibers i.e. actin caps (red), the z-stack projection is color-coded in height. The structure of the actin cytoskeleton differs for Y-TSPCs and A-TSPCs. Both are

traversed by actin fibers, whereby Y-TSPCs display a reduced fiber density compared to A-TSPCs. Only a few dominant fibers, which do not align strictly in parallel, span the longitudinal axis of the Y-TSPCs. Compared to the A-TSPCs, they show enlarged fiber-to-fiber distances, especially for the nucleus spanning stress fibers (Figure 29 A). This observation is in line with the AFM data, where few fibrillary structures appear in both, the topography images and the Young's modulus maps. In contrast to Y-TSPCs, A-TSPCs show a very dense network of actin fibers, traversing the cell in a strictly parallel orientation with equal distances (Figure 29 B).

4.3.3 ROCK INHIBITION: A SUITABLE REJUVENATING STRATEGY

To explore a rejuvenating effect by inhibiting the rho-associated kinases ROCK 1 and 2 with the ROCK-inhibitor Y-27632 on the cell topography, Young's modulus, cell volume and actin cytoskeleton architecture, Y-27632 treated A-TSPCs were also investigated. After treatment with the ROCK-inhibitor, A-TSPCs no longer exhibit a polygonal but a more spindle-like cell shape with only a few, but very long and thin protrusions (Figure 27 C), resembling the elongated shape of Y-TSPCs. The AFM topography images and Young's modulus maps display fibrillary structures, reminiscent of the structures observed in untreated Y-TSPCs (Figure 27 C). The overall Young's modulus of ROCK-inhibitor treated A-TSPCs decreases to a median of only 14.7 kPa (Figure 28 B A), which roughly corresponds to the median Young's modulus of Y-TSPCs. The non-linear decrease of the distribution of the Young's modulus values in the waterfall-plot resembles the curve of Y-TSPCs as well. The cell volume of ROCK-inhibitor treated A-TSPCs decreases to only 2755 μm^3 (Figure 28 B) and thus even below the volume of 7307 μm^3 that was observed for Y-TSPCs. Moreover, Y-27632 treatment of A-TSPCs had a dramatic effect on the structure of the actin cytoskeleton (Figure 29 C). A mixture of thick and very filigree actin fibers still spans the cell along the longitudinal axis, but the strictly parallel fiber arrangement present in untreated A-TSPCs is distorted. The cell shape and Young's modulus of A-TSPCs treated with ROCK inhibitors resemble those of Y-TSPCs and thus confirm a rejuvenating effect of Y-27632 treatment.

4.3.4 DISCUSSION AND CONCLUSION

In this section, the influence of cell aging on the biomechanical properties of tendon stem/progenitor cells (TSPCs) was investigated. In addition, it was demonstrated that by treatment with a ROCK-inhibitor, aged TSPC cells could be rejuvenated to younger cell characteristics such as cell morphology and the Young's modulus.

Functional distortion of tendon stem/progenitor cells (TSPC) has been closely linked to tendon pathologies and degeneration [104, 146–148]. Tendon degeneration and subsequent injuries increase in elderly patients, while their repair capacity declines, indicating that TSPC function is affected by aging [101, 102, 148]. Elucidating the molecular and cellular processes of TSPC aging, Kohler et al. observed significant changes in the expression of genes involved in cell adhesion, migration and the dynamics of the actin cytoskeleton. These findings strongly suggest that alterations in the actin organization play a major role in cell aging, which implies that the mechanical properties of TSPCs change with aging, as well. To answer the question, how the mechanical properties of TSPCs are affected by these age-related changes in the actin cytoskeleton, topography images and Young's modulus maps were recorded from individual TSPCs of young and aged donors.

As expected, based on the reported changes in the actin cytoskeleton, a significant increase of the Young's modulus and cell volume of TSPCs isolated from aged donors was observed. In particular, the low Young's modulus values, which were mainly found in the elevated cell center of Y-TSPCs, were diminished in A-TSPCs. A-TSPCs exhibit a smooth surface topography without prominent fibers. The homogeneous distribution of the Young's modulus over the cell indicates a more homogenous and densely packed actin network in A-TSPCs. Contrary to A-TSPCs, Y-TSPCs exhibited both, soft areas with a relatively large inter-fiber distances, as well as stiffer cell parts with a densely packed fiber arrangement. TPEF microscopy confirmed these differences in actin network organization for both cell types and corroborated the hypothesis that the altered organization of the actin cytoskeleton in aged TSPCs, which is also reflected in a higher actin content and a lower actin turnover [27], is responsible for the age-related increase of the Young's modulus in TSPCs. A similar observation was made for the α -actinin KO cell system: Actin fibers and especially crosslinking and branching increase the Young's modulus of the cells.

Aging effects on human mesenchymal stem cells (hMSCs) of young and elderly donors have been extensively investigated on the molecular level [149–151]. Also, the relationship between increased elastic modulus and aging has been shown for various cell types, including epithelial cells [14], cardiac myocytes [15] and fibroblasts [16,17]. For MSCs, an increase of the elastic modulus has been observed during long-term *in vitro* culture [152]. Also, an age-related increase of viscoelastic properties of TSPC monolayers, isolated from elderly vs. young rats, was investigated [153]. Nevertheless, alterations in biomechanical properties from young to elderly individuals have not been reported to date for hMSCs and especially for human TSPCs. Related to these studies, in this thesis, the Young's modulus could be confirmed to be a suitable marker to discriminate between Y-TSPCs from A-TSPCs. Moreover, rejuvenating A-TSPCs with Y-27632 back to Y-TSPC characteristics turned out to be a promising approach, as it reversed the age-related changes, such as Young's modulus and cell size in TSPCs.

Taken together, in this section age-associated changes of the structure of the actin cytoskeleton could be shown. For TSPCs, cell aging results in a higher density or parallel and highly aligned actin fibers in combination with an increased Young's modulus. Thus, it could be shown that the Young's modulus serves as a suitable biomarker for aging. This marker might be useful to select fully functional TSPCs from patient samples for cell-based therapies and tissue engineering applications. Furthermore, due to the rejuvenation effect on aged TSPCs, ROCK 1 and 2 could be used as potential targets for therapeutic applications, such as the treatment of tendon injuries with functionally rejuvenated cells with potentially increased healing capacity.

4.4 YOUNG'S MODULUS OF Y- TSPC AND A-TSPC LADEN HYDROGELS

In the previous chapter, clear differences between the Young's moduli of Y- and A-TSPC could be shown under 2D cell culture conditions. However, it is known that cells behave differently in a 3D environment because the interplay between cells and their surrounding matrix plays an important role in cellular behavior and ECM remodeling [107]. For the TSPCs, used in this thesis, D. Docheva's group (Universitätsklinikum Regensburg) showed that the micro-architecture of the environment guides cell behavior and has a positive effect on cell proliferation and cell rejuvenation [114]. They used a well-defined hydrogel, containing the self-assembling peptide RADA. RADA peptides consist of the amino acids arginine, alanine and aspartic acid [114, 115]. Thus, RADA peptides undergo spontaneous assembly, generating a fibrous hydrogel with a pore size between 5-200 nm and a water content of ~99 %. This constitutes a microenvironment, similar to natural ECM architecture [38–40]. Therefore, RADA 3D hydrogels have been applied to multiple cell systems already [116, 117]. The results of the following chapter are based on publication 2 listed in list of publications and manuscripts.

4.4.1 INCREASED YOUNG'S MODULUS OF CELL-LADEN HYDROGELS WITH A BIMODAL DISTRIBUTION

To determine the Young's modulus of the pure and the cell-laden 3D RADA hydrogels, Y- and A-TSPCs were cultured for seven days in the 3D gel system by D. Docheva's group. For AFM-measurements, the gels were embedded in TissueTek and 100 μm thick cryosections were prepared. Subsequently, the sections were stained with Hoechst nuclear staining to confirm the presence of the cells in the RADA gel. Indentation measurements on these sections, with the AFM mounted on an optical inverted microscope, were carried out in PBS at RT as shown in Figure 30.

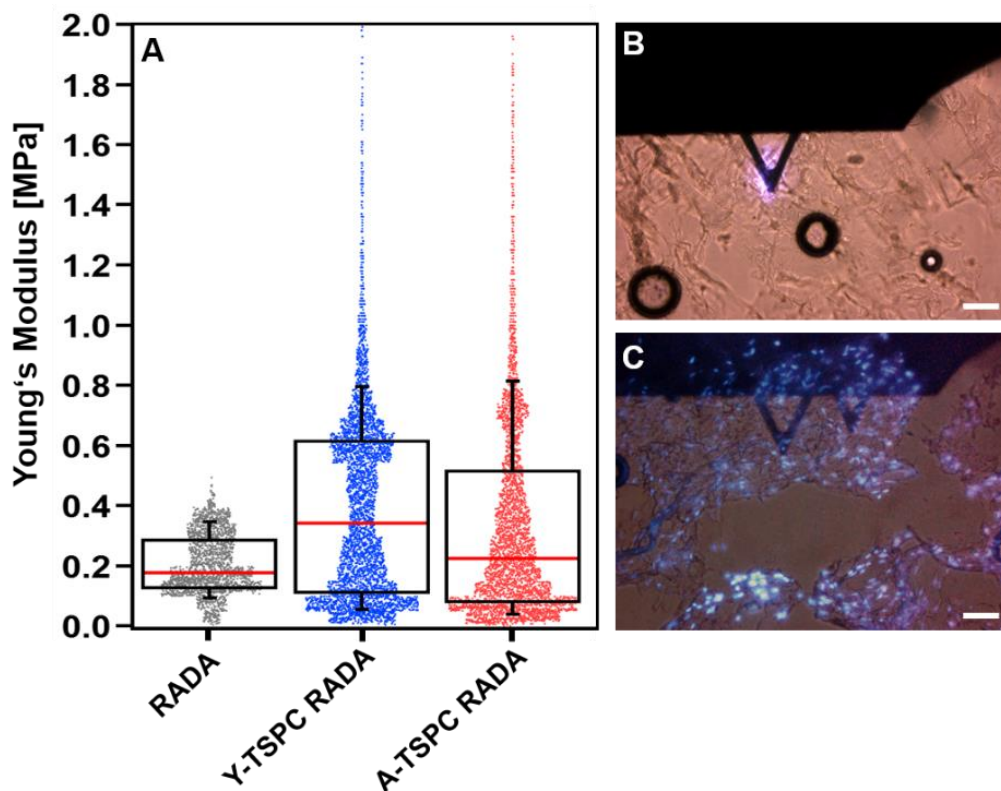


Figure 30: Young's modulus of pure RADA and TSPC cell-laden RADA 3D hydrogels (A). Whisker boxplots display the 10 to 90 percent limits (black lines with end caps), the 25 to 75 percent quantile (black unfilled boxes) and the median (red line) of the Young's modulus. The distributions of the Young's modulus (scatter dot plots) show the accumulation of measured values for pure RADA gel (grey), Y-TSPC-laden RADA gel (blue) and A-TSPC-laden RADA gel (red). For data analysis, the JPK software (Version 6.0.69) was used and the Young's modulus was derived from the indentation part of the curves, using a modified Hertz model. B) Exemplary phase contrast image of a pure RADA gel and C) overlay of phase contrast and Hoechst nuclear staining images of a cell-laden RADA gel. Scale bar: 100 μm . (Published in [114])

The pure RADA hydrogels have an elastic modulus of ~ 0.2 MPa and show a rather homogenous distribution of the Young's modulus (Figure 30 A, grey). After cell cultivation within the gels for seven days, an increased Young's modulus of the gels was observed for both, Y-TSPC and A-TSPCs laden gels. The Y-TSPC laden gel almost doubled the median of the elastic modulus from ~ 0.25 MPa to ~ 0.35 MPa (Figure 30 A, blue). The median of the A-TSPC laden RADA gels, on the other hand, increased only to ~ 0.25 MPa (Figure 30 A, red). Another interesting finding is the profiles of the Young's modulus distributions: After seven days, both cell-laden gels exhibited a bimodal distribution of the Young's modulus values. Both show a high accumulation of Young's modulus values at ~ 0.1 MPa, which is even below the highest accumulation of values for pure RADA gel. Both gels show a similar distribution of the values up to ~ 0.35 MPa. At higher Young's modulus values, Y-TSPC laden RADA gels exhibit a constant frequency distribution of Young's modulus values until ~ 0.55 MPa. At ~ 0.6 MPa a second accumulation of values can be observed. For A-TSPC laden RADA gels, the distribution of Young's modulus values decreases until a second accumulation of values can be observed at ~ 0.7 MPa.

4.4.2 DISCUSSION AND CONCLUSION

The mechanical properties of the ECM have a major influence on cell behavior. In turn, cells can modify ECM properties by active and passive remodeling processes. In this chapter, it was shown that cell-laden 3D RADA gels exhibit a higher Young's modulus when cultivated with Y-TSPCs or with A-TSPCs. The pure 3D RADA hydrogels exhibit a median of the Young's modulus of ~ 0.2 MPa, which is roughly comparable to the Young's modulus of native collagen I fibrils in tendon tissue [154]. An altered Young's modulus of the cell-laden hydrogels can occur through cellular processes. For example, the Young's modulus distribution of the cartilage growth plate increases with increased secretion of collagen [20]. As already shown in 4.1, the Young's modulus decreases with increasing pore size of the matrix, by adding the secretory protein Net-4 [49]. Kohler et al. observed a higher actin turnover and proliferation capacity of Y-TSPCs in 2D, but also a slightly higher cell number of Y-TSPCs after seven days within the 3D gels [27, 114]. Therefore, the increased median of the Young's modulus observed here, may represent the slightly higher proliferation capacity and thus maybe a higher matrix remodeling of Y-TSPCs.

The interplay between cells and the 3D hydrogel creates a complex environment with heterogenic conditions. This complexity becomes apparent because both cell-laden hydrogels exhibit a bimodal Young's modulus distribution due to their composition: hydrogel matrix, cell bodies, nuclei and multiple matrix proteins secreted by TSPCs [27]. Interestingly, the first peak of the Young's modulus values appears at ~0.1 MPa for both cell types. Here, the cells in the 3D hydrogel might remodel the network, leading to presumably larger pores, which in turn manifests itself in a lower first peak of the Young's modulus distribution, than for the pure RADA gel. Contrary, the second peak of the accumulation of Young's modulus values differ between Y- and A-TSPC laden RADA gels. In the previous section, it was shown, that A-TSPCs exhibit a pronounced actin cytoskeleton and a higher Young's modulus when growing on a rigid 2D substrate [26]. Moreover, Kohler et al. showed that A-TSPCs express slightly more fibronectin, together with a higher expression of FN-binding integrins [27]. In another example, it was shown that fibroblasts can degrade fibrin gels proteolytically, but at the same time form stable and stiff fibrin fibers through cellular traction forces and thus locally stiffen the gel [16]. Therefore, A-TSPCs possibly modulate their environment more adhesive by providing integrin-binding motifs resulting in increased spreading and thus in a higher tension within the gel, which could explain a higher second peak of the Young's modulus of A-TSPC laden hydrogels.

Taken together, both cell types changed the Young's modulus of the 3D-RADA-hydrogels. A-TSPCs, more than Y-TSPCs, decreased but also increased the peak of the bimodal distribution of the Young's modulus. According to the previous chapter (4.3), determining the Young's modulus of Y- and A-TSPC-laden 3D-hydrogels is also a suitable biomarker to identify cell aging in 3D constructs.

5 OUTLOOK

In this thesis, structural rearrangements of the actin cytoskeleton have been correlated to changes in the Young's modulus of living cells, and the Young's modulus was attributed mainly to the organization of the actin cytoskeleton. However, the mechanical properties of cells are governed not only by actin fibers but also by a variety of other cell components. Especially by stabilizing structures like the cytoskeleton or the nuclear lamina. The cytoskeleton itself consists of the three main filament-types: actin filaments, microtubules and intermediate filaments. It is crucial that cells have diverse filaments with distinct mechanical properties because cytoskeletal filaments are subjected to constant buckling and bending. Only the interplay of all cytoskeletal filaments enables mechanical diversity. For example, single actin fibers exhibit a diameter of ~ 8 nm and have a persistence length of approx. $10 \mu\text{m}$, whereas large microtubules with a diameter of about 25 nm have a persistence length up to $300 \mu\text{m}$ [61, 155]. Thus, other cytoskeletal components than actin indeed contribute to the biomechanical properties of cells. Recently, the group of Kubitschke and colleagues investigated, to what extent actin filaments and microtubules contribute to the mechanical properties of suspended cells. They found that at small strains ($< 5\%$), cell deformation is largely governed by the actin cytoskeleton, whereas at large strains ($> 5\%$) actin filaments and microtubules cooperate to maintain the cellular shape [156]. Mendez et al. showed, that vimentin also contributes to the mechanical properties, as AFM indentation experiments revealed a reduced elastic modulus of vimentin knockout murine embryo fibroblasts [157]. In this thesis, the presence of other cytoskeletal filaments was not considered. Further experiments should determine the influence of these filament types on the biomechanical properties of the cell. Moreover, the influence of all cytoskeleton filaments on the formation and maturation of FAs and therefore on the cell shape should be investigated in future experiments.

Lamins are intermediate filament proteins and the major structural proteins of the cell nucleus of eukaryotic cells. The nuclear lamina is connected to the actin cytoskeleton by the LINC complex. Discher and colleagues showed a correlation between substrate stiffness and type A lamin (lamin-A) content. They discovered that the level of the nucleoskeletal protein lamin-A scales with the elastic modulus of the tissue. They observed that lamin-A was increased 30-fold from soft to stiff tissue [10]. In brief, matrix stiffness and external stress increase lamin-A levels, which stabilize the nucleus. Therefore, the expression level of lamin-A seems to be mechanosensitive and depends on cytoskeletal tension. In this thesis, it was shown, that both α -actinins A1 and A4 influence the architecture of the actin cytoskeleton and presumably the intracellular tension. This probably results in the destabilization of the nuclear envelope and thus has a major influence on the transduction and translation of mechanical signals. Preliminary results obtained in this thesis indicate, that lamin-A, which is responsible for the stability of the nuclear lamina, forms clusters within the lamina and that the total lamin-A amount is reduced in A1/A4 KO cells (data not shown). A further step in future studies could therefore be the investigation of the lamin-A content in the nuclear envelope and the Young's modulus of the nucleus in cells with an impaired actin cytoskeleton, using the AFM.

A. METHODS AND EXPERIMENTAL DETAILS

A1. CELL CULTURE MATERIAL AND PROTOCOLS

NIH3T3 FIBROBLASTS

The knockout cell lines A1/A4 KO, A1/A4 KO + A1 and A1/A4 KO + A4 were made by simultaneous multi-gene knock-out using CRISPR/Cas9-mediated genome engineering and kindly provided by Prof. Christof Hauck and Alexander Timper (Universität Konstanz). Murine NIH3T3 fibroblast wildtype (WT) cells were cultured in DMEM growth medium (Biochrom) supplemented with 10 % fetal calf serum (FCS) (Biochrom), 1% GlutaMax (Gibco) and 1 % Penicillin / Streptomycin (Biochrom) at 37° C and 10 % CO₂ in a humidified cell culture incubator. A1/A4 KO as well as A1/A4 KO +A1 and A1/A4 KO + A4 cells were additionally cultured with 100 µg/ml Hygromycin (Invitrogen). Cells were subcultured every 2 to 3 days to guarantee a maximal 70-80 % confluence.

TENDON STEM PROGENITOR CELLS

Human tendon stem/progenitor cells (TSPC) used in the present work were isolated from non-ruptured human Achilles tendons (16 donor patients overall) at the Surgical Clinic of Ludwig Maximilians University (LMU) in Munich by Kohler et al. (approved by the Ethical Commission of the LMU Medical Faculty, grant No. 166-08) [27]. Young tendon cells (Y-TSPC) from 4 donors with an average age of 28 ± 5 years were distinguished from aged tendon cells (A-TSPC), extracted from 12 donors with an average age of 63 ± 14 years. Because of tendon degeneration, one 37-year old donor was included in the group of A-TSPC cells [27]. Cells were cultivated in DMEM/Ham's F-12 1:1 mixture (Biochrom) with

stable glutamine, 1xMEM NEAA (Gibco), 10 % FCS (Biochrom), and 400 µg/ml L-ascorbic acid-2-phosphate (Sigma-Aldrich) in a humidified incubator at 37 °C and 5 % CO₂. For all experiments, tendon cells in passages 2–5 were used. For ROCK inhibition, adherent cells were incubated for 72 h with 10 µM ROCK-inhibitor Y-27632 (Sigma-Aldrich) enriched in DMEM/Ham's F-12 1:1 mixture (Biochrom) with stable glutamine, 1xMEM NEAA (Gibco), 10 % FCS (Biochrom), and 400 µg/ml L-ascorbic acid-2-phosphate (Sigma-Aldrich) in a humidified incubator at 37 °C and 5 % CO₂. To provide active ROCK-inhibitor, the Y-27632 supplemented medium was replaced every 24 h, as described in Kohler et al. [27].

A2. MICROSCOPY AND IMMUNOCYTOCHEMISTRY

IMMUNOCYTOCHEMISTRY: STAINING PROCEDURE

For imaging, NIH3T3 fibroblasts were seeded with a confluency of ~60 – 70 % on 10 µg/ml fibronectin (FN) (Applichem) coated 170 µm high precision coverslips (Carl Roth) for 24 h under cell culture conditions. The next day, cells were washed with PBS containing Ca²⁺/Mg²⁺ (Biochrom) and fixed with 3.7 % formaldehyde (Carl Roth) for 15 min at RT followed by washing 3 times with PBS. For permeabilization, cells were incubated with 0.5 % Triton-X 100 (Sigma Aldrich) in PBS for 10 minutes at RT. Cells were washed again with PBS and unspecific binding sites were blocked by incubating the cells in 10 % goat serum (Sigma Aldrich) and 0.1 % Triton-X 100 for 1 hour at RT gently shaken with 150 rpm. Afterward, primary antibodies were added with a final concentration according to manufacturer's instructions in a solution of 1 % BSA, 0.1 % Triton-X 100 in PBS and incubated overnight at 4 °C and 40 rpm. The next day, cells were washed 3 times with 0.2 % Triton-X 100 in PBS for 15 min at RT and 150 rpm. Respective secondary antibodies were added with a final concentration according to manufacturer's instructions in PBS. Furthermore, Phalloidin-Atto594 (Attotec) in a final concentration of 200 ng/ml and DAPI (Roth) with a final concentration of 10 ng/ml, were added. Cells were incubated in this staining solution for 1 hour at RT and 150 rpm in the dark to avoid bleaching. Afterward, the cells were washed with 0.2 % Triton-X in PBS at RT and 150 rpm twice and once with PBS. Cells were mounted in ProLong Diamond Antifade Mountant

(Thermo Fisher) or Abberior antifade solid medium (Abberior) for imaging. Fluorescence images and z-stacks were taken with structured illumination using a Zeiss Observer equipped with the Apotome 2 (Zeiss).

Primary antibodies: Vinculin (Cell Signaling, #13901), myosin IIa (Cell Signaling, #3403), Pan-cadherin (Cell Signaling, #4037), MRTF (Santa Cruz, sc-390324)

Secondary Antibodies: anti-rabbit Alexa Fluor 488 (abcam, ab150081), anti-mouse Alexa Fluor 488 (abcam, ab150117), anti-rabbit Alexa Fluor 594 (Fisher Scientific, A11037), anti-rabbit Alexa Fluor 647 (Cell Signaling, #4414S)

TWO-PHOTON EXCITED FLUORESCENCE

Two-photon excited fluorescence (TPEF) microscopy was performed in cooperation with the Multiphoton Imaging Lab (Munich University of Applied Sciences) with Prof. Thomas Hellerer and Christoph Polzer [158]. Therefore, TSPC cells were seeded on a Col I coated 170 μm thick precision coverslips (Carl Roth) for 24 hours, washed with PBS and fixed with 3.7 % formaldehyde (Carl Roth) for 10 min at RT followed by washing with PBS. Cells were treated with 0.2 % Triton-X 100 (Sigma Aldrich) in PBS for 10 min at RT. For cell staining, Atto594-Phalloidin (Attotec) and DAPI (Appllichem) were applied for 20 min at RT, washed 3 times with PBS, air-dried and mounted with ProLong Diamond Antifade Mountant (ThermoFisher). Then, samples were imaged with a custom-built 2-photon laser scanning microscope using an ultrashort pulsed fiber laser system (Toptica Photonics, FemtoFiber dichro bioMP) emitting at 780 nm and 1030 nm for two-photon excitation. Both lasers were focused onto the specimen by a 100 x apochromat oil immersion objective (NA = 1.49, Nikon). Fluorescence detection was realized using photomultiplier tubes (Hamamatsu Photonics) in non-descanned backward configuration. Height images were acquired by moving the objective in axial direction in steps of 200 nm and averaging over 40 frames at each axial position. Two-color images were merged using ImageJ (Version 1.6.0_24). A home-written Matlab routine (MathWorks) was used to color-code the height of the actin fibers.

SCANNING ELECTRON MICROSCOPY

Scanning electron microscopy (SEM) images were taken in cooperation with Vitali Kulikov and Constanze Eulenkamp (University of applied sciences Munich). Therefore, cells were seeded on FN-coated coverslips and incubated overnight under cell culture conditions. The next day, cells were fixed with 3 % Glutaraldehyd (Roth) for 1 h at 37 °C followed by 4 °C overnight. Then, the cells were washed 3 times for 5 min with SEM-buffer (0.1 M NaH₂PO₄·2H₂O, 0.1 M Na₂HPO₄, 0.1 M Sucrose, pH=7.4). For dehydration, samples were incubated for 15 min each in: 35 % EtOH, 50 % EtOH, 70 % EtOH, 95 % EtOH, 100 % EtOH. Samples were stored in 100 % EtOH overnight at 4 °C. The next day, cells were covered with Hexamethyldisilazan (HMDS) for 3 min. For SEM imaging, samples were sputtered with platinum.

A3. ATOMIC FORCE MICROSCOPY

DETERMINATION OF A SUITED VERTICAL TIP VELOCITY

To determine the effect of varying vertical tip velocities on matrigel and cells, experiments were performed in the quantitative imaging (QI) mode using a Nanowizard 4 AFM, equipped with a 100 μm x 100 μm x 15 μm piezo scanner and temperature-controlled Petri dish holder (JPK Instruments). The AFM was mounted on an inverted optical microscope (Axiovert 200, Carl Zeiss). For matrigel, a scan area of 10 x 10 μm with 20 x 20 force curves were measured. Five different vertical tip velocities were tested: 5, 15, 25, 50, and 75 $\mu\text{m}/\text{s}$ with a constant maximal loading force of 1 nN and a silicon nitride cantilever with a nominal spring constant of 0.03 N/m (Bruker). The Young's modulus was derived from the first 500 nm of the indentation part of the curves using a modified Hertz model, as described in detail elsewhere [20, 130, 159]. For data analysis, the JPK software (Version 6.0.69) was used. For the cells, a scan area of 80 x 80 μm with 60 x 60 force curves was measured. Five different vertical tip velocities were tested: 20, 50, 100, 300, and 500 $\mu\text{m}/\text{s}$ with a constant maximal loading force of 1 nN and a silicon nitride cantilever with a nominal spring constant of 0.01 N/m (Bruker). Young's modulus was determined by fitting the Hertz-Sneddon model to the indentation part of the curves, as described elsewhere [20, 130, 159]. For data analysis, the JPK software (Version 6.0.69) was used.

DETERMINATION OF THE YOUNG'S MODULUS OF MATRIGEL AND THE EFFECT OF NET-4

Indentation measurements on matrigel were performed using the Nanowizard 1 AFM (JPK Instruments), equipped with a 100 μm x 100 μm x 15 μm piezo scanner, mounted on an inverted optical microscope (Axiovert 200, Carl Zeiss). The whole setup was placed on an active isolation table (Micro 60, Halcyonics) inside of a custom-built 1 m³ soundproof box to reduce the influence of ambient noise. All indentation experiments were carried out in PBS at RT, using silicon nitride MLCT cantilevers (Bruker) with a nominal spring constant of 0.03 N/m. The exact force constant was determined for each cantilever individually, using the thermal noise method [160].

The following experiments were carried out using a recombinant full-length netrin-4 (Net-4), kindly provided by Raphael Reuten (Biotech Research & Innovation Centre, Copenhagen). For the mixing experiment, prior to AFM experiments, 100 μl of Matrigel (Corning, Lot. 9091003, Ref. 354234) were gently mixed using a pre-cooled pipette with 0.6 %, 1.2 %, 3 %, 6 %, 10 %, 25 %, 30 % and 50 % Net-4 in PBS (Biochrom) and subsequently pipetted on top of a pre-cooled microscope slide into a silicon ring with an inner diameter of 1 cm. Polymerization of the gel was enabled by an incubation time of 30 min at 37°C. For AFM experiments, a droplet of PBS was pipetted on top of the gel mounted on the AFM sample holder. Maps of 10 x 10 force-distance curves were recorded with a 100 x 100 μm scan area, at a z-piezo velocity of 5 $\mu\text{m/s}$. The indentation force was limited to 2 nN. At least 5 force maps on at least 2 different gels with a total number of 373 - 939 force curves were analyzed. For the titration experiment, 2 ml of Matrigel were pipetted into a precooled Petri dish with 55 mm in diameter, followed by an incubation time of 30 min at 37 °C. For AFM experiments, 9 ml of PBS were pipetted on top of the gel and force curves were recorded on the pure matrigel first. Afterwards, 0.1 %, 0.5 %, 1 %, 2.5 %, 5 %, 10 %, 25 %, 50 % and 100 % Net-4 were added in a titration procedure. Arrays of 10 x 10 force-distance curves were recorded in a 10 μm x 10 μm scan area, at a z-piezo velocity of 5 $\mu\text{m/s}$. In the titration experiments, the indentation force was limited to 3 nN. The Young's modulus was derived from the first 500 nm of the indentation part of the curves using a modified Hertz model, as described in detail elsewhere [20, 130, 159]. For data analysis, the JPK software (Version 6.0.69) was used.

DETERMINATION OF THE YOUNG'S MODULUS OF NIH3T3 FIBROBLASTS

Prior to AFM, plastic 35 mm cell culture dishes (TPP) were coated with 10 $\mu\text{g/ml}$ fibronectin (Applichem) in PBS for 1 h at 37°C. Afterward, NIH3T3 fibroblasts were seeded with a confluency of 50-60 % and allowed to grow for 24 h. All AFM experiments were carried out at 37°C in alpha MEM medium, buffered with 15 mM HEPES (pH7.4). AFM experiments were performed in the QI mode using a Nanowizard 4 AFM equipped with a 100 μm x 100 μm x 15 μm piezo scanner and a temperature-controlled Petri dish holder (JPK Instruments). The AFM was mounted on an inverted optical microscope (Axiovert 200, Carl Zeiss). Using the QI mode, arrays of 256 x 256 force-distance curves were recorded in a 100 μm x 100 μm scan area, at a z-piezo velocity of 300 $\mu\text{m/s}$. The maximum indentation force was set to 1 nN, and the z-range for cantilever retraction was limited to 3 μm to above the contact point of the AFM tip. Silicon nitride MLCT cantilevers (Bruker) with a nominal spring constant of 0.01 N/m were used. The exact force constant was determined for each cantilever individually, using the thermal noise method [160]. AFM data analysis was carried out using the JPK software (Version 6.0.69, JPK Instruments). Force-distance curves were converted to force-indentation curves and the Young's modulus was extracted at each position by fitting the Hertz-Sneddon model to the indentation part of the curves, as described elsewhere [20, 130, 159]. Eight individual WT and A1/A4 KO cells, and five individual A1/A4 KO +A1 and A1/A4 KO + A4 cells, were analyzed.

DETERMINATION OF THE YOUNG'S MODULUS OF TSPCS

Prior to AFM, plastic 35 mm cell culture dishes (TPP) were coated with 20 $\mu\text{g/ml}$ rat-tail collagen I solution (Merck Millipore) in PBS and incubated at 4°C overnight. TSPCs were seeded with a confluency of 50 - 60 % and grown on these dishes for 24 h. All AFM experiments were carried out at 37 °C in alpha MEM medium, buffered with 15 mM HEPES (pH7.4). For all AFM measurements qp-BioAC-20 CB2 AFM cantilevers (Nanosensors) with a nominal force constant of 0.1 N/m, a tip height of 6-8 μm and a tip radius <10 nm with a nearly conical shape were used. Prior to recording the AFM data, the actual cantilever force constant was determined for each cantilever individually, using the thermal noise method [160]. AFM experiments were performed as described in the section before. In case of Y-TSPCs five single cells and for A-TSPCs and A-TSPCs + Y27632, seven individual cells were analyzed.

DETERMINATION OF THE YOUNG'S MODULUS OF TSPC LADEN RADA HYDROGELS

Pure and cell-laden RADA hydrogels were prepared and cultivated for 7 days before they were fixed in 95 % ethanol and 5 % glacial acetic acid at 4°C for 1 h, then submitted to 70 % overnight by D: Docheva's group. Prior to AFM experiments, the hydrogels were rehydrated in 60% ethanol at RT for 1h, followed by 50 % ethanol at RT overnight, and in PBS at RT for 1 h. During the last 5 min, Hoechst H6024 nucleus staining (Sigma-Aldrich) was added for cell identification. After rehydration, the hydrogels were embedded in Tissue-tek (Sakura) and 100 μm thick cryo-sections were produced using a CM1950 cryotome (Leica), as referred in [20]. Indentation measurements were performed using the Nanowizard 1 AFM (JPK Instruments). All indentation experiments were carried out in PBS at RT, using silicon nitride MLCT cantilevers (Bruker) with a nominal spring constant of ~ 0.1 N/m. Maps of 25 x 25 force-distance curves were recorded with a 3 x 3 μm scan area, at a z-piezo velocity of 2 $\mu\text{m/s}$. The indentation force was limited to 5 nN. For each group, three different maps on three different gels were recorded.

A4. CELL MIGRATION, LATRUNCULIN A AND MRTF EXPERIMENTS

CELL MIGRATION ASSAY

For the dot migration assay, cells were concentrated by centrifugation and a drop of 10 μ l cell suspension was placed into an FN-coated Petri dish and incubated for 30 minutes at 37°C and 10% CO₂ to allow the majority of the cells to adhere. Afterward, the droplets were rinsed several times with DMEM to remove unattached cells, resulting in a dense drop-shaped 2D monolayer and incubated overnight. The next day, time-lapse microscopy was carried out using a Zeiss Axio Observer Z1 and the Zeiss Incubator PM S1 with a time interval of five minutes for 27 h. The cell migration assay was carried out in cooperation with Vitali Kulikov at the University of Applied Sciences Munich.

The mean square displacement (MSD) was calculated from the migration assay as referred in [161].

$$MSD(t) = \frac{1}{T - t + 1} \sum_{\tau=0}^{T-1} [\vec{r}(\tau + t) - \vec{r}(\tau)]^2$$

Where $\vec{r}(\tau + t)$ and $\vec{r}(\tau)$ are the position vectors at the given time point τ and $\tau + t$, where here t is the time increment between two subsequent images taken during time-lapse microscopy. T is the total number of time points of a single tracked cell.

DISRUPTION OF THE ACTIN CYTOSKELETON WITH LAT.A

Lifeact-RFP expressing NIH3T3 WT and A1/A4 KO fibroblasts were grown in FN-coated (10 μ g/ml fibronectin) cell culture Petri dishes for 24 h at 37 °C. Petri dishes were transferred to the cell incubation unit mounted on the fluorescent microscope (Zeiss Observer Z1) and time-lapse microscopy was applied. 1 μ M Lat. A was added to the cells at a given time point and time-lapse microscopy was applied with a frame rate of 90 s for 15 min.

MECHANOSENSITIVE TRANSLOCATION OF MRTF IN A SCRATCH ASSAY

For the MRTF translocation assay, cells were seeded into an FN-coated 50 mm ibidi Petri dishes and incubated overnight at 10 % CO₂. The next day, they were tested for confluence and a scratch was applied with a sterile 10 µl pipette tip into a 100% confluent cell layer. Then, the cells were washed several times with PBS and incubated in fresh DMEM for 15 min, 30 min, 1 h and 4 h. Cells were fixed and stained as described before.

B. LIST OF PUBLICATIONS AND MANUSCRIPTS

Publication 1: Stefanie Kiderlen, Christoph Polzer, Joachim O. Rädler, Denitsa Docheva, Hauke Clausen-Schaumann, Stefanie Sudhop: Age related changes in cell stiffness of tendon stem/progenitor cells and a rejuvenating effect of ROCK-inhibition, *Biochemical and Biophysical Research Communications*, (2019), doi: 10.1016/j.bbrc.2019.01.027

Manuscript 1: Stefanie Kiderlen, Timo Baade, Alexander Timper, Vitali Kulikov, Joachim Rädler, Christof Hauck, Hauke Clausen-Schaumann, Stefanie Sudhop: Roles of alpha-actinin-1 and -4 on the actin architecture and mechanical properties of cells. *manuscript in preparation*

Manuscript 2: Raphael Reuten, Sina Zendehroud, Monica Nicolau, Lutz Fleischhauer, Anu Marjaana Laitala, **Stefanie Kiderlen**, Denise Nikodemus, Lena Wullkopf, Sebastian Rune Nielsen, Sarah McNeilly, Carina Prein, Stefanie Sudhop, Kamilla Westarp Zornhagen, Frank Suhr, Eleni Maniati, Oliver M. T. Pearce, Manuel Koch, Lene Broeng Oddershede, Tom van Agtmael, Chris Madsen, Alejandro E. Mayorca-Guiliani, Wilhelm Bloch, Roland Netz, Hauke Clausen-Schaumann, Janine T. Erler: Basement membrane mechanics determine metastasis, *submitted*

Publication 2: Heyong Yin, Franziska Strunz, Jiaju Lu, Christoph Brochhausen, **Stefanie Kiderlen**, Hauke Clausen-Schaumann, Xiumei Wang, Manuela E. Gomes, Volker Alt, Denitsa Docheva, Ph.D.: Three-dimensional self-assembling nanofiber matrix rejuvenates aged/degenerative human tendon stem/progenitor cells, *Biomaterials* (2020), doi: 10.1016/j.biomaterials.2020.119802

Manuscript 3: Reiprich S., Hofbauer E., **Kiderlen S.**, Sudhop S., Clausen-Schaumann H., Böcker W., Aszódi A., Schönitzer V.: Organization and adhesive properties of the hyaluronan pericellular coat in hyaluronan synthases overexpressing mesenchymal stem cells, *submitted*

Publication 3: Pavel Filippov, **Stefanie Kiderlen**, Ursula Koch: Präparation der Oberflächen von hochreinem polykristallinem Aluminium zur mechanischen Analyse mittels Nanoindentierung, *Practical Metallography* (2019), *accepted* (Ref: PM110633)

C. ABBREVIATIONS

2D	Two-dimensional
3D	Three-dimensional
A1	α -actinin-1
A4	α -actinin-4
ABD	Actin binding domain
AFM	Atomic force microscope
AJ	Adherent junctions
BM	Basement membrane
CaM	Calmodulin
CO₂	Carbon dioxide
Col	Collagen
CRISPR	Clustered regularly interspaced short palindromic repeats
DAPI	2-(4-Amidinophenyl)-1H-indole-6-carboxamide
ECM	Extracellular matrix
FA	Focal adhesions
FCS	Fetal calf serum
FD	Force distance
FI	Force indentation
FN	Fibronectin

ABBREVIATIONS

GFP	Green fluorescent protein
HEPES	2-[4-(2-hydroxyethyl)piperazin-1-yl]ethanesulfonic acid
HMDS	1,1,1,3,3,3-Hexamethyldisilazane
KO	Knockout
Lat. A	Latrunculin A
MRTF	Myocardin related transcription factor
MSC	Mesenchymal stem cells
Net-1/-2/-3/-4	Netrin 1-4
PBS	Phosphate buffered saline
QI	Quantitative imaging
RFP	Red fluorescent protein
ROCK	Rho-associated <i>protein</i> kinase
RT	Room temperature
SEM	Scanning electron microscopy
TPEF	Two-photon excited fluorescence
TSPC	Tendon stem progenitor cells
WT	Wildtype

D. REFERENCES

- [1] Chistiakov, D.A.; Orekhov, A.N.; Bobryshev, Y.V. Effects of shear stress on endothelial cells: go with the flow. *Acta physiologica (Oxford, England)*, **2017**, *219*, 382–408.
- [2] Frost, H.M. From Wolff's law to the Utah paradigm: insights about bone physiology and its clinical applications. *The Anatomical record*, **2001**, *262*, 398–419.
- [3] Sharir, A.; Stern, T.; Rot, C.; Shahar, R.; Zelzer, E. Muscle force regulates bone shaping for optimal load-bearing capacity during embryogenesis. *Development (Cambridge, England)*, **2011**, *138*, 3247–3259.
- [4] Croes, S.A.; Bartheld, C.S. von. Measurement of contractile force of skeletal and extraocular muscles: effects of blood supply, muscle size and in situ or in vitro preparation. *Journal of neuroscience methods*, **2007**, *166*, 53–65.
- [5] Charras, G.; Yap, A.S. Tensile Forces and Mechanotransduction at Cell-Cell Junctions. *Current biology : CB*, **2018**, *28*, R445-R457.
- [6] A, K.; A, L. Mechanical Behaviour of Skin: A Review. *J Material Sci Eng*, **2016**, *5*.
- [7] Piérard, G.E.; Piérard, S.; Delvenne, P.; Piérard-Franchimont, C. In vivo evaluation of the skin tensile strength by the suction method: pilot study coping with hysteresis and creep extension. *ISRN dermatology*, **2013**, *2013*, 841217.
- [8] Butcher, D.T.; Alliston, T.; Weaver, V.M. A tense situation: forcing tumour progression. *Nature reviews. Cancer*, **2009**, *9*, 108–122.
- [9] Oftadeh, R.; Perez-Viloria, M.; Villa-Camacho, J.C.; Vaziri, A.; Nazarian, A. Biomechanics and mechanobiology of trabecular bone: a review. *Journal of biomechanical engineering*, **2015**, *137*.
- [10] Swift, J.; Ivanovska, I.L.; Buxboim, A.; Harada, T.; Dingal, P.C.D.P.; Pinter, J.; Pajerowski, J.D.; Spinler, K.R.; Shin, J.-W.; Tewari, M.; Rehfeldt, F.; Speicher, D.W.; Discher, D.E. Nuclear lamin-A scales with tissue stiffness and enhances matrix-directed differentiation. *Science (New York, N.Y.)*, **2013**, *341*, 1240104.
- [11] Handorf, A.M.; Zhou, Y.; Halanski, M.A.; Li, W.-J. Tissue stiffness dictates development, homeostasis, and disease progression. *Organogenesis*, **2015**, *11*, 1–15.
- [12] Tee, S.-Y.; Bausch, A.R.; Janmey, P.A. The mechanical cell. *Current biology : CB*, **2009**, *19*, R745-8.

-
- [13] Kasza, K.E.; Nakamura, F.; Hu, S.; Kollmannsberger, P.; Bonakdar, N.; Fabry, B.; Stossel, T.P.; Wang, N.; Weitz, D.A. Filamin A is essential for active cell stiffening but not passive stiffening under external force. *Biophysical journal*, **2009**, *96*, 4326–4335.
- [14] Bonnans, C.; Chou, J.; Werb, Z. Remodelling the extracellular matrix in development and disease. *Nature reviews. Molecular cell biology*, **2014**, *15*, 786–801.
- [15] Sonbol, H.S. Extracellular Matrix Remodeling in Human Disease. *Journal of microscopy and ultrastructure*, **2018**, *6*, 123–128.
- [16] van Esterik, F.A.S.; Vega, A.V.; Pajanonot, K.A.T.; Cuizon, D.R.; Velayo, M.E.; Dejito, J.; Flores, S.L.; Klein-Nulend, J.; Bacabac, R.G. Fibrin network adaptation to cell-generated forces. *Rheol Acta*, **2018**, *57*, 603–610.
- [17] Smith, L.R.; Cho, S.; Discher, D.E. Stem Cell Differentiation is Regulated by Extracellular Matrix Mechanics. *Physiology (Bethesda, Md.)*, **2018**, *33*, 16–25.
- [18] Kolahi, K.S.; Donjacour, A.; Liu, X.; Lin, W.; Simbulan, R.K.; Bloise, E.; Maltepe, E.; Rinaudo, P. Effect of substrate stiffness on early mouse embryo development. *PLoS one*, **2012**, *7*, e41717.
- [19] Engler, A.J.; Sen, S.; Sweeney, H.L.; Discher, D.E. Matrix elasticity directs stem cell lineage specification. *Cell*, **2006**, *126*, 677–689.
- [20] Prein, C.; Warmbold, N.; Farkas, Z.; Schieker, M.; Aszodi, A.; Clausen-Schaumann, H. Structural and mechanical properties of the proliferative zone of the developing murine growth plate cartilage assessed by atomic force microscopy. *Matrix biology : journal of the International Society for Matrix Biology*, **2016**, *50*, 1–15.
- [21] Huang, H.; Kamm, R.D.; Lee, R.T. Cell mechanics and mechanotransduction: pathways, probes, and physiology. *American Journal of Physiology-Cell Physiology*, **2004**, *287*, C1-C11.
- [22] Dai, J.; Sheetz, M.P. Mechanical properties of neuronal growth cone membranes studied by tether formation with laser optical tweezers. *Biophysical journal*, **1995**, *68*, 988–996.
- [23] Manduca, A.; Oliphant, T.E.; Dresner, M.A.; Mahowald, J.L.; Kruse, S.A.; Amromin, E.; Felmlee, J.P.; Greenleaf, J.F.; Ehman, R.L. Magnetic resonance elastography: Non-invasive mapping of tissue elasticity. *Medical Image Analysis*, **2001**, *5*, 237–254.
- [24] Ophir, J.; Alam, S.K.; Garra, B.; Kallel, F.; Konofagou, E.; Krouskop, T.; Varghese, T. Elastography: Ultrasonic estimation and imaging of the elastic properties of tissues. *Proc Inst Mech Eng H*, **1999**, *213*, 203–233.
- [25] Antonacci, G.; Braakman, S. Biomechanics of subcellular structures by non-invasive Brillouin microscopy. *Sci Rep*, **2016**, *6*, 9.

- [26] Kiderlen, S.; Polzer, C.; Rädler, J.O.; Docheva, D.; Clausen-Schaumann, H.; Sudhop, S. Age related changes in cell stiffness of tendon stem/progenitor cells and a rejuvenating effect of ROCK-inhibition. *Biochemical and biophysical research communications*, **2019**, *509*, 839–844.
- [27] Kohler, J.; Popov, C.; Klotz, B.; Alberton, P.; Prall, W.C.; Haasters, F.; Müller-Deubert, S.; Ebert, R.; Klein-Hitpass, L.; Jakob, F.; Schieker, M.; Docheva, D. Uncovering the cellular and molecular changes in tendon stem/progenitor cells attributed to tendon aging and degeneration. *Aging cell*, **2013**, *12*, 988–999.
- [28] Kuznetsova, T.G.; Starodubtseva, M.N.; Yegorenkov, N.I.; Chizhik, S.A.; Zhdanov, R.I. Atomic force microscopy probing of cell elasticity. *Micron (Oxford, England : 1993)*, **2007**, *38*, 824–833.
- [29] Mitrossilis, D.; Fouchard, J.; Pereira, D.; Postic, F.; Richert, A.; Saint-Jean, M.; Asnacios, A. Real-time single-cell response to stiffness. *Proceedings of the National Academy of Sciences of the United States of America*, **2010**, *107*, 16518–16523.
- [30] Roca-Cusachs, P.; del Rio, A.; Puklin-Faucher, E.; Gauthier, N.C.; Biais, N.; Sheetz, M.P. Integrin-dependent force transmission to the extracellular matrix by α -actinin triggers adhesion maturation. *Proceedings of the National Academy of Sciences of the United States of America*, **2013**, *110*, E1361-70.
- [31] Pascalis, C. de; Etienne-Manneville, S. Single and collective cell migration: the mechanics of adhesions. *Molecular biology of the cell*, **2017**, *28*, 1833–1846.
- [32] Park, J.S.; Chu, J.S.; Tsou, A.D.; Diop, R.; Tang, Z.; Wang, A.; Li, S. The effect of matrix stiffness on the differentiation of mesenchymal stem cells in response to TGF- β . *Biomaterials*, **2011**, *32*, 3921–3930.
- [33] Prager-Khoutorsky, M.; Lichtenstein, A.; Krishnan, R.; Rajendran, K.; Mayo, A.; Kam, Z.; Geiger, B.; Bershadsky, A.D. Fibroblast polarization is a matrix-rigidity-dependent process controlled by focal adhesion mechanosensing. *Nature cell biology*, **2011**, *13*, 1457–1465.
- [34] Pelham, R.J.; Wang, Y.I. Cell locomotion and focal adhesions are regulated by substrate flexibility. *Proceedings of the National Academy of Sciences of the United States of America*, **1997**, *94*, 13661–13665.
- [35] Ariza de Schellenberger, A.; Bergs, J.; Sack, I.; Taupitz, M. The Extracellular Matrix as a Target for Biophysical and Molecular Magnetic Resonance Imaging. In: *Quantification of Biophysical Parameters in Medical Imaging*. Sack, I., Schaeffter, T., Eds.; Springer International Publishing: Cham, **2018**; Vol. 123; pp. 123–150.
- [36] Vracko, R. Basal Lamina Scaffold-Anatomy and Significance for Maintenance of Orderly Tissue Structure: A Review. *The American Journal of Pathology*, **1974**, *77*, 313–346.

- [37] Timpl, R.; Brown, J.C. Supramolecular assembly of basement membranes. *BioEssays : news and reviews in molecular, cellular and developmental biology*, **1996**, *18*, 123–132.
- [38] Yurchenco, P.D.; Ruben, G.C. Basement membrane structure in situ: evidence for lateral associations in the type IV collagen network. *The Journal of cell biology*, **1987**, *105*, 2559–2568.
- [39] Abrams, G.A.; Goodman, S.L.; Nealey, P.F.; Franco, M.; Murphy, C.J. Nanoscale topography of the basement membrane underlying the corneal epithelium of the rhesus macaque. *Cell and tissue research*, **2000**, *299*, 39–46.
- [40] Gaiko-Shcherbak, A.; Fabris, G.; Dreissen, G.; Merkel, R.; Hoffmann, B.; Noetzel, E. The Acinar Cage: Basement Membranes Determine Molecule Exchange and Mechanical Stability of Human Breast Cell Acini. *PloS one*, **2015**, *10*, e0145174.
- [41] Hynes, R.O. The extracellular matrix: not just pretty fibrils. *Science (New York, N.Y.)*, **2009**, *326*, 1216–1219.
- [42] Paulsson, M. Basement membrane proteins: structure, assembly, and cellular interactions. *Critical reviews in biochemistry and molecular biology*, **1992**, *27*, 93–127.
- [43] Khoshnoodi, J.; Pedchenko, V.; Hudson, B.G. Mammalian collagen IV. *Microscopy research and technique*, **2008**, *71*, 357–370.
- [44] LeBleu, V.S.; Macdonald, B.; Kalluri, R. Structure and function of basement membranes. *Experimental biology and medicine (Maywood, N.J.)*, **2007**, *232*, 1121–1129.
- [45] Aumailley, M. The laminin family. *Cell adhesion & migration*, **2013**, *7*, 48–55.
- [46] Hohenester, E.; Yurchenco, P.D. Laminins in basement membrane assembly. *Cell adhesion & migration*, **2013**, *7*, 56–63.
- [47] Ho, M.S.P.; Böse, K.; Mokkapati, S.; Nischt, R.; Smyth, N. Nidogens-Extracellular matrix linker molecules. *Microscopy research and technique*, **2008**, *71*, 387–395.
- [48] Thomsen, M.S.; Routhe, L.J.; Moos, T. The vascular basement membrane in the healthy and pathological brain. *Journal of cerebral blood flow and metabolism : official journal of the International Society of Cerebral Blood Flow and Metabolism*, **2017**, *37*, 3300–3317.
- [49] Reuten, R.; Zendejrou, S.; Nicolau, M.; Fleischhauer, L.; Laitala, A.; Kiderlen, S.; Nikodemus, D.; Wullkopf, L.; Nielsen, S.; McNeilly, S.; Prein, C.; Sudhop, S.; Zornhagen, C.; Suhr, F.; Maniati, E.; Pearce, O.; Koch, M.; Oddershede, L.; van Agtmael, T.; Madsen, C.; Mayorca-Guiliani, A.; Bloch, W.; Netz, R.; Clausen-Schaumann, H.; Erler, J. *Basement membrane mechanics determine metastasis: submitted.*

- [50] Ozdemir, E.; Kakehi, Y.; Okuno, H.; Yoshida, O. Role of matrix metalloproteinase-9 in the basement membrane destruction of superficial urothelial carcinomas. *The Journal of urology*, **1999**, *161*, 1359–1363.
- [51] Reuten, R.; Patel, T.R.; McDougall, M.; Rama, N.; Nikodemus, D.; Gibert, B.; Delcros, J.-G.; Prein, C.; Meier, M.; Metzger, S.; Zhou, Z.; Kaltenberg, J.; McKee, K.K.; Bald, T.; Tüting, T.; Zigrino, P.; Djonov, V.; Bloch, W.; Clausen-Schaumann, H.; Poschl, E.; Yurchenco, P.D.; Ehrbar, M.; Mehlen, P.; Stetefeld, J.; Koch, M. Structural decoding of netrin-4 reveals a regulatory function towards mature basement membranes. *Nat Commun*, **2016**, *7*, 13515.
- [52] Schneiders, F.I.; Maertens, B.; Böse, K.; Li, Y.; Brunken, W.J.; Paulsson, M.; Smyth, N.; Koch, M. Binding of netrin-4 to laminin short arms regulates basement membrane assembly. *The Journal of biological chemistry*, **2007**, *282*, 23750–23758.
- [53] Kelley, L.C.; Lohmer, L.L.; Hagedorn, E.J.; Sherwood, D.R. Traversing the basement membrane in vivo: a diversity of strategies. *The Journal of cell biology*, **2014**, *204*, 291–302.
- [54] Järveläinen, H.; Sainio, A.; Koulu, M.; Wight, T.N.; Penttinen, R. Extracellular matrix molecules: potential targets in pharmacotherapy. *Pharmacological reviews*, **2009**, *61*, 198–223.
- [55] Bateman, J.F.; Boot-Handford, R.P.; Lamandé, S.R. Genetic diseases of connective tissues: cellular and extracellular effects of ECM mutations. *Nature reviews. Genetics*, **2009**, *10*, 173–183.
- [56] Suki, B.; Bates, J.H.T. Extracellular matrix mechanics in lung parenchymal diseases. *Respiratory physiology & neurobiology*, **2008**, *163*, 33–43.
- [57] Cox, T.R.; Erler, J.T. Remodeling and homeostasis of the extracellular matrix: implications for fibrotic diseases and cancer. *Disease models & mechanisms*, **2011**, *4*, 165–178.
- [58] Tarentino, A.L.; Maley, F. A comparison of the substrate specificities of endo-beta-N-acetylglucosaminidases from *Streptomyces griseus* and *Diplococcus Pneumoniae*. *Biochemical and biophysical research communications*, **1975**, *67*, 455–462.
- [59] Paszek, M.J.; Zahir, N.; Johnson, K.R.; Lakins, J.N.; Rozenberg, G.I.; Gefen, A.; Reinhart-King, C.A.; Margulies, S.S.; Dembo, M.; Boettiger, D.; Hammer, D.A.; Weaver, V.M. Tensional homeostasis and the malignant phenotype. *Cancer cell*, **2005**, *8*, 241–254.
- [60] Roy Choudhury, A.; Gupta, S.; Chaturvedi, P.K.; Kumar, N.; Pandey, D. Mechanobiology of Cancer Stem Cells and Their Niche. *Cancer microenvironment : official journal of the International Cancer Microenvironment Society*, **2019**, *12*, 17–27.
- [61] Blanchoin, L.; Boujemaa-Paterski, R.; Sykes, C.; Plastino, J. Actin dynamics, architecture, and mechanics in cell motility. *Physiological reviews*, **2014**, *94*, 235–263.

- [62] Svitkina, T.M. Ultrastructure of the actin cytoskeleton. *Current opinion in cell biology*, **2018**, *54*, 1–8.
- [63] Maninova, M.; Caslavsky, J.; Vomastek, T. The assembly and function of perinuclear actin cap in migrating cells. *Protoplasma*, **2017**, *254*, 1207–1218.
- [64] Tojkander, S.; Gateva, G.; Lappalainen, P. Actin stress fibers--assembly, dynamics and biological roles. *Journal of cell science*, **2012**, *125*, 1855–1864.
- [65] Saez, A.; Buguin, A.; Silberzan, P.; Ladoux, B. Is the mechanical activity of epithelial cells controlled by deformations or forces? *Biophysical journal*, **2005**, *89*, L52-4.
- [66] Ghibaudo, M.; Saez, A.; Trichet, L.; Xayaphoummine, A.; Browaeys, J.; Silberzan, P.; Buguin, A.; Ladoux, B. Traction forces and rigidity sensing regulate cell functions. *Soft Matter*, **2008**, *4*, 1836.
- [67] Yu, C.-h.; Rafiq, N.B.M.; Cao, F.; Zhou, Y.; Krishnasamy, A.; Biswas, K.H.; Ravasio, A.; Chen, Z.; Wang, Y.-H.; Kawauchi, K.; Jones, G.E.; Sheetz, M.P. Integrin-beta3 clusters recruit clathrin-mediated endocytic machinery in the absence of traction force. *Nat Commun*, **2015**, *6*, 8672.
- [68] Haase, K.; Al-Rekabi, Z.; Pelling, A.E. Mechanical cues direct focal adhesion dynamics. *Progress in molecular biology and translational science*, **2014**, *126*, 103–134.
- [69] Maninová, M.; Vomastek, T. Dorsal stress fibers, transverse actin arcs, and perinuclear actin fibers form an interconnected network that induces nuclear movement in polarizing fibroblasts. *The FEBS journal*, **2016**, *283*, 3676–3693.
- [70] Blanchard, A.; Ohanian, V.; Critchley, D. The structure and function of alpha-actinin. *Journal of muscle research and cell motility*, **1989**, *10*, 280–289.
- [71] Otey, C.A.; Carpen, O. Alpha-actinin revisited: a fresh look at an old player. *Cell motility and the cytoskeleton*, **2004**, *58*, 104–111.
- [72] Foley, K.S.; Young, P.W. The non-muscle functions of actinins: an update. *The Biochemical journal*, **2014**, *459*, 1–13.
- [73] Edlund, M.; Lotano, M.A.; Otey, C.A. Dynamics of α -actinin in focal adhesions and stress fibers visualized with α -actinin-green fluorescent protein. *Cell Motil. Cytoskeleton*, **2001**, *48*, 190–200.
- [74] Pavalko, F.M.; Burridge, K. Disruption of the actin cytoskeleton after microinjection of proteolytic fragments of alpha-actinin. *The Journal of cell biology*, **1991**, *114*, 481–491.
- [75] Kovac, B.; Teo, J.L.; Mäkelä, T.P.; Vallenius, T. Assembly of non-contractile dorsal stress fibers requires α -actinin-1 and Rac1 in migrating and spreading cells. *Journal of cell science*, **2013**, *126*, 263–273.
- [76] Goldmann, W.H. Role of vinculin in cellular mechanotransduction. *Cell biology international*, **2016**, *40*, 241–256.

- [77] Knudsen, K. Interaction of alpha-actinin with the cadherin/catenin cell-cell adhesion complex via alpha-catenin. *The Journal of cell biology*, **1995**, *130*, 67–77.
- [78] Sjöblom, B.; Salmazo, A.; Djinović-Carugo, K. Alpha-actinin structure and regulation. *Cellular and molecular life sciences : CMLS*, **2008**, *65*, 2688–2701.
- [79] Le, S.; Hu, X.; Yao, M.; Chen, H.; Yu, M.; Xu, X.; Nakazawa, N.; Margadant, F.M.; Sheetz, M.P.; Yan, J. Mechanotransmission and Mechanosensing of Human alpha-Actinin 1. *Cell reports*, **2017**, *21*, 2714–2723.
- [80] Quick, Q.; Skalli, O. Alpha-actinin 1 and alpha-actinin 4: contrasting roles in the survival, motility, and RhoA signaling of astrocytoma cells. *Experimental cell research*, **2010**, *316*, 1137–1147.
- [81] Murphy, A.C.H.; Young, P.W. The actinin family of actin cross-linking proteins - a genetic perspective. *Cell & bioscience*, **2015**, *5*, 49.
- [82] Zaidel-Bar, R.; Itzkovitz, S.; Ma'ayan, A.; Iyengar, R.; Geiger, B. Functional atlas of the integrin adhesome. *Nature cell biology*, **2007**, *9*, 858–867.
- [83] Timper, A.; Simon, M.; Wang, L.; Buchmuller, B.; Tran, S.; Buerger, S.; Grottrup, M.; Paone, C.; Hauck, C. *Rapid multiplex gene disruption and complementation in mammalian cells reveals a novel function of alpha-actinin-1 binding to the integrin beta subunit, in preparation.*
- [84] Timper, A. *Knockout and complementation of non-muscle α -actinin-1 and -4 reveals new aspects of their role in stress fiber formation, focal adhesion organization and cell migration: Dissertation, submitted, 2019.*
- [85] Nourshargh, S.; Alon, R. Leukocyte migration into inflamed tissues. *Immunity*, **2014**, *41*, 694–707.
- [86] Vishwakarma, M.; Di Russo, J.; Probst, D.; Schwarz, U.S.; Das, T.; Spatz, J.P. Mechanical interactions among followers determine the emergence of leaders in migrating epithelial cell collectives. *Nat Commun*, **2018**, *9*, 3469.
- [87] Hanahan, D.; Weinberg, R.A. Hallmarks of cancer: the next generation. *Cell*, **2011**, *144*, 646–674.
- [88] Eble, J.A.; Niland, S. The extracellular matrix in tumor progression and metastasis. *Clinical & experimental metastasis*, **2019**, *36*, 171–198.
- [89] Tse, J.R.; Engler, A.J. Stiffness gradients mimicking in vivo tissue variation regulate mesenchymal stem cell fate. *PloS one*, **2011**, *6*, e15978.
- [90] Liu, L.; Rando, T.A. Manifestations and mechanisms of stem cell aging. *The Journal of cell biology*, **2011**, *193*, 257–266.
- [91] Rando, T.A. Stem cells, ageing and the quest for immortality. *Nature*, **2006**, *441*, 1080–1086.

- [92] Bianco, C.; Rangel, M.C.; Castro, N.P.; Nagaoka, T.; Rollman, K.; Gonzales, M.; Salomon, D.S. Role of Cripto-1 in stem cell maintenance and malignant progression. *The American Journal of Pathology*, **2010**, *177*, 532–540.
- [93] Pisciotta, A.; Bertoni, L.; Vallarola, A.; Bertani, G.; Mecugni, D.; Carnevale, G. Neural crest derived stem cells from dental pulp and tooth-associated stem cells for peripheral nerve regeneration. *Neural regeneration research*, **2020**, *15*, 373–381.
- [94] Baxter, M.A.; Wynn, R.F.; Jowitt, S.N.; Wraith, J.E.; Fairbairn, L.J.; Bellantuono, I. Study of telomere length reveals rapid aging of human marrow stromal cells following in vitro expansion. *Stem cells (Dayton, Ohio)*, **2004**, *22*, 675–682.
- [95] Sethe, S.; Scutt, A.; Stolzing, A. Aging of mesenchymal stem cells. *Ageing research reviews*, **2006**, *5*, 91–116.
- [96] Yu, J.M.; Wu, X.; Gimble, J.M.; Guan, X.; Freitas, M.A.; Bunnell, B.A. Age-related changes in mesenchymal stem cells derived from rhesus macaque bone marrow. *Aging cell*, **2011**, *10*, 66–79.
- [97] Stolzing, A.; Jones, E.; McGonagle, D.; Scutt, A. Age-related changes in human bone marrow-derived mesenchymal stem cells: consequences for cell therapies. *Mechanisms of ageing and development*, **2008**, *129*, 163–173.
- [98] Kasper, G.; Mao, L.; Geissler, S.; Draycheva, A.; Trippens, J.; Kühnisch, J.; Tschirschmann, M.; Kaspar, K.; Perka, C.; Duda, G.N.; Klose, J. Insights into mesenchymal stem cell aging: involvement of antioxidant defense and actin cytoskeleton. *Stem cells (Dayton, Ohio)*, **2009**, *27*, 1288–1297.
- [99] Wu, F.; Nerlich, M.; Docheva, D. Tendon injuries: Basic science and new repair proposals. *EFORT open reviews*, **2017**, *2*, 332–342.
- [100] Tuite, D.J.; Renström, P.A.; O'Brien, M. The aging tendon. *Scandinavian journal of medicine & science in sports*, **1997**, *7*, 72–77.
- [101] Smith, R.K.W.; Birch, H.L.; Goodman, S.; Heinegård, D.; Goodship, A.E. The influence of ageing and exercise on tendon growth and degeneration—hypotheses for the initiation and prevention of strain-induced tendinopathies. *Comparative Biochemistry and Physiology Part A: Molecular & Integrative Physiology*, **2002**, *133*, 1039–1050.
- [102] Rees, J.D.; Wilson, A.M.; Wolman, R.L. Current concepts in the management of tendon disorders. *Rheumatology (Oxford, England)*, **2006**, *45*, 508–521.
- [103] Lee, K.J.; Clegg, P.D.; Comerford, E.J.; Canty-Laird, E.G. A comparison of the stem cell characteristics of murine tenocytes and tendon-derived stem cells. *BMC musculoskeletal disorders*, **2018**, *19*, 116.

- [104] Bi, Y.; Ehirchiou, D.; Kiltz, T.M.; Inkson, C.A.; Embree, M.C.; Sonoyama, W.; Li, L.; Leet, A.I.; Seo, B.-M.; Zhang, L.; Shi, S.; Young, M.F. Identification of tendon stem/progenitor cells and the role of the extracellular matrix in their niche. *Nature medicine*, **2007**, *13*, 1219–1227.
- [105] Amano, M.; Nakayama, M.; Kaibuchi, K. Rho-kinase/ROCK: A key regulator of the cytoskeleton and cell polarity. *Cytoskeleton (Hoboken, N.J.)*, **2010**, *67*, 545–554.
- [106] Park, J.T.; Kang, H.T.; Park, C.H.; Lee, Y.-S.; Cho, K.A.; Park, S.C. A crucial role of ROCK for alleviation of senescence-associated phenotype. *Experimental gerontology*, **2018**, *106*, 8–15.
- [107] Baker, B.M.; Chen, C.S. Deconstructing the third dimension: how 3D culture microenvironments alter cellular cues. *Journal of cell science*, **2012**, *125*, 3015–3024.
- [108] Yin, Y.; Sanes, J.R.; Miner, J.H. Identification and expression of mouse netrin-4. *Mechanisms of Development*, **2000**, *96*, 115–119.
- [109] Arseni, L.; Lombardi, A.; Orioli, D. From Structure to Phenotype: Impact of Collagen Alterations on Human Health. *International journal of molecular sciences*, **2018**, *19*.
- [110] Starke, J.; Wehrle-Haller, B.; Friedl, P. Plasticity of the actin cytoskeleton in response to extracellular matrix nanostructure and dimensionality. *Biochemical Society transactions*, **2014**, *42*, 1356–1366.
- [111] Caliari, S.R.; Burdick, J.A. A practical guide to hydrogels for cell culture. *Nature methods*, **2016**, *13*, 405–414.
- [112] Cosgrove, B.D.; Gilbert, P.M.; Porpiglia, E.; Mourkioti, F.; Lee, S.P.; Corbel, S.Y.; Llewellyn, M.E.; Delp, S.L.; Blau, H.M. Rejuvenation of the muscle stem cell population restores strength to injured aged muscles. *Nature medicine*, **2014**, *20*, 255–264.
- [113] Li, J.; Hansen, K.C.; Zhang, Y.; Dong, C.; Dinu, C.Z.; Dzieciatkowska, M.; Pei, M. Rejuvenation of chondrogenic potential in a young stem cell microenvironment. *Biomaterials*, **2014**, *35*, 642–653.
- [114] Yin, H.; Strunz, F.; Lu, J.; Brochhausen, C.; Kiderlen, S.; Clausen-Schaumann, H.; Wang, X.; Gomes, M.; Alt, V.; Docheva, D. *Three-dimensional self-assembling nanofiber matrix rejuvenates aged/degenerative human tendon stem/progenitor cells: Biomaterials*, **2020**.
- [115] Gelain, F.; Bottai, D.; Vescovi, A.; Zhang, S. Designer self-assembling peptide nanofiber scaffolds for adult mouse neural stem cell 3-dimensional cultures. *PLoS one*, **2006**, *1*, e119.
- [116] Liu, X.; Wang, X.; Wang, X.; Ren, H.; He, J.; Qiao, L.; Cui, F.-Z. Functionalized self-assembling peptide nanofiber hydrogels mimic stem cell niche to control human adipose stem cell behavior in vitro. *Acta biomaterialia*, **2013**, *9*, 6798–6805.

- [117] Sun, Y.; Li, W.; Wu, X.; Zhang, N.; Zhang, Y.; Ouyang, S.; Song, X.; Fang, X.; Seeram, R.; Xue, W.; He, L.; Wu, W. Functional Self-Assembling Peptide Nanofiber Hydrogels Designed for Nerve Degeneration. *ACS applied materials & interfaces*, **2016**, *8*, 2348–2359.
- [118] Binnig; Quate; Gerber. Atomic force microscope. *Physical review letters*, **1986**, *56*, 930–933.
- [119] Krieg, M.; Fläschner, G.; Alsteens, D.; Gaub, B.M.; Roos, W.H.; Wuite, G.J.L.; Gaub, H.E.; Gerber, C.; Dufrêne, Y.F.; Müller, D.J. Atomic force microscopy-based mechanobiology. *Nat Rev Phys*, **2019**, *1*, 41–57.
- [120] Radmacher, M.; Tillamnn, R.W.; Fritz, M.; Gaub, H.E. From molecules to cells: imaging soft samples with the atomic force microscope. *Science (New York, N.Y.)*, **1992**, *257*, 1900–1905.
- [121] Radmacher, M.; Cleveland, J.P.; Fritz, M.; Hansma, H.G.; Hansma, P.K. Mapping interaction forces with the atomic force microscope. *Biophysical journal*, **1994**, *66*, 2159–2165.
- [122] JPK Instruments AG. QI™ mode - Quantitative Imaging with the NanoWizard® 3 AFM: Technical Note (Accessed November 18, 2019).
- [123] Chopinet, L.; Formosa, C.; Rols, M.P.; Duval, R.E.; Dague, E. Imaging living cells surface and quantifying its properties at high resolution using AFM in QI™ mode. *Micron (Oxford, England : 1993)*, **2013**, *48*, 26–33.
- [124] Hertz, H. Ueber die Berührung fester elastischer Körper. *Journal für die reine und angewandte Mathematik (Crelles Journal)*, **1882**, *1882*, 156–171.
- [125] Sneddon, I.N. The stress distribution due to a force in the interior of a semi-infinite elastic medium. *Math. Proc. Camb. Phil. Soc.*, **1944**, *40*, 229–238.
- [126] Guz, N.; Dokukin, M.; Kalaparthi, V.; Sokolov, I. If cell mechanics can be described by elastic modulus: study of different models and probes used in indentation experiments. *Biophysical journal*, **2014**, *107*, 564–575.
- [127] Mahaffy, R.E.; Park, S.; Gerde, E.; Käs, J.; Shih, C.K. Quantitative Analysis of the Viscoelastic Properties of Thin Regions of Fibroblasts Using Atomic Force Microscopy. *Biophysical journal*, **2004**, *86*, 1777–1793.
- [128] Bilodeau, G.G. Regular Pyramid Punch Problem. *Journal of Applied Mechanics*, **1992**, *59*, 519–523.
- [129] Li, L.; Zhang, W.; Wang, J. A viscoelastic-stochastic model of the effects of cytoskeleton remodelling on cell adhesion. *Royal Society open science*, **2016**, *3*, 160539.
- [130] Sneddon, I.N. The relation between load and penetration in the axisymmetric boussinesq problem for a punch of arbitrary profile. *International Journal of Engineering Science*, **1965**, *3*, 47–57.

- [131] Moreno-Flores, S.; Benitez, R.; Vivanco, M.D.; Toca-Herrera, J.L. Stress relaxation microscopy: imaging local stress in cells. *Journal of biomechanics*, **2010**, *43*, 349–354.
- [132] JPK Instruments AG. Determining the elastic modulus of biological samples using atomic force microscopy: Technical Note (Accessed November 20, 2019).
- [133] Garcia, P.D.; Garcia, R. Determination of the viscoelastic properties of a single cell cultured on a rigid support by force microscopy. *Nanoscale*, **2018**, *10*, 19799–19809.
- [134] Soofi, S.S.; Last, J.A.; Liliensiek, S.J.; Nealey, P.F.; Murphy, C.J. The elastic modulus of Matrigel as determined by atomic force microscopy. *Journal of structural biology*, **2009**, *167*, 216–219.
- [135] Weber, A.; Iturri, J.; Benitez, R.; Toca-Herrera, J.L. Measuring biomaterials mechanics with atomic force microscopy. 1. Influence of the loading rate and applied force (pyramidal tips). *Microscopy research and technique*, **2019**, *82*, 1392–1400.
- [136] Domke, J.; Radmacher, M. Measuring the Elastic Properties of Thin Polymer Films with the Atomic Force Microscope. *Langmuir*, **1998**, *14*, 3320–3325.
- [137] Kleinman, H.K.; Martin, G.R. Matrigel: basement membrane matrix with biological activity. *Seminars in cancer biology*, **2005**, *15*, 378–386.
- [138] Slater, K.; Partridge, j.; Nandivad, H. Tuning the Elastic Moduli of Corning® Matrigel® and Collagen I 3D Matrices by Varying the Protein Concentration: Corning Application Note (Accessed 20.22.2019).
- [139] Lejmi, E.; Leconte, L.; Pédrón-Mazoyer, S.; Ropert, S.; Raoul, W.; Lavalette, S.; Bouras, I.; Feron, J.-G.; Maitre-Boube, M.; Assayag, F.; Feumi, C.; Alemany, M.; Jie, T.X.; Merkulova, T.; Poupon, M.-F.; Ruchoux, M.-M.; Tobelem, G.; Sennlaub, F.; Plouët, J. Netrin-4 inhibits angiogenesis via binding to neogenin and recruitment of Unc5B. *Proceedings of the National Academy of Sciences of the United States of America*, **2008**, *105*, 12491–12496.
- [140] Staquicini, F.I.; Dias-Neto, E.; Li, J.; Snyder, E.Y.; Sidman, R.L.; Pasqualini, R.; Arap, W. Discovery of a functional protein complex of netrin-4, laminin gamma1 chain, and integrin alpha6beta1 in mouse neural stem cells. *Proceedings of the National Academy of Sciences of the United States of America*, **2009**, *106*, 2903–2908.
- [141] Eveno, C.; Broqueres-You, D.; Feron, J.-G.; Rampanou, A.; Tijeras-Raballand, A.; Ropert, S.; Leconte, L.; Levy, B.I.; Pocard, M. Netrin-4 delays colorectal cancer carcinomatosis by inhibiting tumor angiogenesis. *The American Journal of Pathology*, **2011**, *178*, 1861–1869.
- [142] Harn, H.I.-C.; Wang, Y.-K.; Hsu, C.-K.; Ho, Y.-T.; Huang, Y.-W.; Chiu, W.-T.; Lin, H.-H.; Cheng, C.-M.; Tang, M.-J. Mechanical coupling of cytoskeletal elasticity and force generation is crucial for understanding the migrating nature of keloid fibroblasts. *Experimental dermatology*, **2015**, *24*, 579–584.

- [143] Kihara, T.; Haghparast, S.M.A.; Shimizu, Y.; Yuba, S.; Miyake, J. Physical properties of mesenchymal stem cells are coordinated by the perinuclear actin cap. *Biochemical and biophysical research communications*, **2011**, *409*, 1–6.
- [144] Sugitate, T.; Kihara, T.; Liu, X.-Y.; Miyake, J. Mechanical role of the nucleus in a cell in terms of elastic modulus. *Current Applied Physics*, **2009**, *9*, e291-e293.
- [145] Guo, Q.; Xia, Y.; Sandig, M.; Yang, J. Characterization of cell elasticity correlated with cell morphology by atomic force microscope. *Journal of biomechanics*, **2012**, *45*, 304–309.
- [146] Zhou, Z.; Akinbiyi, T.; Xu, L.; Ramcharan, M.; Leong, D.J.; Ros, S.J.; Colvin, A.C.; Schaffler, M.B.; Majeska, R.J.; Flatow, E.L.; Sun, H.B. Tendon-derived stem/progenitor cell aging: defective self-renewal and altered fate. *Aging cell*, **2010**, *9*, 911–915.
- [147] Xu, H.; Liu, F. Downregulation of FOXP1 correlates with tendon stem/progenitor cells aging. *Biochemical and biophysical research communications*, **2018**, *504*, 96–102.
- [148] Asai, S.; Otsuru, S.; Candela, M.E.; Cantley, L.; Uchibe, K.; Hofmann, T.J.; Zhang, K.; Wapner, K.L.; Soslowsky, L.J.; Horwitz, E.M.; Enomoto-Iwamoto, M. Tendon progenitor cells in injured tendons have strong chondrogenic potential: the CD105-negative subpopulation induces chondrogenic degeneration. *Stem cells (Dayton, Ohio)*, **2014**, *32*, 3266–3277.
- [149] Ganguly, P.; El-Jawhari, J.J.; Giannoudis, P.V.; Burska, A.N.; Ponchel, F.; Jones, E.A. Age-related Changes in Bone Marrow Mesenchymal Stromal Cells: A Potential Impact on Osteoporosis and Osteoarthritis Development. *Cell transplantation*, **2017**, *26*, 1520–1529.
- [150] Turinetto, V.; Vitale, E.; Giachino, C. Senescence in Human Mesenchymal Stem Cells: Functional Changes and Implications in Stem Cell-Based Therapy. *International journal of molecular sciences*, **2016**, *17*.
- [151] Baker, N.; Boyette, L.B.; Tuan, R.S. Characterization of bone marrow-derived mesenchymal stem cells in aging. *Bone*, **2015**, *70*, 37–47.
- [152] Bongiorno, T.; Kazlow, J.; Mezencev, R.; Griffiths, S.; Olivares-Navarrete, R.; McDonald, J.F.; Schwartz, Z.; Boyan, B.D.; McDevitt, T.C.; Sulchek, T. Mechanical stiffness as an improved single-cell indicator of osteoblastic human mesenchymal stem cell differentiation. *Journal of biomechanics*, **2014**, *47*, 2197–2204.
- [153] Wu, H.; Zhao, G.; Zu, H.; Wang, J.H.-C.; Wang, Q.-M. Aging-related viscoelasticity variation of tendon stem cells (TSCs) characterized by quartz thickness shear mode (TSM) resonators. *Sensors and actuators (Warrendale, Pa.)*, **2015**, *210*, 369–380.

-
- [154] Dex, S.; Alberton, P.; Willkomm, L.; Söllradl, T.; Bago, S.; Milz, S.; Shakibaei, M.; Ignatius, A.; Bloch, W.; Clausen-Schaumann, H.; Shukunami, C.; Schieker, M.; Docheva, D. Tenomodulin is Required for Tendon Endurance Running and Collagen I Fibril Adaptation to Mechanical Load. *EBioMedicine*, **2017**, *20*, 240–254.
- [155] Wisanpitayakorn, P.; Mickolajczyk, K.J.; Hancock, W.O.; Vidali, L.; Tüzel, E. *Measurement of the Persistence Length of Cytoskeletal Filaments using Curvature Distributions*, **2018**.
- [156] Kubitschke, H.; Schnauss, J.; Nnetu, K.D.; Warmt, E.; Stange, R.; Kaes, J. Actin and microtubule networks contribute differently to cell response for small and large strains. *New J. Phys.*, **2017**, *19*, 93003.
- [157] Mendez, M.G.; Restle, D.; Janmey, P.A. Vimentin enhances cell elastic behavior and protects against compressive stress. *Biophysical journal*, **2014**, *107*, 314–323.
- [158] Periasamy, A.; So, P.T.; König, K., Eds. *Multiphoton Microscopy in the Biomedical Sciences XIX*; SPIE, **February 02, 2019 - February 07, 2019**.
- [159] Docheva, D.; Padula, D.; Popov, C.; Mutschler, W.; Clausen-Schaumann, H.; Schieker, M. Researching into the cellular shape, volume and elasticity of mesenchymal stem cells, osteoblasts and osteosarcoma cells by atomic force microscopy. *Journal of cellular and molecular medicine*, **2008**, *12*, 537–552.
- [160] Butt, H.-J.; Jaschke, M. Calculation of thermal noise in atomic force microscopy. *Nanotechnology*, **1995**, *6*, 1–7.
- [161] Gorelik, R.; Gautreau, A. Quantitative and unbiased analysis of directional persistence in cell migration. *Nature protocols*, **2014**, *9*, 1931–1943.

DANKSAGUNG

An dieser Stelle möchte ich mich herzlich bei allen Personen bedanken, die mich während meiner Promotionszeit begleitet, unterstützt und damit zur Entstehung dieser Arbeit beigetragen haben. Besonderer Dank gilt dabei Prof. Dr. Joachim O. Rädler und Prof. Dr. Hauke Clausen-Schaumann für die Betreuung meiner Doktorarbeit sowie Dr. Stefanie Sudhop, für die Betreuung im Labor. Hauke und Stefanie möchte ich dabei noch einmal ausdrücklich für die Unterstützung und die tolle Zusammenarbeit in den letzten Jahren danken.

Großer Dank gilt natürlich dem gesamte Team aus dem Centrum für Angewandtes Tissue Engineering und Regenerative Medizin (CANTER) und dem Labor für Nanoanalytik und Biophysik an der Hochschule München für angewandte Wissenschaften für die Unterstützung, das tolle Arbeitsklima, die Freundschaften und für alle CANTER-Bierchen. Insbesondere möchte ich mich bei Conny Hasselberg-Christoph für die tolle Zusammenarbeit, die ganze Unterstützung und die immer gute Laune bedanken! Danke an meinen Kollegen Bastian Hartmann für das Korrekturlesen, die vielen Diskussionen, Anregungen und die tolle Zeit. Vielen Dank auch an Tanja Becke für die Unterstützung vor allem während meiner Anfangsphase und die schöne Zeit (Bologne). Vielen Dank an Amelie Erben und Lutz Fleischhauer für das Korrekturlesen. Und natürlich danke an Benedikt Kaufmann und Sascha Schwarz für die tolle Zeit! Großer Dank gilt natürlich auch allen Studenten, die mich während meiner Promotion begleitet und unterstützt haben, insbesondere Vitali Kulikov, Michael Stockert, Verena Dubb und Veronika Blache . Danke für eure tolle Mitarbeit und all das Engagement!

Ich bedanke mich auch bei allen kooperativen Arbeitsgruppen für die Projekte und Ideen, die während dieser Zeit entstanden sind. Insbesondere bei dem Kooperationsverbund BayWISS für die finanzielle Unterstützung und die Plattform einer kooperativen Promotion. Danke an Prof. Dr. Christof Hauck, Alex und Timo an der Universität Konstanz, deren KO-Zellen tolle neue Forschungsprojekte für mich eröffnet haben! Aus dem Multiphoton Imaging Labor an der Hochschule München möchte ich insbesondere Christoph Polzer für die Kooperationen, die spannende Zusammenarbeit, das Korrekturlesen, die Unterstützung die super Zeit danken. In diesem Zuge möchte ich mich auch bei Prof. Dr. Thomas Hellerer, und Thomas Kellerer für die tolle Zusammenarbeit bedanken. Danke auch an Prof. Dr. Denitsa Docheva, durch deren TSPC Zellen tolle Kooperationen entstanden sind.

Großer Dank auch an Dr. Raphael Reuten für die tolle Zusammenarbeit und die schönen Projekte.

Großer Dank gilt natürlich meiner Familie auf die ich mich immer verlassen konnte und für all die Unterstützung! Dabei möchte ich mich besonders bei meiner lieben Mama bedanken, einfach für Alles! Für den notwendigen Ausgleich und die tollen Erlebnisse bedanke ich mich herzlich bei allen vier Röckls!

- Last but not least - besonders großer Dank gilt mio amore Florian Wilke, der durch seine Unterstützung einen großen Beitrag zu dieser Arbeit geleistet hat. Danke für deinen bedingungslosen Rückhalt und die wunderschöne Zeit in den letzten Jahren!

Danke!